European Organization for Nuclear Research (CERN)

Geneva, Switzerland

Hochschule Hannover

University of Applied Sciences and Arts

Hanover, Germany

Multiphysics modelling of the LHC main quadrupole superconducting circuit

Master's thesis

Faculty II - Mechanical Engineering and Bio Process Engineering

Author:
Dimitri Pracht

supervised by
Prof. Dr. Martin Gottschlich (Hochschule Hannover)
Dr. Emmanuele Ravaioli (CERN)

February - June 2019

Eidesstattliche Erklärung

Hiermit bestätige ich, Dimitri Pracht, die vorliegende Arbeit selbständig verfasst und keine anderen als die angegebenen Hilfsmittel benutzt zu haben. Die Stellen der Arbeit, die dem Wortlaut oder dem Sinn nach anderen Werken entnommen sind, wurden unter Angabe der Quellen kenntlich gemacht. Weiterhin bestätige ich hiermit, dass die hier vorgelegte wissenschaftliche Arbeit, weder in Teilen noch insgesamt, bisher keinem anderen Prüfungsausschuss vorgelegt wurde.

Genf (Schweiz), den 24.06.2019

Ort, Datum

Dimitri Pracht

List of Figures

List of Tables

Contents

Chapter 1

Introduction

Superconducting magnets that bend and focus the particle beams are one of the key parts of a particle accelerator. In this thesis the LHC Main Quadrupole (MQ) magnet-circuit is the point of investigation. Simulation of the complex electrical, magnetic, and thermal transients occurring in the magnet is critical for analyzing the magnet behaviour and assessing the impact of failure cases. Within this study this complex system was modelled using the STEAM [1] (Simulation of Transient Effects in Accelerator Magnets) framework, which was developed in the Performance Evaluation (PE) section at CERN. The main goal of this thesis is the development, validation, and characterization of the model of the LHC main quadrupole magnet and its circuit. Both models were independently tested and validated against measurement results. Furthermore, both models were coupled in a cooperative simulation (co-simulation) [2], where the circuit model and the magnet model exchange signals across physical domains to reproduce the behaviour during the quench of one of the magnets in the circuit. The simulated results from the co-simulation were validated as well. After finalizing this project, the new models became a part of the library of LHC superconducting circuit models developed with the STEAM framework. In addition, an improved diode model of the cold by-pass diode [3] used in the LHC circuits has been developed and validated against measurement results. Therefore, this thesis is mainly addressed to those responsible of simulating different transient effects in superconducting magnets and circuits and are interested in coupling magnet and circuit models within a co-simulation.

1.1 Thesis structure

Within this thesis, an electro-magnetic-thermal model of the LHC Main Quadrupole magnet was generated with the framework STEAM-SIGMA [4, 5] and simulated with COMSOL©. In addition, a magnet model was generated and simulated using the program STEAM-LEDET [6, 7]. In parallel, a model of the LHC Main Quadrupole circuit was generated using the PSpice© program. PSpice© was used as well to develop a new model of the protection diode used for the main quadrupole magnets. In the final step, the electro-magnetic-thermal magnet model and the electrical circuit model were coupled using the program for cooperative simulation (COSIM) [2]. The simulation results for the magnet

model, the circuit model and the co-simulation model were validated against measurement results collected during test campaigns. The following key points are corresponding to the chapters of the Master's thesis:

- Introduction about superconductivity, accelerator magnets and the LHC [8]
- Description of the LHC Main Quadrupole magnet and its electrical circuit [9]
- Description of the different software used within this thesis
- Generation of the LHC Main Quadrupole magnet model and validation against measurements
- Generation of the LHC Main Quadrupole circuit model and validation against measurements. Development of a new model of a protection diode operating at cryogenic temperatures including electrical and thermal effects
- Generation of a co-simulation model coupling circuit and the magnet models, and validation against measurements

1.2 Large Hadron Collider

The Large Hadron Collider (LHC) is the largest particle accelerator ever built. The LHC is operated by the *Conseil Européen pour la Recherche Nucléaire* (CERN) and is the result of a collaboration of thousands of researchers from different countries. It is a circular particle accelerator with a circumference of about 27 km and four main physical experiments: ATLAS, ALICE, CMS and LHCb [9]. Figure 1.1 shows the schematic view of the LHC with the main experiments. For simplicity, it can be assumed that the complete circumference is subdivided into eight sectors or arcs [8, 9]. The acceleration almost up to the speed of light occurs only in one point at the LHC (Point 4). Two particle beams are accelerated, one in clockwise, the other in counter clockwise direction. If the optimal energy and beam quality is reached, both beams collide and produce analysis data for searching of new particles, which could be generated during the collision. The LHC was designed for a total proton collision energy of 13 TeV. In total, 9593 magnets are installed within the LHC where 1232 of them are the main dipole magnets and 392 are the main quadrupole magnets (see section 1.5) [9]. During the operation the beams turn 11245 times per second and the number of collisions during operation is about 1 billion per second [10]. The principle schematic of the LHC is shown in figure 1.1.

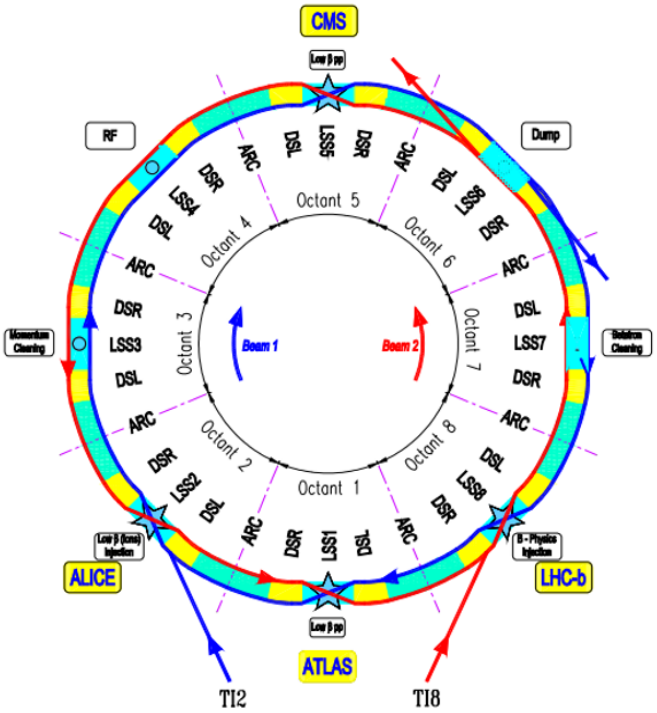

Figure 1.1: Schematic view on the LHC with the main experiments ATLAS, ALICE, CMS, LHCb [9]

In figure 1.1 both beams are injected at two different points with almost the speed of light, coming from the pre-accelerators of the CERN accelerator complex. The LHC can be subdivided into eight octants. Octant 4 contains RF Cavities responsible for the acceleration of the particle beams. Within octant 6 specific equipment can dump both particle beams in case of an emergency during operation [9, 11].

1.3 Superconductivity

The performance of an accelerator relies on the number of collisions between particles per time and contact area as well as on the energy of performed collisions. To increase the collision energy the velocity of the particles has to be increased. Referring to a circular accelerator, this can be fulfilled by increasing the magnetic field strength. The applications of normal conducting magnets are limited by the effect of iron yoke saturation (approximated limitation for iron is 2 T). Moreover, the required energy for powering such a system and the corresponding dimensions of the system would be excessive. For these reasons superconducting magnets are used. Superconducting materials have a vanishing electrical resistance, which results in low required powering energy. Using superconducting materials very high currents can be supplied to generate strong magnetic fields without increasing the system dimensions [7, 12]. For a material to become superconducting, three criteria have to be fulfilled. The superconducting state is determined by the current density J_{sc} [Am^{-2}] of the superconductor, the applied magnetic field B_{ap} [T] and the temperature T [K]. When this determinant parameters are below certain critical values, they form a so-called critical surface in a 3D illustration. Within this critical surface, the supercon-

ducting material remains in a superconducting state. Figure 1.2 shows the critical surface for niobium-titanium (Nb-Ti).

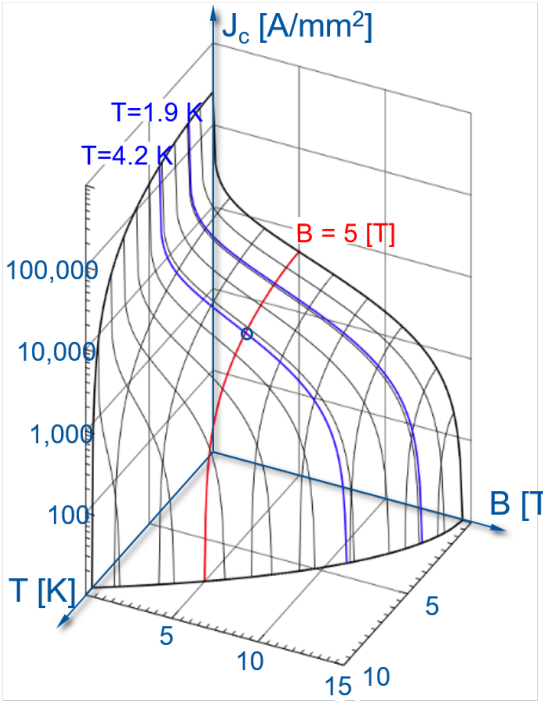

Figure 1.2: Critical surface of the superconducting material Nb-Ti [13]

The critical current density at a specific point of system design can be estimated from the critical surface. For example the critical current density J_c of 3000 Amm^{-2} can be estimated for a field of 5 T and a temperature of 4.2 K using 1.2. For superconductivity, two groups of materials can be distinguished, low-temperature superconductors (LTS) and high-temperature superconductors (HTS). Conventionally, the temperature threshold assigning materials to LTS or HTS is 30 K. The majority of superconducting magnets are composed using low-temperature superconductors like Nb-Ti or Nb_3Sn. In the LHC, presently all superconducting magnets are mainly made of Nb-Ti. For the upgrade of the LHC to higher luminosity, it is planned to install new Nb-Ti and Nb_3Sn magnets in the machine. From the shape of the critical surface of Nb-Ti in figure 1.2 it can be noticed that the maximum magnetic field (about 9 T) can be reached at temperatures between 1.9 K and 4.2 K. However, at 4.2 K and 9 T the critical current density is too small for most practical applications. Therefore, superconducting magnet within the LHC are cooled up to 1.9 K. To provide the required cooling power at this low temperatures, cryogenic baths with superfluid helium are used [12].

1.4 Superconducting cable and superconducting magnets

When the superconductors change their state to normal conducting, their electrical resistivity is about a factor 1000 higher than the one of conductors used at room temperature,

like copper and aluminium [7, 14, 15]. In case if the superconducting material change its state to normal conducting, a parallel path with low resistance has to be provided to reduce the produced ohmic losses ($\approx$ MJ) [12]. This is done by embedding the superconducting material in a resistive matrix made of copper or aluminium. The superconducting material is embedded in the resistive stabilizer matrix in form of thin filaments. This is done to avoid flux jumps and to reduce the errors within the magnetic field [13, 16]. The superconducting filaments are in the order of a few micrometers in diameter. Figure 1.3 shows the cross-sections of two wires, composed of Nb-Ti (a) and Nb_3Sn filaments (b). The absence of superconducting filaments in the centre of the wire (see figure 1.3) is done to allow the filaments the possibility for transposition. If every filament can carry a current of about 25mA to 50 mA, then each wire can carry 250 A to 500 A. As a consequence, it is necessary to use 20 to 40 wires (or strands) for reaching 5000 A to 1000 A. These 20 to 40 wires connected in parallel form a superconducting cable [12]. The LHC magnets are composed using so-called Rutherford cables, which is a cable type used mainly for accelerator magnets. The advantages of Rutherford cables are the high packing factor and the good stacking possibility [17]. Figure 1.4 shows a Rutherford cable from the top and its cross-section.

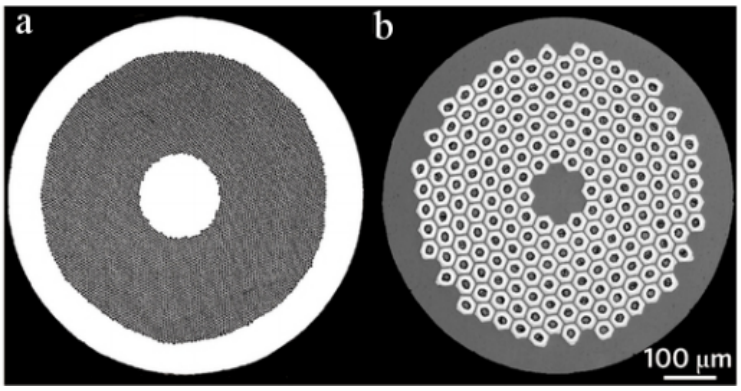

Figure 1.3: Examples of wires with superconducting filaments [18]. (a) Wire made of Nb-Ti filaments embedded in a copper matrix. (b) Wire made of Nb_3Sn filaments.

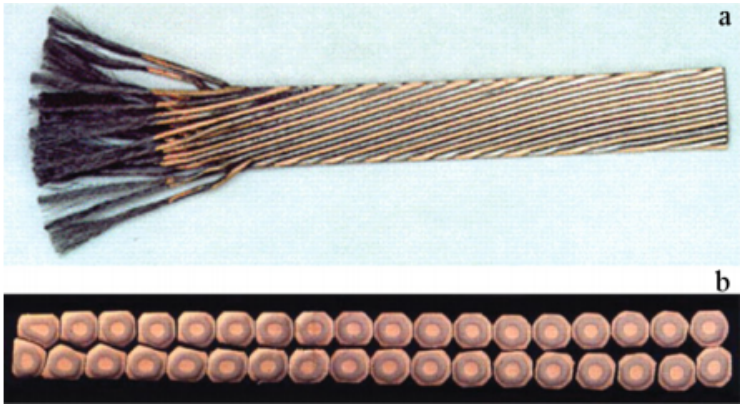

Figure 1.4: Rutherford cable used in the LHC main dipole magnets [16]. (a) View from the top. (b) View at the cross-section

During the operation of superconducting magnets transitory losses are often present and have an effect on the superconducting material. These losses can be subdivided into the main contributions of inter-filament coupling losses (IFCL) [17, 19, 20], inter-strand coupling losses (ISCL) [17, 21, 22], magnetization losses, mechanical losses and eddy-currents losses [17]. From figure 1.4 it can be seen that the strands forming a cable are twisted. This is done to reduce the inter-strand coupling losses (ISCL) development within the cable. These losses can be generated at the contact points between superconducting strands due to coupling currents. Such coupling currents may be present as well between filaments. Therefore, superconducting filaments within each strand are twisted as well to reduce the development of inter-filament coupling losses (IFCL) [17]. The magnetization losses are the result of changing magnetic field distribution within the superconducting filaments. Mechanical losses are the consequence of Lorentz forces during the operation of the magnet that provide movements of the superconducting cable [7, 12].

To achieve the required high-magnetic field, superconducting cables are repeatedly wound and form different coil geometries. The circular cable windings form a so-called solenoid coil. A magnet with this coil geometry provides a homogeneous unidirectional magnetic field and is often used for particle detection in high energy physics like in the Compact Muon Solenoid (CMS) at CERN [23]. Within particle accelerators, several magnet types are present and fulfill different tasks. This requires different coil geometry than the one used for solenoid magnets. As an example the main dipole magnets within the LHC are used for bending the particle beams and providing a circular trajectory of the beams. The main quadrupole magnets within the LHC are needed to focus and de-focus the beams [9, 24]. The three fundamental magnet types (solenoid, dipole and quadrupole) are shown in figure 1.5. As explained above, the collision energy of the particles depends on the strength of the magnetic field of the dipole magnets. Thus, stronger magnetic fields are needed to achieve higher collision energy.

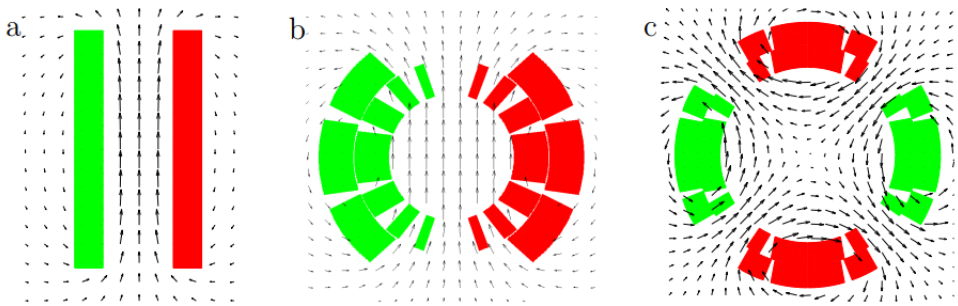

Figure 1.5: Cross-section of differently formed cable coils for magnets. (a) Solenoid magnet. (b) Dipole magnet. (c) Quadrupole magnet. The color of the coil fraction indicates the operation current polarity [7].

1.5 Quench

A quench is the sudden transition of superconducting material to the normal state [17, 25] and can occur when the surrounding conditions of the material like temperature, magnetic

field or current density do not provide the stable operation below the critical surface (see figure 1.2) [12]. The energy density needed to quench a material is in the order of μJmm^{-3}, because the heat capacity of the materials is very small at low temperatures [7]. During operation of a superconducting magnet a quench can occur due to heat leaks, a flux jump, coupling and magnetization losses, heat load coming from radiation or beam loss, the loss of insulation vacuum and even mechanical events like the movement of the conductor due to Lorentz forces [14]. Due to the fact that superconducting magnets are operating at high magnet fields, the stored energy within these magnets can be significant to damage the magnet and interrupt the operation of a particle accelerator for several weeks or months. Therefore, knowing the consequences of a quench in a superconducting magnet is very important for the design of the magnet and for the design of quench protection strategies (see chapter 2.2.2) [26].

When some local part in the magnet becomes normal conducting, the high current passing through the resistive stabilizer matrix at this local part will develop ohmic losses and the local temperature will increase. The initially quenched part (hot-spot) has more time to develop ohmic losses and its temperature is used to limit the maximum allowable temperature during the magnet design process. The allowable temperature limit is usually set by the room temperature. An uncontrolled excessive temperature growth can result in the phase transition of the insulation material or even the conductor material. If in some parts of the coil the temperature increases but in others stays cryogenic, this can cause high temperature gradients followed by high thermal stresses [17]. Moreover, high voltages can develop within the coil as well as between the coil and ground when the high current is passing through the resistive matrix. This can cause short circuits and arcing. Besides high voltages, a pressure increase due to a so-called cryogenic blow-off is possible [27]. Thus, simulation of transients related to a quench is one of the key actions to improve the protection system of superconducting magnets and their circuits.

Chapter 2

LHC main quadrupole magnet and its circuit

As explained in chapter 1, the two particle beams are rotating in different directions. This requires opposite magnetic fields in both channels. The LHC contains 1232 superconducting main dipole magnets (MB) and 392 superconducting main quadrupole magnets (MQ). These magnets contain two apertures, housed in one mechanical structure. Every single aperture is defined by one coil set. Depending on the circuit and the function of each of these coil sets, they can be connected within one electrical circuit or in separate electrical circuits. This will be discussed in detail in the chapters 2.1.2 and 2.2. In this chapter the point of observation is the circuit of the main quadrupole magnets and the main quadrupole magnet itself.

2.1 LHC main quadrupole circuit

As explained in chapter 1, the LHC is divided into eight sectors or arcs. Mechanically, every magnet consists of two apertures (two coil pairs) and is housed in a common mechanical structure, the so-called cold mass. Electrically, the two apertures can be in the same circuit or in two different circuits. In case of the main dipole magnets both apertures are connected within the same circuit. Thus, all main dipole magnets within one arc or sector form one electrical circuit. In case of the main quadrupole magnets, each arc contains two separate electrical circuits.

Each main quadrupole circuit is powered independently and contains physically (depending on the circuit) from 47 up to 51 quadrupole magnets. But electrically, the main quadrupole magnets in each sector form two electrical separate circuits. Thus, the LHC consists of eight main dipole circuits and sixteen main quadrupole circuits. The reason is that within the common mechanical structure of the main quadrupole magnets, both apertures have different functions and are connected in different circuits [9]. These two different circuits are summarized within the abbreviations RQF/RQD. The last letter explains the functionality of the respective circuit. The letter "F" stands for focusing the particle beams in the horizontal plane and the letter "D" stands for de-focusing in the

horizontal plane but focusing in the vertical plane [15] . The use of these circuits is critical for the operation of the LHC-machine.

The LHC main quadrupole circuit can be divided into the following parts [28]:

- power converter (PC)
- energy-extraction (EE)
- main quadrupole magnets (MQ) and their protection system
- earthing circuit (EC)

Figure 2.1 shows a simplified schematic of the LHC main quadrupole circuit.

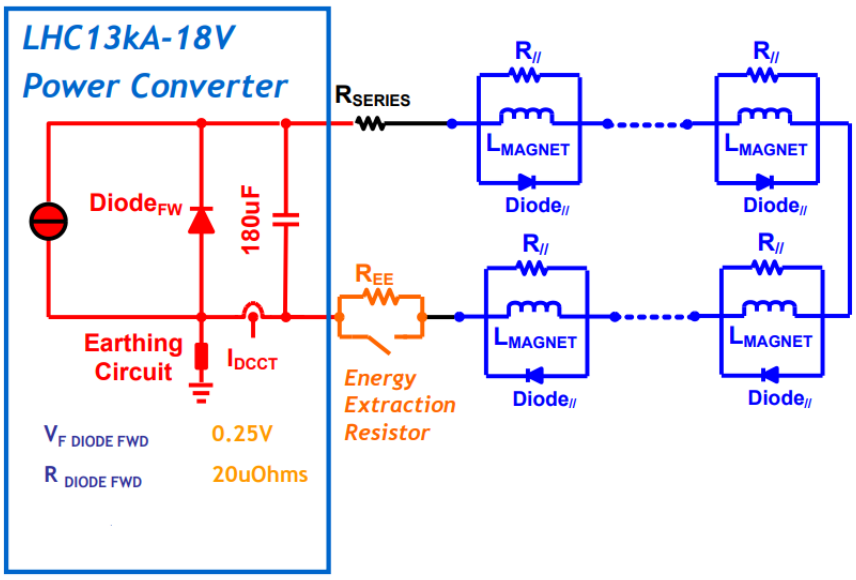

Figure 2.1: simplified schematic of the LHC main quadrupole circuit [28].

The power converter is marked in red, the energy-extraction resistor is marked in orange and the main quadrupole magnets are marked in blue. The resistance of the warm parts of the circuit are marked in black. The warm resistance of the circuit contains the resistance of current leads and other connections to the power converter. The circuit is grounded at the load site of the power converter and all magnets are powered in series. Each magnet has a bypass diode and a resistor in parallel. For reliability reasons the power converter contains several modules and filters, which are needed for providing the nominal current of 11870 A to the magnets [9]. In chapter 2.1.1 the power converter will be described in detail. The energy-extraction system is not a direct part of the protection system for the main quadrupole magnets, but reduces the energy stored in the circuit after detecting a quench [29]. The energy-extraction is explained in detail in chapter 2.1.3. The main quadrupole magnets themselves make up the last part. From electrical point of view the magnets can be considered as a simple inductance and will be described in chapter 2.1.2.

2.1.1 Power Converter

As explained above, every main quadrupole circuit is powered individually. For redundancy reasons the power converter components are divided into different modules. The power converter can be seen as a main module, which contains sub modules. The main module is divided into a 3-levels structure with sub modules, sub-sub modules, and sub-sub-sub modules. The sub-sub-sub modules are the finest elements within this module structure [28]. This structure is shown in figure 2.2 and represents the internal division of modules shown in figure 2.3. The high number of modules increases not only the complexity of the system, but also the reliability. If one of the sub sub modules fails due to an error, all other sub modules are in parallel and the power converter will still work. Figure 2.3 shows a photograph of the LHC main quadrupole power converter, including the five sub modules.

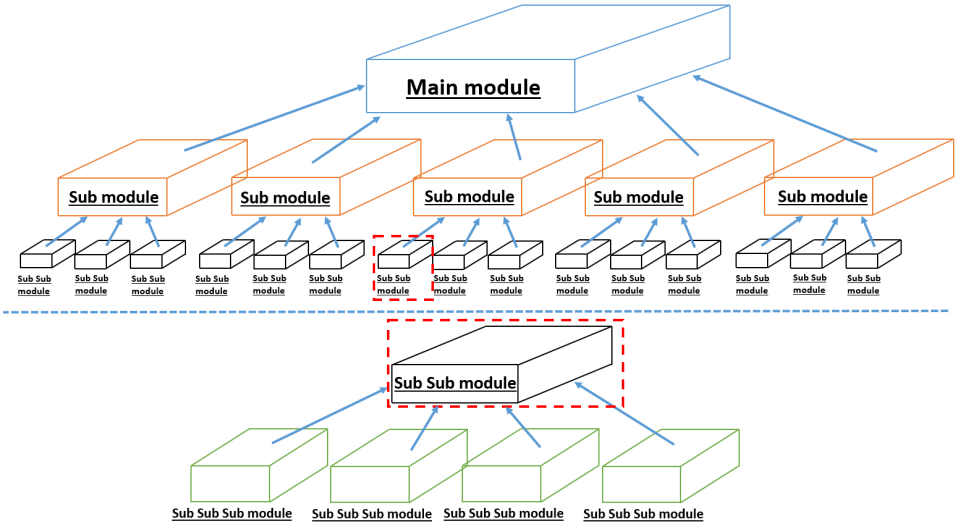

Figure 2.2: LHC main quadrupole power converter - module structure

Figure 2.3: LHC main quadrupole power converter. Division into five sub modules and a power rack connection [28].

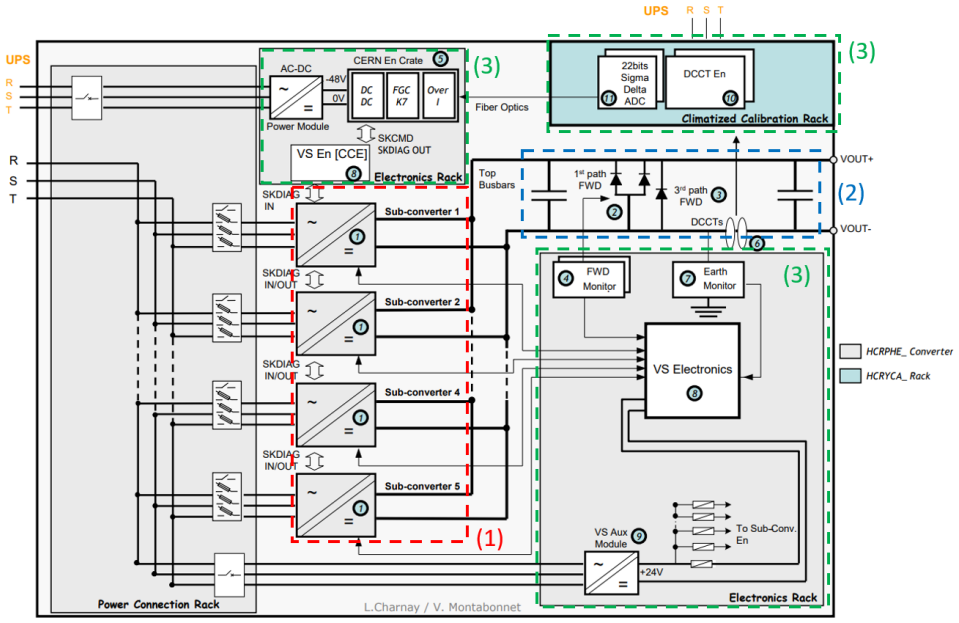

Figure 2.4: LHC main quadrupole power converter. Block diagram [28]

To give a more detailed idea of the sub modules, the following block diagram (figure 2.4) of the LHC main quadrupole power converter circuit has to be considered. Within the block diagram the connection lines from the power connection rack are visible and marked (R, S and T). Every connection line enters each sub-converter module (see first mark in figure 2.4). The sub-converters are connected in parallel and then connected to the first path and to the third path of diodes (see second mark in figure 2.4). The second path of the diodes is connected within the sub-converters. Summarized, three diode paths are connected in parallel. These diodes are designed to carry the current during the discharge of the circuit, after the circuit is disconnected to the power converter.

For controlling the diodes and the sub-converters, monitoring electronics is installed (see third mark in figure 2.4). For modeling the power converter circuit behaviour, this monitoring circuit is not important and will not be taken into account during the circuit modeling in PSpice. Thus, no further details will be provided about this circuit. Another detail level are the sub-converter modules. The sub-converter module is shown in the figure 2.5.

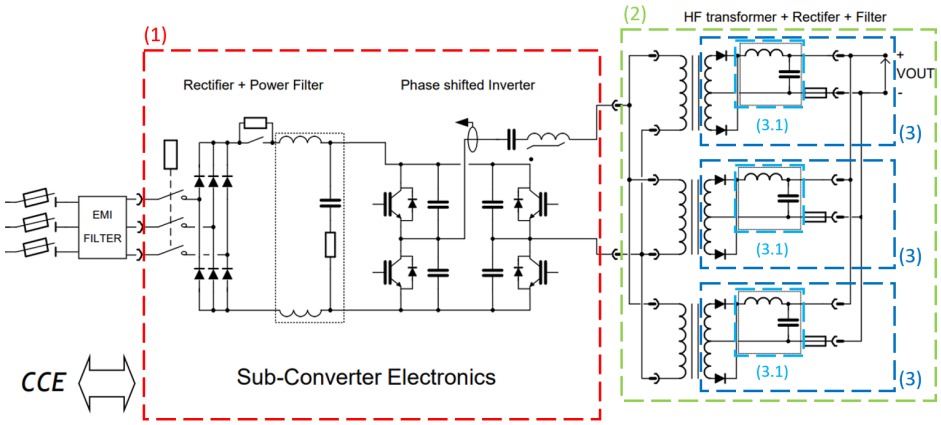

Figure 2.5: LHC main quadrupole power converter. Sub-converter module [28]

Each of the five sub modules consists in principle of two components. The first component is the sub-converter electronics (first mark in figure 2.5), the second is the sub-sub module (second mark in figure 2.5). For modelling the electrical circuit only the sub-sub modules will be taken into account (see (1) and (2) in figure 2.4) as this is the main modelling circuit and not the coupled sub-converter electronics circuit (see (3) in figure 2.4). Within the block diagram in figure 2.4 the output of the sub-converters are connected to the first and the third path of the used diodes. These diodes branches are very important and have to be discussed more detailed.

The first path of the diodes consists of 64 water-cooled Schottky diodes connected in parallel [30]. The diodes within this path are designed to carry nearly 90 % of the whole circuit current during the discharge. The second path of the diodes is installed in the sub-converter modules. Each sub-module contains three sub-sub modules (see second mark in figure 2.5). In sum there are 120 diodes, which are connected in parallel. The diodes used here are water-cooled Schottky diodes as well [30]. They are designed to withstand about 10 % of the current, which remains from the 1st diode path. The 3rd path contains 3 disc diodes, which are connected in parallel. These three diodes are air-cooled and located on the top busbars. These three diodes are designed to carry the current in case of a fault in the other parallel diode paths. To give an impression for which current the diodes were designed, figure 2.6 can be considered. Figure 2.6 shows the diode characteristics for all three diodes branches. From the plot it becomes clear, which current will pass through which diode at a specific voltage. Moreover, it becomes clear that the 3rd diode branch is designed to take the complete current in case if the connection to the two other branches will be destroyed for some reason [31]. Besides the diodes, another important components that are present in the sub-sub modules are the LC-filters. The LC-filters are also visible in figure 2.5 (see (3.1)). The function of these filters is to protect the magnet from high frequency signals due to switch opening or due to a fast power abort (FPA) [28, 32].

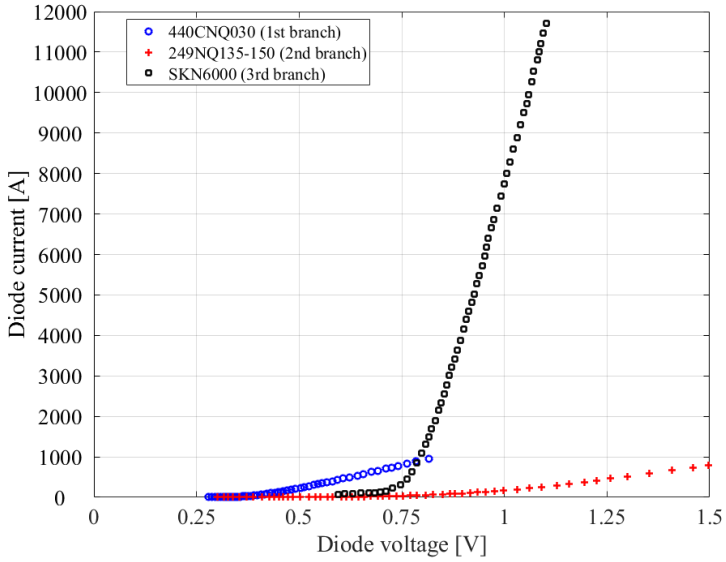

Figure 2.6: Diode characteristics of the three diodes branches used in the power converter. [30, 31, 33]

2.1.2 Earthing Circuit

The next part within the power converter circuit is the earthing circuit. The schematic of the earthing circuit is shown in the figure 2.7. The earthing circuit provides a known and reliable connection of the circuit to ground [28, 34]. In addition, it allows the detection of earth faults and limits the current to ground in case of a failure.

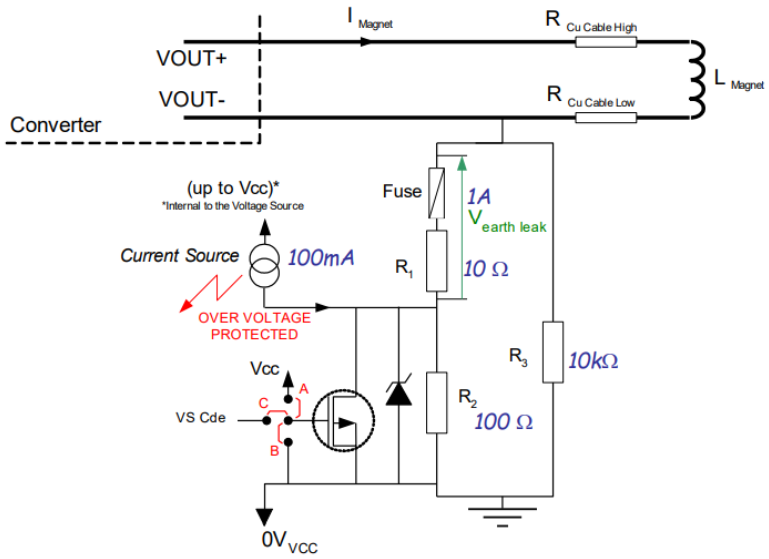

Figure 2.7: LHC main quadrupole power converter. Earthing circuit [28]

The current source in the circuit generates a current of 100 mA, which in absence of faults passes through the resistance R_2. Thus, the voltage across R_2 is nearly 10 V, if there is no earth fault. The entire circuit is lifted to a voltage of +10 V with respect to the main ground. Due to the presence of the parallel resistor R_3, just a very small leakage current through this resistor is present, even without the existence of an earthing fault.

This leakage current is similar to the ratio R_2/R_3 and the source current of 100 mA ($I_{\text{leakage}} \approx 100\ \text{mA} \cdot R_2/R_3 \approx 1\ \text{mA}$). The 1A Fuse and the resistance R_3 is installed to limit the earthing current in case of an earthing fault. If no earth fault occurs, the current through the monitoring resistance R_1 will have the same value as the leakage current through the resistance R_3. The monitoring and detection unit is parallel to the Z-diode and the resistance R_2. The Earth fault threshold is $I_{\text{EC,failure}} = \pm 50$ mA [28].

2.1.3 Energy-Extraction system

Each arc contains two different circuits of the main quadrupole magnets. One combines the focussing, another one the de-focussing magnets. This was already mentioned in chapter 2.1. Added to the main dipole circuit, every arc contains 24 separate electrical circuits. In chapter 2.2 the protection systems of each particular magnet will be explained. But also the circuit itself needs to be protected. Therefore, in total 32 the energy-extraction systems are installed in the LHC. The main dipole circuits are containing two energy-extraction systems, one close to the power converter (similar to figure 2.1 for the MQ circuit) and another one in the mid-point of the circuit. Each of the main quadrupole circuits (focussing and de-focussing) will contain one energy-extraction system, respectively. The energy-extraction system consists of high-current DC breakers, the energy-extraction resistors and control electronics [9, 29]. A simplified schematic of the energy-extraction circuit is shown in figure 2.9.

In the case of a triggered quench or a fast power abort (FPA), the connection to the power converter will be interrupted. After this, the magnet starts discharging and the current of the magnets will go through the protection diode (see figure 2.1 and chapter 2.2.2.2). The diode can withstand such a high current a couple of seconds, but not minutes. For this reason, the energy-extraction resistor is present in the circuit. After a triggered quench or an FPA, the switch of the energy-extraction circuit opens and the complete current will flow through the resistor R_{EE}. Due to his high value (tens of mΩ), the time constant of the discharging time will be significantly reduced. As a result, the diodes wont need to withstand this high current for a long time and will not be destroyed. This fact makes the energy-extraction system a very important part of the LHC main quadrupole circuit. The time constant is the fraction between the total magnet inductance and the circuit resistance, $\tau = L_{\text{m,total}}/(R_{\text{EE}} + R_{\text{circuit}})$. To see the influence of the resistor R_{EE}, the following example could be considered. It can be assumed as a circuit with 47 main quadrupole magnets, which gives an inductance value of $L_{\text{m,total}} = 263$ mH. In addition to that, it can be assumed that except of R_{EE}, only the resistance of the warm parts of the circuit is present with an example value of $R_{\text{circuit}} = 1$ mΩ. The discharging current of an inductance in series with a resistor is given by equation 2.1.

$$I_{\text{circuit}} = I_0 \cdot e^{(-t \cdot (R_{\text{circuit}} + R_{\text{EE}})/L_{\text{m,total}})} \tag{2.1}$$

The discharge starts with the nominal current of $I_0 = 11870$ A at $t = 0$ s. Figure 2.8 shows the current during the discharge over time for two cases. The first case is without

R_{EE}. The second case is with a resistor value of $R_{\mathrm{EE}} = 6.6$ mΩ.

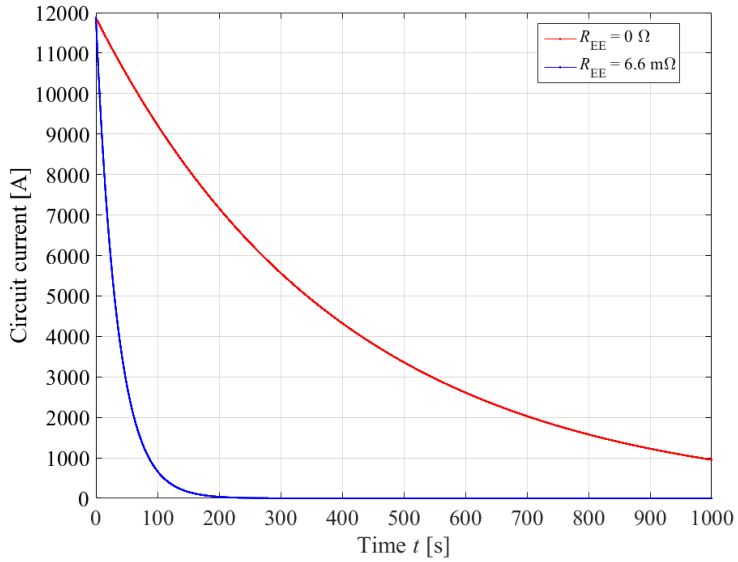

Figure 2.8: Current discharge of a simplified quadrupole circuit - with and without the resistor R_{EE}

In the case with the resistance R_{EE} (blue curve) the current is discharging much faster and achieves $I_{\mathrm{circuit}} \approx 2$ A after $t \approx 300$ s. In contrast, the test case without R_{EE} (red curve) is not completely discharged after $t = 1000$ s. From this very simple example it becomes clear, why the presence of the energy-extraction system is very important for the circuit. The two example curves in figure 2.8 show the influence of the resistor R_{EE} in the circuit. For the real main quadrupole circuit the energy-extraction resistor was designed for an extraction time constant of $\tau \approx 40$ s. Moreover, the energy-extraction resistance and magnet inductance can vary with time. Since the influence of the energy-extraction system is clarified, the structure of the energy-extraction system has to to be discussed in detail [29]. Figure 2.9 shows the schematic of the energy-extraction system.

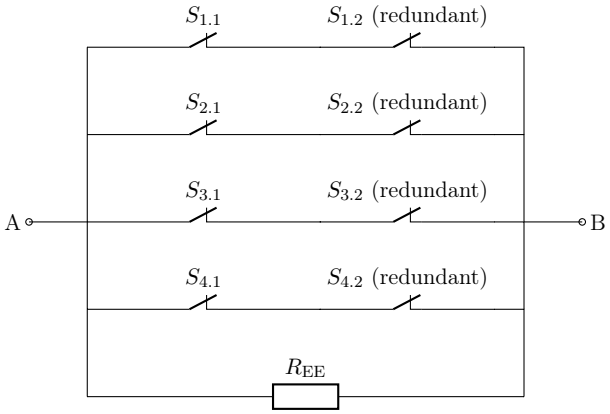

Figure 2.9: Simplified schematic of the energy-extraction circuit

The system consists of four switch branches, which are connected in parallel to the energy-extraction resistor R_{EE}. The current is distributed within these four branches, due

to a water-cooled power bus-way. Each branch contains two series-connected switches for redundancy. For safe operation, at least three branches have to be active. Thus that one of the branches can be opened due to simultaneous failure of both switches in series while assuring the discharge of the magnet circuit, and without permanent damage to the rest of the equipment. The energy-extraction resistor has a body made of stainless steel. Furthermore, the resistor is forced air-cooled and has a included air-to-water heat exchanger. The drawing of an energy-extraction resistor for the main quadrupole magnets is shown in figure 2.10.

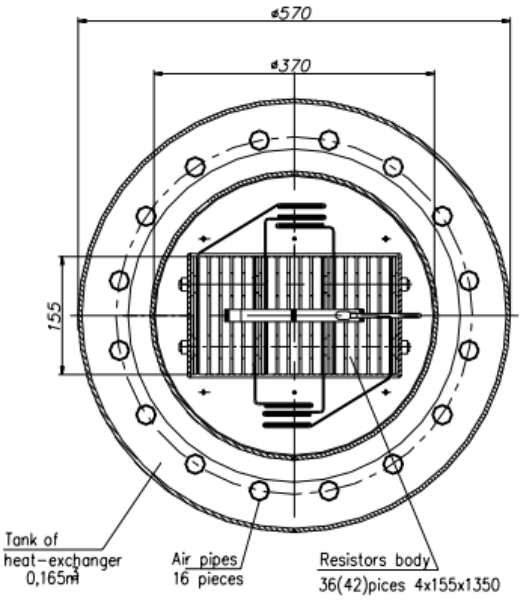

Figure 2.10: Horizontal cross-section of a quadrupole dump resistor [35]

The resistor body is composed of three sub-assemblies. Each of these sub-assemblies consists of 12 series connected resistor plates. All sub-assemblies are connected in parallel. The resistor body is inside of a cylindrical tank, which is filled with 165 litres of water and contains 16 heat-exchanger pipes. Moreover, two fans are mounted on the top of the assembly and guarantee a forced air circulation of air within the closed cooling circuit. The large resistor body and the water-to-air heat exchange are necessary because the entire energy stored in the main quadrupole circuit (22-24 MJ) will be deposited in this resistor during the discharge for a few tens of seconds.

Of course a real switch does not behave ideally and the circuit shown in figure 2.9 has to be adapted to real conditions. Additional effects that have to be taken into account are the following:

- Parasitic elements (resistors and self-inductance of leads, capacitances to ground, etc.)
- Opening phases of the switches in each branch
- Delay between opening of different switches

The first mentioned point is important, because every real component includes a self-inductance and a resistance. Due to the fact that every mechanical component has a delay while opening and closing, the opening phases of the switches need to be taken into account. To understand better the behaviour of the real switches, figure 2.11 can be considered. This figure shows the different opening phases of high current DC-switches, which are used within the energy-extraction system for the main quadrupole magnets. Moreover, the leads have an inductance of 1 μH/m, a resistance of 1 $\mu\Omega$/m, and an additional capacitance across the switch. All this information needs to be considered for modelling the circuit behaviour of the energy-extraction system. The resistance of the switch increases with every finished phase. The opening phases and the related values of the switch resistance are summarized in table 2.1.

Table 2.1: Value table with the time and resistor value for the opening phases of a real switch [29].

No.	**Time**	**Average value**	**Min...Max value**
1	T_{mc} [ms]	2.2	2.0 ... 2.4
2	T_{ac} [ms]	2.0	1.8 ... 2.4
3	T_{br} [ms]	2.6	2.1 ... 3.0
4	T_{arc}[ms]	1.2	1.0 ... 1.8
5	T_{gd} [ms]	0.3	0.2 ... 0.4
No.	**Resistance**	**Average value**	**Min...Max value**
1	R_{mc} [$\mu\Omega$]	80	80
2	R_{ac} [$\mu\Omega$]	260	160 ... 380
3	R_{br2} [mΩ]	33	28.9 ... 36.4
4	R_{arc2} [mΩ]	90	35.7 ... 155.2
5	R_{in} [MΩ]	1.0	1.0

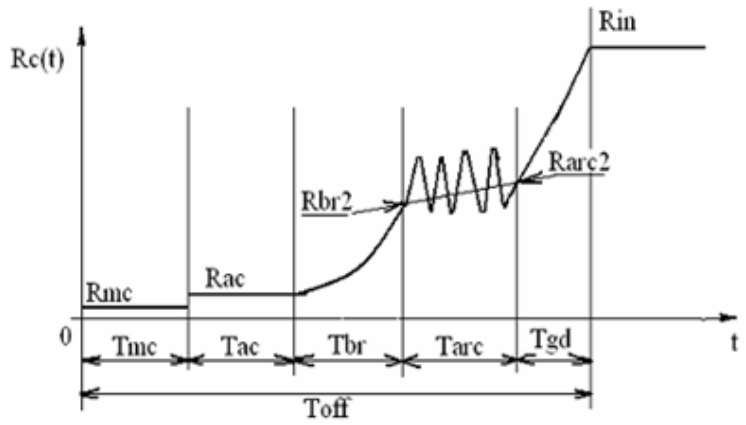

Figure 2.11: Opening phases of a real switch of each energy-extraction circuit branch [29].

2.2 LHC main quadrupole magnet

As explained above, the LHC is divided into eight sectors or arcs. Therefore, the main quadrupole magnets, which will be in focus of this report, are also called arc quadrupoles. Every section contains 23 section cells, which are 106.9 m long and shown in figure 2.12.

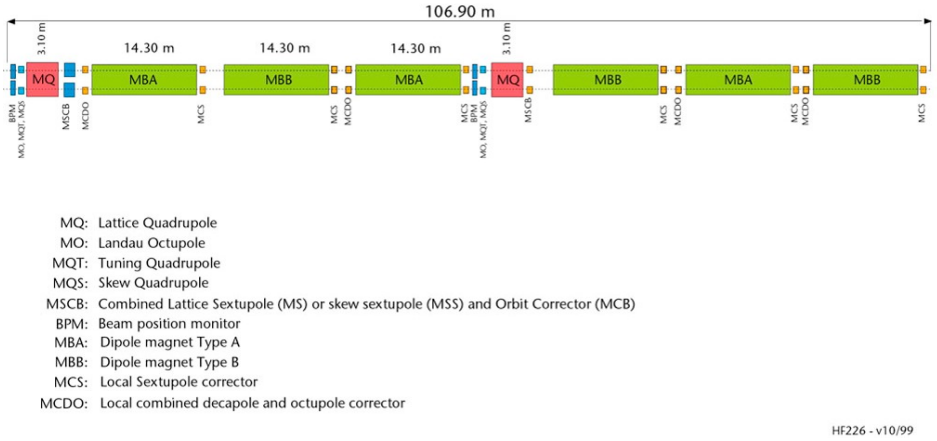

Figure 2.12: One section cell within one LHC arc [9]

Each cell can be divided into two half-cells. Each of these half-cells consists of three dipole magnets, one quadrupole magnet and a number of corrector magnets. The main quadrupole magnets are installed together with sextupole, octupole and dipole corrector magnets in so called short straight sections (SSS). Other quadrupole magnet types are located on both sites of the experiments Atlas, Alice, CMS and LHCb. This string of three quadrupole magnets on each site of the experiments is called the inner triplet. The main dipole magnets achieve a very high magnetic field of 8.33 T and are with a number of 1232 magnets mainly present within the LHC, followed by the main quadrupole magnets with a number of 392 magnets. From figure 2.12 it becomes clear that the length of the main quadrupole magnets is almost 1/5 of the main dipole magnets [9].

2.2.1 Parameters of the Main quadrupole magnets

The advantages of using superconducting materials are explained in chapter 1. Different types of superconducting cables were developed, but this report refers to Rutherford cables as they are used within the main quadrupole magnets. The reason for using cables within superconducting magnets can be boiled down to the high energy needed for accelerating particles. The energy is proportional to the square of the current through the magnet. Thus, high currents are critical for accelerating the particles, which can achieved by cables. Moreover, the field in superconducting magnets is generated by the current and not by the iron yoke, as it is for normal conducting magnets. The superconducting cables needed to be cooled below the critical temperature (see chapter 1). In case of the LHC, the magnets are cooled with superfluid helium at 1.9 K. This allows to achieve a magnetic field above 8 T in the main dipole magnets with the opportunity for reaching an ultimate field of 9 T

[9, 12]. To keep the superconducting magnets at this temperature an extraordinary effort has to be performed.

As explained in the beginning of chapter 2, the main dipole and main quadrupole magnets are double-aperture magnets. In the case of the main dipoles, both aperture are powered in series. In the case of the main quadrupoles, each aperture has either the function of focussing or de-focussing of the beam particles in the horizontal plane. Figure 2.13 shows the cross-section of the LHC main quadrupole magnets within the cold mass.

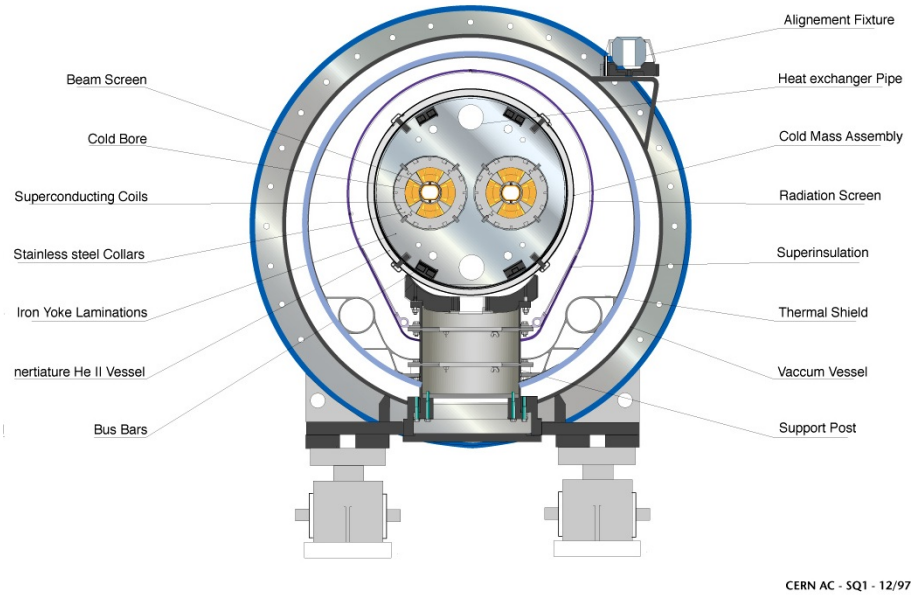

Figure 2.13: LHC main quadrupole cross section [9].

The superconducting coils of both apertures, which are marked in yellow in figure 2.13, are surrounded by stainless steel collars and laminated iron yoke. In the middle of each aperture, the beam screen is located. Around the iron yoke the cold mass assembly is located, which is surrounded by a radiation screen and multilayer-insulation (MLI). The next layer is the so-called thermal shield. The thermal shield with the insulation vacuum are critical to keep the superconducting magnets at 1.9 K. Between the cold mass and the inner wall of the vacuum vessel insulation vacuum ($\sim 10^{-6}$ mbar) is maintained. The insulation vacuum is necessary to avoid heat transfer by gas conduction. The MLI, which is wrapped around the cold mass and the thermal shield is necessary to avoid radiation heat transfer. Between the cold mass assembly and the thermal shield a radiation screen is located. Finally, the thermal shield is surrounded by a vacuum vessel, which separates the magnet from the ambient conditions [9, 36]. Within the following table, the main parameters of the double-aperture main quadrupole magnets are summarized. As explained above, the needed energy requires a current of 11870 A. This results in a stored energy within the magnet of $E_{\mathrm{m}} \approx 0.8$ MJ. This information combined with the information about the importance of the insulation vacuum and the thermal shield, for keeping the magnet at a temperature at 1.9 K, turns out into a conclusion that the monitoring system for all these parameters, as well as the protection system for the magnets is essential for a good

performance of the LHC machine. The cross section of one half aperture is shown in figure 2.14. This figure illustrates more detailed the different parts of the magnet.

Table 2.2: Parameters of the LHC main quadrupole magnet at nominal current [9, 36].

Parameter	**Value**	**Unit**
Superconductor material	Nb-Ti	-
Nominal temperature	1.9	K
Nominal quadrupole gradient value	223	T/m
Peak field in conductor	6.87	T
Nominal current	11870	A
Magnetic length	3.1	m
Self-inductance (both apertures)	11.2	mH
Distance between the centers of the apertures	194	mm
Inner coil diameter	56	mm
Outer coil diameter	118.6	mm
Outer collar diameter	170	mm
Inner yoke diameter	176	mm
Outer yoke diameter	456	mm
Collar material	stainless steel	-
Yoke material	Low carbon steel	-
Stored energy (both apertures)	784	kJ

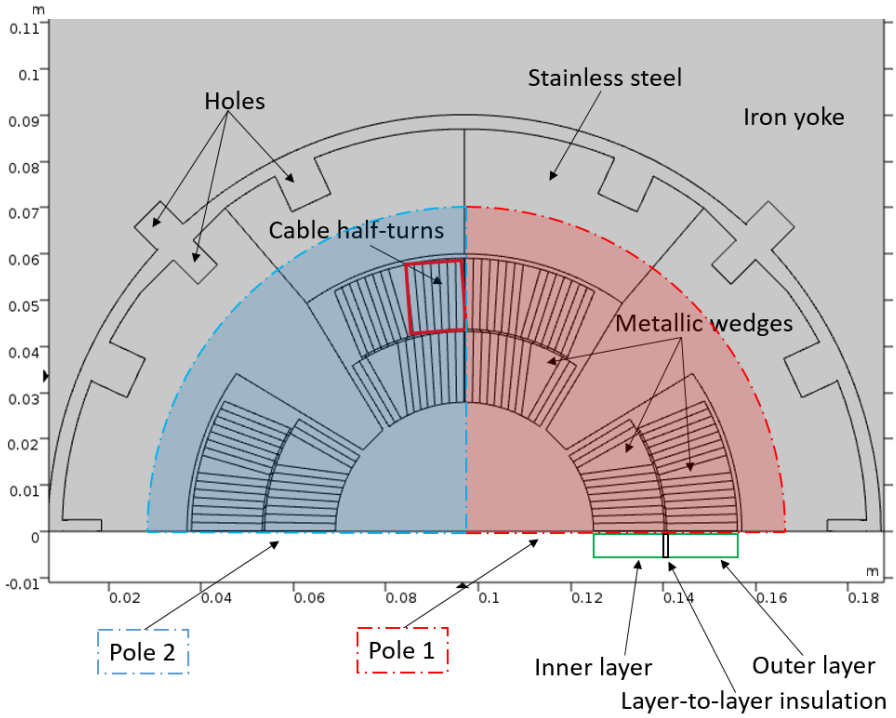

Figure 2.14: Cross-section of one half-aperture of the LHC main quadrupole magnet. Shown in the window of the COMSOL© program

The magnet coil contains an inner and an outer layer made of superconducting Rutherford cable. In figure 2.14 a part of the superconducting cable is marked in red. The inner and outer layer of the superconducting cable are separated by a kapton insulation layer with a thickness of about 500 μm thick. The superconducting cable consists of 36 round strands, which are divided into 2 rows with 18 strands per row. Another part are the metallic wedges that separate two block of turns (see figure 2.14) and provide circular coil geometry in the cross-section. These wedges are in case of the main quadrupole magnets made of copper. Each cable is insulated with kapton strips that are whipped around the cables. Moreover, the copper wedges are insulated with kapton in the same way. The insulation of the copper wedges, as of the cable bares is 0.13 mm thick [9, 27]. Table 2.3 summarizes the most relevant cable parameters for the inner and the outer cable layer. The correlation between the cable geometry and the geometry of the insulation is important to understand the influence of helium and the fraction of helium present in the cable. Figure 2.15 shows the simplified schema for the superconducting Rutherford cable used for the LHC main quadrupole magnets.

Table 2.3: Cable and Strand Parameters of the LHC main quadrupole magnets [9].

Strand	**Value**	**Unit**
Diameter after coating	0.825 $\pm$0.0025	mm
Copper to superconductor ratio	1.95 $\pm$0.05	-
Filament diameter	6	μm
RRR	$\geq$ 150	-
Twist pitch after cabling	100 $\pm$1.5	mm
Cable	**Value**	**Unit**
Number of Strands	36	-
Width	15.10	mm
Thin edge	1.362	mm
Thick edge	1.598	mm
Cable insulation thickness (azimuth)	0.13	mm
Cable insulation thickness (elevation)	0.11	mm

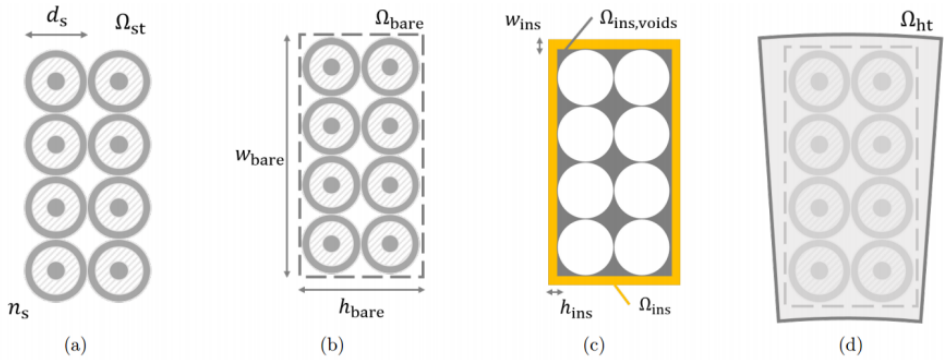

Figure 2.15: Rutherford cable used for the LHC main quadrupole magnets. Simplified schema [37]. (a) Cross-section of the cable strands. (b) Cross-section of the bare cable. (c) Insulated cable (d) Surface area seen by FE-solver (COMSOL©)

In figure 2.15 different stages of the superconducting cable are present. This allows the understanding of the cable geometry and the designations used within the following chapters. Here d_s is the strand diameter after coating (see also table 2.3). As mentioned in chapter 1, the superconducting strand consists in this case out of several thousands of superconducting filament that are embedded in a resistive copper matrix. For the calculation of the strand area Ω_{st} [m^2] equation 2.2 can be considered [37].

$$\Omega_{st} = \frac{1}{\cos\theta_{tp,st}} N_s \pi \left(\frac{d_s}{2}\right)^2 \tag{2.2}$$

Where N_s is the total number of strands within the cable and $\theta_{tp,st}$ is the strand twist-pitch angle. The superconducting filaments and strands are twisted with a certain twist pitch. In case of the filaments this procedure is necessary for reducing the inter-filament coupling loss. To reduce the inter-strand coupling loss, the strands are twisted in the same way. As a result, the twist-pitch angle appears and has to be taken into account. This angle can be considered using equation the 2.3.

$$\theta_{tp,st} = \arctan\left(\frac{w_{bare} - d_s}{0.5 \cdot l_{tp,st}}\right) \tag{2.3}$$

Where w_{bare} [m] is the wide side of the bare cable (see figure 2.15 (b)) and $l_{tp,st}$ [m] the strand twist-pitch (see table 2.3). According to figure 2.15 (b), the area of the bare cable can be calculated using equation 2.4.

$$\Omega_{bare} = w_{bare} \cdot h_{bare} \tag{2.4}$$

The area of the voids within the cable (see figure 2.15 (c)) is the difference between the area of the bare cable and the area of the strands. Therefore, equation 2.5 can be considered.

$$\Omega_{\text{voids}} = \Omega_{\text{bare}} - \Omega_{\text{st}} = w_{\text{bare}} \cdot h_{\text{bare}} - \frac{1}{\cos\theta_{\text{tp,st}}} N_{\text{s}} \pi \left(\frac{d_{\text{s}}}{2}\right)^2 \tag{2.5}$$

The area defined by the voids Ω_{voids}, has to be divided into inner voids $\Omega_{\text{in,voids}}$ and outer voids $\Omega_{\text{out,voids}}$. The inner voids are the sum of the voids without contact to the outer insulation of the cable. Thus, the inner voids are located between the strands. For the calculation of these inner voids equation 2.6 can be considered [37]. In contrast, the outer voids have contact to the cable insulation and can be calculated using equation 2.7.

$$\Omega_{\text{in,voids}} = \frac{(n_{\text{s,l}} - 1)(n_{\text{l}} - 1)}{n_{\text{s,l}} n_{\text{l}}} \Omega_{\text{voids}} \tag{2.6}$$

$$\Omega_{\text{out,voids}} = \frac{n_{\text{s,l}} + n_{\text{l}} - 1}{n_{\text{s,l}} n_{\text{l}}} \Omega_{\text{voids}} \tag{2.7}$$

In the equations 2.6 and 2.7 $n_{\text{st,l}}$ is the number of strands per layer and n_{l} is the number of strand layers in the cable. Finally, the area of the insulated cable is calculated with 2.8.

$$\Omega_{\text{cable,ins}} = (w_{\text{bare}} + 2w_{\text{ins}})(h_{\text{bare}} + 2h_{\text{ins}}) \tag{2.8}$$

Here the narrow and the wide side of the bare cable are given from the cable properties with w_{bare} and h_{bare}, respectively. The insulation is taken into account by using w_{ins} and h_{ins}. Since the geometrical parameters defining the cable are discussed, they will be used in the following chapters.

2.2.2 Quench Protection

The question of quench protection is very important for operating superconducting high energy magnets and will be discussed within this chapter [17, 26]. As discussed in chapter 1 a quench is a status change from superconducting to normal state. If a quench appears in an unprotected high-energy magnet, this can result in the following points [7, 26]:

- High ohmic loss
- High peak temperature
- Loss of control of the stored energy
- High voltages across the magnet
- High mechanical stresses

To avoid the damage of the magnet, a good performing quench protection system has to be designed for the magnet. Several ways exist to protect a superconducting magnet

that will be discussed partially in the following chapters as well. But the following two chapters will take into account the quench protection systems that are directly attached to each magnet. This way of connection is different from the one of the energy-extraction system, which is connected once for a complete circuit (see chapter 2.1.3).

2.2.2.1 Quench Heaters

Quench heaters (QH) are thin stainless-steel strips that are connected with the outer layers of the magnet coil. In case of a quench, the quench heaters are heating up the most part of the coil and are powered by a dedicated voltage supply [38, 39]. After a quench is detected and the quench heaters are powered, a large part of the coil will heat up and will be transferred from superconducting to normal state. Instead of having an excessive temperature in a small volume, a small temperature growth appears in a large volume. The energy is distributed over the magnet volume and the magnet will not be damaged. The following figure shows a quench heater strip used for magnet protection. Even if the magnet the Quench Heaters are attached to is different, the figure gives an idea of how a Quench Heater looks like.

Figure 2.16: Picture of one quench heater strip. Used for high energy superconducting magnets [40].

2.2.2.2 Protection Diode

Another part of the protection system is the protection diode. The protection diode is electrically connected in parallel to the magnet and has to carry the complete current in case of a quench [3]. During the normal operation time the diode is not getting any current. But when the quench is detected, the quench heaters are powered and the magnet starts to become resistive, the voltage across the diode grows until the diode opening voltage is reached. As a result, the diode starts to carry the complete current and to protect the magnet this way. The following two pictures show the protection diode and there location in the magnet cryostat [3]. The first part of picture 2.18 shows the protection diode stack. The stack is located within two heat sinks and is electrically connected with non-insulated busbars. Looking at the location of the diode within the cryostat in picture 2.18 it becomes clear, why the protection diodes are also called "cold diodes". Due to the location within the cold mass at a temperature of 1.9 K, the diode characteristics is different with respect to the one at 300 K. To get an impression, of how much i.e. the forward characteristics

changes with temperature, figure 2.19 can be taken into account. The figure shows the temperature dependence for two diode types (with thin and thick base) of the forward characteristics.

Figure 2.17: Protection diode [41].

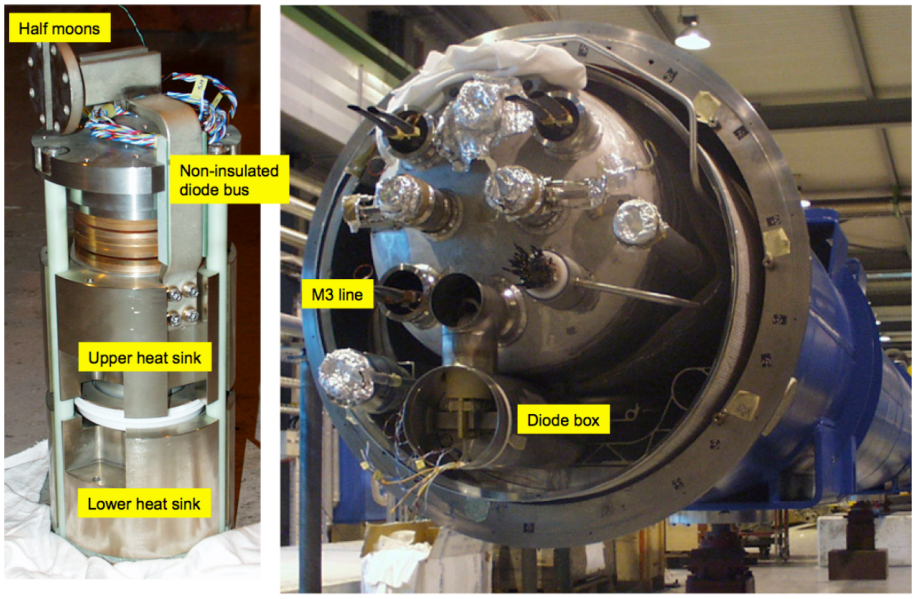

Figure 2.18: Protection diode stack. Assembly and location [41].

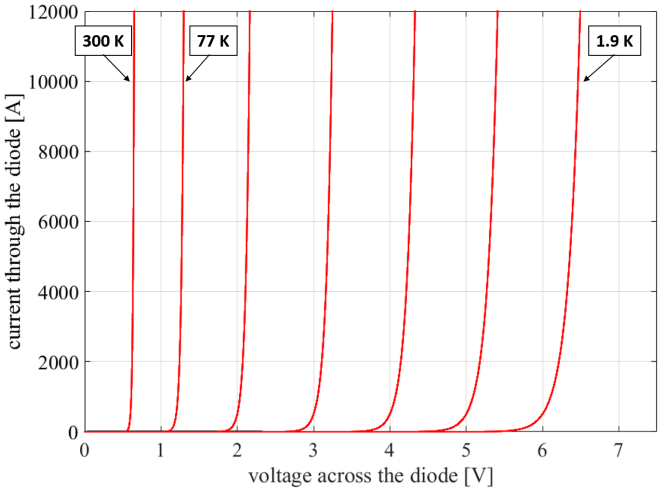

Figure 2.19: Qualitative forward characteristics of the protection diode at different temperatures.

It is visible that the $I_\mathrm{f} = \mathrm{f}(U_\mathrm{f})$ behaviour is shifted to higher forward voltages, if the temperature decreases. Thus, the diode opening voltage is higher with lower tempereture. For protecting the main dipole and main quadrupole magnets, the same diodes are used. This special developed diodes have a cold-turn-on voltage of 6 V at 1.9 K, 1.2 V at 77 K and a voltage of 0.7 V at room temperature.

Chapter 3

Quench protection modelling

In this chapter the physics phenomena relevant to quench protection modelling and programs used for simulating them will be discussed in detail. All programs used within this thesis are part of the STEAM (Simulation of Transient Effects in Accelerator Magnets) framework, which is developed within the section TE-MPE-PE at CERN [1, 37]. This framework uses commercial available and in-house software for simulating transients occurring in superconducting magnets and circuits. The structure of the STEAM framework is shown in the figure 3.1.

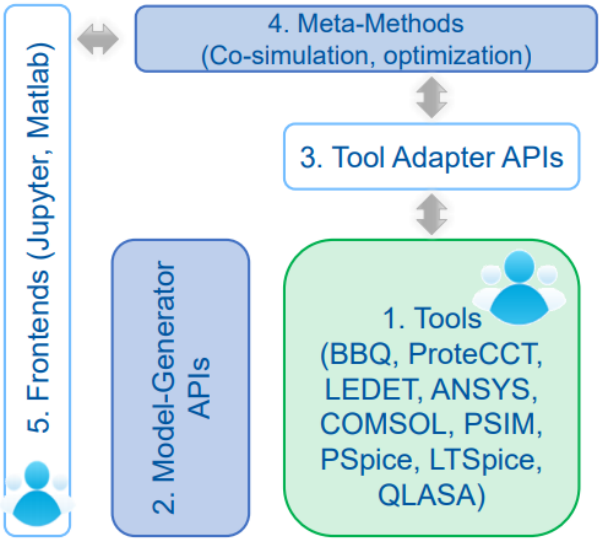

Figure 3.1: Structure of the STEAM framework [42]

The STEAM framework can be subdivided into two parts, called model generation and simulation. For each of these parts the framework contains several programs. For model generation the software STEAM-SIGMA can be used [4, 37]. It provides automated model generation of superconducting magnet models for the COMSOL© (.mph-file). Circuit models can be generated using the software SING. SING helps the user automatically generating SPICE circuit models. After the field (in terms of co-simulation, magnet models are also called field models) and the circuit model are generated, they can be individually simulated. The simulation of the field magnet model can occur within STEAM-LEDET [6,

7] or COMSOL©. STEAM-LEDET is an application, which can be used for the generation and simulation of magnet models. COMSOL© is a finite-element-program for simulating multiphysical behaviour of the superconducting magnets.

The models generated with STEAM-SIGMA will be used by the finite element program COMSOL© for simulating multiphysical behaviour of the magnet. In parallel the circuit model can be generated in an automated way using the tool SING. This tool provides the generation of circuit (.cir) files, which are used within the circuit simulation tool called PSpice©. After the magnet and the circuit models are generated and separately tested, they can be co-simulated by using the software COSIM [2].

3.1 Physics involved in quench protection modeling

For better understanding of the model behaviour during the simulation and the explicit model assumptions, this subsection will focus on the model assumptions and limitations. As explained in chapter 2.2.1, the superconducting cable of the LHC main quadrupole magnets consists of 36 strands, divided into two rows with 18 strands per row. Each strand consists of about 6500 filaments embedded in a stabilizing copper matrix. Due to the manufacturing process of the cables, the volume between the strands within the cable could be filled with insulation material or the voids could still be present. These are the physical effects most relevant for quench protection modelling:

- Inter-filament and inter-strand coupling losses
- Modelling Quench Heaters
- Heat transfer within the magnet model
- Heat capacity of Helium
- One-dimensional quench propagation.

Within the following sections these physical effects will be described more in detail.

3.1.1 Inter-filament and inter-strand coupling losses

These coupling losses within the cable can be divided into inter-filament coupling losses (IFCL) [17, 19, 20] and inter-strand coupling losses (ISCL) [19, 21, 22]. These coupling losses are a result of the magnetic field variation in the strands and in the cables. A variation of the applied magnetic field dB_a/dt [Ts^{-1}] induces a magnetic field B_{if} [T] in a superconducting strand. This magnetic field B_{if} opposes dB_a/dt and the resulting (total) field can be calculated as the sum of these two magnetic fields $B_t = B_a + B_{if}$ [7, 19, 20].

The coupling current flows through the stabilizer copper matrix and develops ohmic losses within this matrix. This results in coupling losses, not only between filaments, but also between strands. As a result, these parts within a superconducting cable can heat up and if the local heat generation is strong enough, it can result in a quench within the cable. Such a quench in a superconducting cable, which is caused by IFCL and ISCL is

called a quench back. Under the assumption of a constant field change dB_a/dt, the power per conductor volume [Wm^{-3}] generated within each wire can be calculated using equation 3.1 [17].

$$P'''_{if} = \left(\frac{l_f}{2\pi}\right)^2 \frac{1}{\rho_{eff}} \left(\frac{dB_t}{dt}\right)^2 = \frac{2}{\mu_0}\tau_{if}\left(\frac{dB_t}{dt}\right)^2 \tag{3.1}$$

Within equation 3.1 the parameter τ_{if} [s] is a characteristic time constant and describes the development of the inter-filament coupling currents. This time constant is described with equation 3.2 [17].

$$\tau_{if} = \frac{\mu_0}{2}\left(\frac{l_f}{2\pi}\right)^2 \frac{1}{\rho_{eff}} \tag{3.2}$$

Within the equations 3.1 and 3.2 l_f [m] is the filament twist-pitch (see chapter 2), ρ_{eff} [Ωm] is the effective transverse resistivity, according to the resistive matrix in which the strands are embedded and $\mu_0 = 4\pi 10^{-7}$ [H/m] is the magnetic permeability of vacuum. The effective transverse resistivity ρ_{eff} is dependent on the residual resistivity ration (RRR), the magneto-resistivity, and the barrier between superconducting filaments and the matrix.

Inter-strand coupling currents are developing when a cable contains several superconducting strands. When a magnetic field change occurs perpendicular to the cable broad face, ISCC are induced and passing through the contact resistance between two crossing strands. Using equation 3.5 the inter-strand coupling losses per volume can be calculated [19].

$$P'''_{is} = \frac{2}{\mu_0}\tau_{is}\left(\frac{dB_{t,\perp}}{dt}\right)^2 \tag{3.3}$$

Equation 3.5 is very similar to 3.1, but now the perpendicular component of the magnetic field is taken into account and the time constant is different. Within equation 3.5 the parameter τ_{is} [s] is a characteristic time constant and describes the development of the inter-strand coupling currents. This time constant is described with equation 3.6 [19].

$$\tau_{is} = \frac{\mu_0}{\pi}\left[\ln\left(\frac{w}{h}\right) + \frac{3}{2}\right]\frac{h}{w}\beta_{is} \tag{3.4}$$

Here h [m] and w [m] are the narrow and wide side of the cable, respectively. Additionally, β_{is} [$m\Omega^{-1}$]is a characteristic parameter.

3.1.2 Modelling quench heaters

The importance of quench heaters in terms of quench protection is discussed within 2.2.2.1. Thus, modelling quench heaters is a very important part of simulating correct magnet behaviour during a quench. During a quench, the quench heaters were triggered to protect the magnet by heating up a large part of the coil so that the energy can distribute over a

larger volume. The quench heaters are heating up the outer layer of the magnet coil. For implementing quench heaters in COMSOL©, an equivalent 1D-model has to be generated and coupled with the 2D-model of the magnet [37, 43]. Figure 3.2 shows the location of the quench heater at one half-pole of the LHC main quadrupole magnets and the equivalent 1D model of the quench heater.

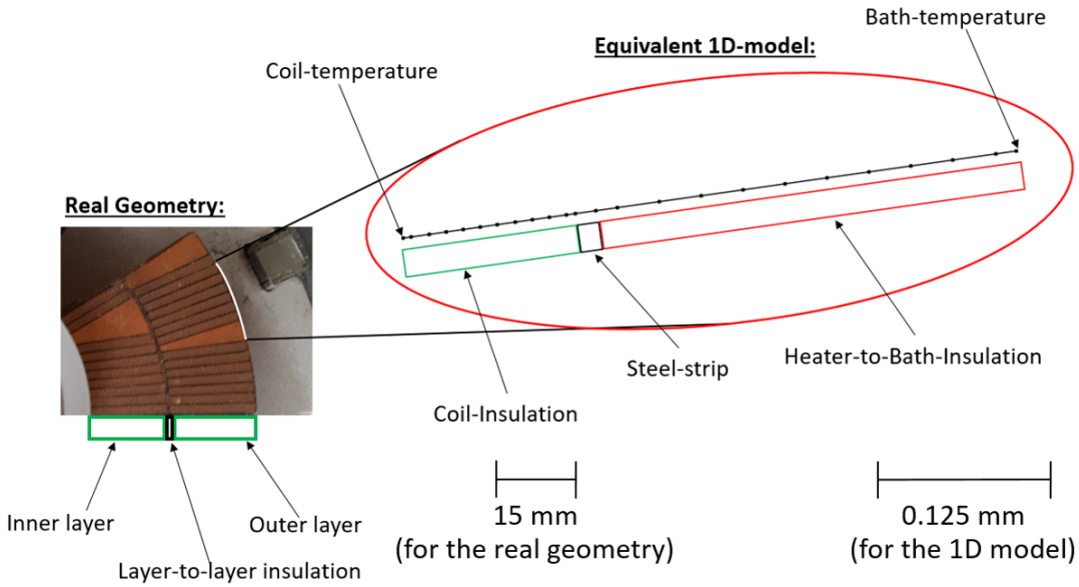

Figure 3.2: Location of the quench heaters in the cross section of the LHC MQ magnet with the equivalent 1D model

This equivalent 1D model was generated in both programs that are used for modeling the magnet behaviour, coupled with the 2D magnet models and verified within simulations, to check the expected behaviour. In figure 3.2 it can be noticed that the quench heater consists of different material layers. For the LHC main quadrupole magnets the steel strip is the actual heating part. The heating steel strip is insulated on both sides with kapton. To the coil it is insulated with $s_{\mathrm{ins,coil}} = 125$ μm and to the helium bath with $s_{\mathrm{ins,bath}} = 500$ μm [9]. The quench heaters are only glued to the outer layer of the cable coil and the positions of all quench heaters, located at both apertures within the LHC main quadrupole magnet cold mass, are visible in figure 3.3.

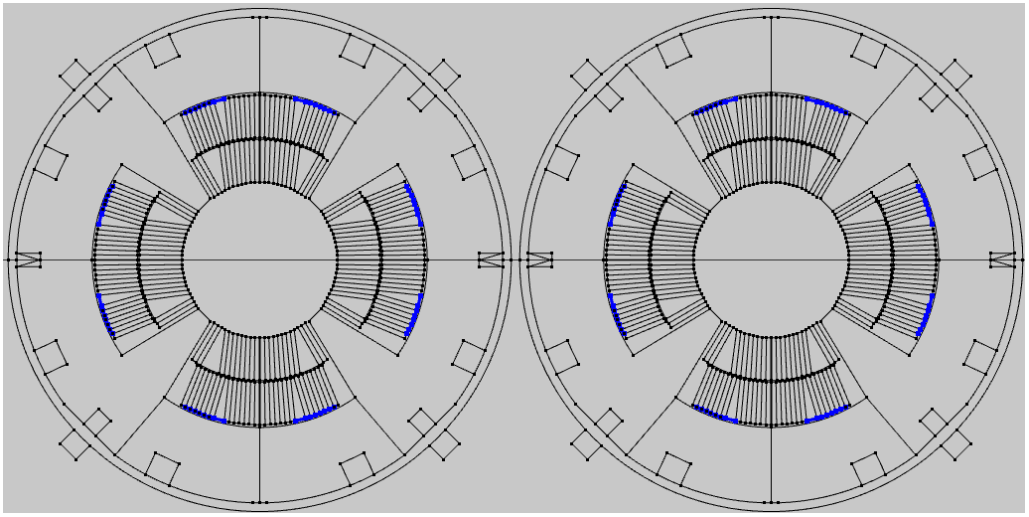

Figure 3.3: Location of the quench heaters (blue) in the cross section of the LHC main quadrupole cold mass. Window from the COMSOL© Program

3.1.3 Heat transfer within the magnet model

Due to the initially quenched hot-spot or due to the triggered quench heaters, heat is deposited within the outer layers of cable coil. For this reason, modelling the correct heat transfer is very important. The heat coming from the quench heaters propagates along the outer cable layer and from the outer layer to the inner layer. Thus, without the manually added heat transfer between the cable layers the half-turns within the inner layer could not heat up and quench. Thus, the energy stored in the magnet ($E_\mathrm{m} \approx 0.8$ MJ [9]) could not be distributed within the cable volume, which would cause mismatches between simulated and measured signals. Equation 3.5 describes the general equation that is used in both program, STEAM-SIGMA [4] and STEAM-LEDET [6, 7], to model heat transfer:

$$C_\mathrm{v}\partial_t T + \nabla \cdot \vec{q} = Q_\mathrm{if} + Q_\mathrm{is} + Q_\mathrm{eddy} + Q_\mathrm{ohm} \tag{3.5}$$

Here the heat stored in the system is described by $\rho C_\mathrm{p}\partial_\mathrm{t}\mathrm{T}$, with ρ as the material density and the second part $\nabla\cdot\vec{\mathrm{q}}$ is describing the heat flux [4]. On the right sight of the equation the heat sources are summed together. The ohmic losses Q_ohm are related to the moment, when the superconducting material loses the superconducting state and starts developing a resistance. The losses proportional to eddy-currents are summarized within Q_eddy. The contributions from inter-filament and inter-strand coupling losses are summarized within Q_if and Q_is, respectively.

Within the cable itself, the specific heat capacity is calculated as the sum of the heat capacities of different components within the superconducting cable, multiplied with the fractions of these components. The specific heat capacity per unit length of the cable half-turns C_tot [J/(mK)] is described within equation 3.6. It can be calculated as the weighted average, using the given specific heat capacities for the stabilizer (here copper) $c_\mathrm{v,Cu}$ [J/(m^{3}K)], the superconductor $c_\mathrm{v,sc}$, the internal voids $c_\mathrm{in,voids}$, as well as the external

voids $c_{\text{ext,voids}}$ and the insulation c_{ins}. Additionally, this weighted sum has to be multiplied with the insulated cable surface $\Omega_{\text{cable,ins}}$ [m^2]. The surface $\Omega_{\text{cable,ins}}$ can be estimated using equation 2.8.

$$C_{\text{tot}} = (f_{\text{Cu}}c_{\text{v,Cu}} + f_{\text{sc}}c_{\text{v,sc}} + f_{\text{in, voids}}c_{\text{in, voids}} + f_{\text{ext, voids}}c_{\text{ext, voids}} + f_{\text{ins}}c_{\text{ins}})\Omega_{\text{cable,ins}} \quad (3.6)$$

Moreover, copper wedges play an important role within heat transfer modelling and have to be discussed more in detail. The copper wedges are necessary for providing the circular form of the magnet. Looking at the temperature distribution in the magnet cross section, the copper wedges have a much higher thermal conductivity, than niobium titanium at cryogenic temperatures. Corresponding to [44], the thermal conductivity of copper is approximately 400 times higher than the conductivity of niobium titanium at cryogenic temperatures. This is important to know due to the fact that the superconducting strands are embedded within a resistive copper matrix.

Thus, including the copper wedges could be important for proper simulation the thermal distribution. The additional 1D resistance growth is the last modifications of the model, which is not done by default within STEAM-SIGMA. All magnet models are 2D models and thus the quenched part of the cable cross section implicates the complete half-turn immediately over the complete length to quench. To represent correct resistance growth of the hot-spot in the beginning part, additional 1D resistance growth is added within the 2D magnet model. This behaviour does not represent a complete 3D model of the magnet, but only a simplified combination of 1D and 2D.

3.1.4 Heat capacity of helium

Due to the large heat capacity of superfluid helium, the contact of the strands to superfluid helium effects the temperature growth within the cable strands and the discharge of the magnet. Moreover, due to the manufacturing process this volume is not constant and can vary even within one cable. This makes it challenging to estimate the correct volume fraction within the cable, which is probably filled with superfluid helium. To consider the influence of the helium fraction within the cable volume, a factor for the helium fraction is integrated within the magnet models in STEAM-LEDET and COMSOL©. This parameter allows to apply a homogeneous helium fraction for the complete cross section of the magnet. Due to the large heat capacity of superfluid helium, this parameter becomes very power-full for the simulations. To give an idea of the influence of this parameter, the heat capacity of helium for both programs, STEAM-LEDET and COMSOL©, is shown as a function of temperature in figure 3.4.

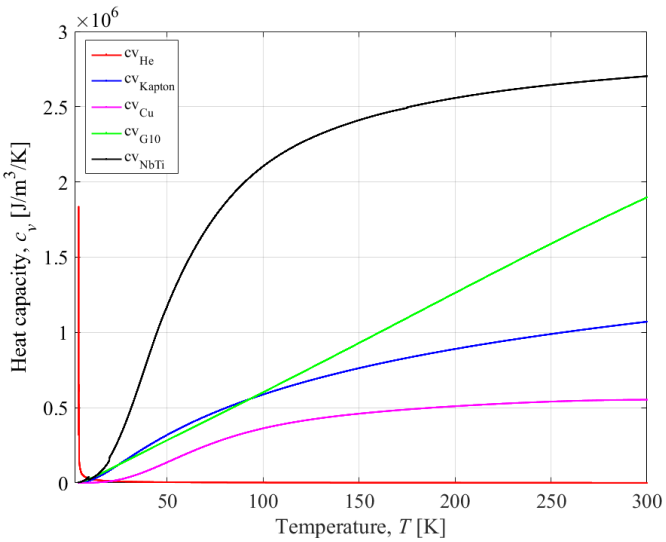

Figure 3.4: Heat capacity for several materials used within the 2D models [44].

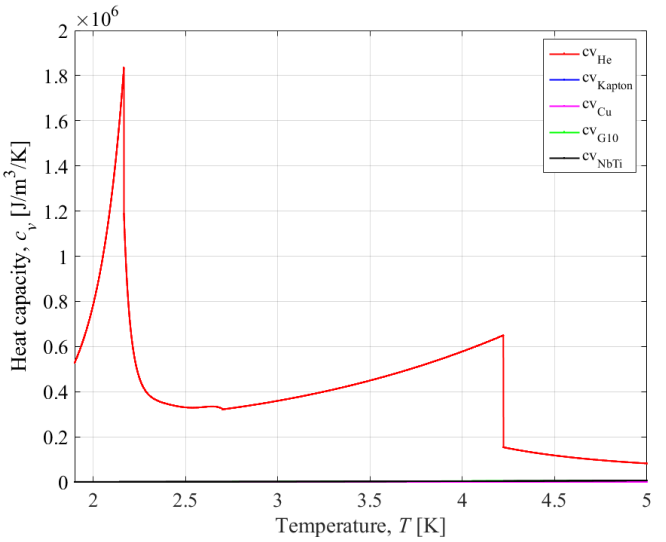

Figure 3.5: Heat capacity for several materials used within the 2D models [44]. Zoomed section between $T_{\mathrm{op}} = 1.9$ K and $T = 5$ K

From figure 3.4 and 3.5 it becomes clear that the heat capacity of helium behaves highly nonlinear between the operational temperature of $T_{\mathrm{op}} = 1.9$ K and T = 5 K. Within this temperature range the heat capacity of helium increases the required energy to quench a half-turn, because the large heat capacity extract the deposited heat very effective. Above 10 K the influence of helium becomes negligible. The rapid signal change within the plotted curve for helium between the temperature of 4 K and 4.5 K is due to the phase transition of helium from liquid to gaseous state. The correct amount of liquid helium within the superconducting cables cannot be measured and can vary due to tolerances within the cable manufacturing process. Thus, the correct estimation of the fraction of helium within a extracted magnet during a specific test or the magnet during the LHC operation process, relies on experience values and corrections during the simulation iteration process.

3.1.5 One-dimensional quench propagation

The next important point is the quench propagation along the cable length. It can be assumed that a local temperature rise (a so called hot-spot) will appear somewhere in the magnet. In detail, the tiny part of the superconducting wires within the strand will change from superconducting to normal state [12, 45]. The resistance of these wires in normal state is higher than the one from copper and as a result, the current will by-pass the superconducting wires and will generate ohmic losses in the copper matrix. Due to these effects, the quench can propagate along the cable length and along the cable width to the neighboring strands. The magnet models used in STEAM-LEDET and COMSOL© are 2D models. Thus, the quench propagation along the cable length is initially not considered. In this case, a tiny hot-spot in the cable can not be simulated, only a complete half-turn can be forced to quench over the complete magnet length. In the course of this thesis, a quench propagation function was developed and implemented in the magnet models from STEAM-LEDET and COMSOL©. The idea behind the implementation of this function is to represent more accurate the resistance growth of the hot-spot during a quench and the resistance growth after the quench heaters are triggered and start quenching the outer layer of the cable coil. Equation 3.7 shows the formula for calculating the quench propagation velocity in a superconducting cable [17].

$$v_{\mathrm{qp}} = \underbrace{J/(c_{\mathrm{v}}) \cdot \sqrt{\rho_{\mathrm{el}} k/(T_{\mathrm{s}} - T_0)}}_{\text{adiabatic quench propagation velocity}} \cdot \left((1-2y)/\sqrt{yz^2+z+1-y}\right) \tag{3.7}$$

Here J [A/mm^2] is the operating current density of the half-turns. The electrical resistivity of the material is given with ρ_{el} [Ωm] and the thermal conductivity with k [W/(mK)]. The initial operating temperature is represented by T_0 [K] and the temperature T_{s} [K] is the average temperature between the current sharing temperature T_{cs} [K] and the critical temperature T_{c} [K]. The critical temperature is the temperature at which the superconductor changes its state to normal conducting. This temperature depends on the field B [T] applied to the superconductor. The current sharing temperature is the temperature when the current stops passing only through the superconducting material, but also through the copper matrix. Within the copper matrix the current develops ohmic losses, which producing heat. The first and second part of the equation forming the adiabatic quench propagation velocity, which doesn't take into account helium cooling. To consider non-adiabatic behaviour, both factors y and z can be used, where y is the steady-state term and z is the transient term. Using both factors the status change in terms of heat transfer from steady-state to transient can be modelled. Estimating this parameters is not part of the thesis. Moreover, the realistic behaviour of helium within the cable, in case when a certain part of this cable quenches, is not well understood. For simulating of the helium behaviour detailed studies are ongoing at CERN. Thus, to develop a very precise analytic formula for the correct quench propagation velocity needs more preliminary investigation into this topic. But this investigation is not part of this thesis and thus the

correction factor according to helium cooling will not be considered. The adiabatic quench propagation velocity is written separately in equation 3.8 [17, 46].

$$v_{\mathrm{qp,ad}} = J/(c_{\mathrm{v}}) \cdot \sqrt{\rho_{\mathrm{el}} k/(T_{\mathrm{s}} - T_0)} \tag{3.8}$$

The individual temperatures required to estimate the adiabatic quench propagation velocity can be calculated using equation 3.9 up to 3.11 [17, 45, 46]. The temperature T_{s} can be calculated using equation 3.9.

$$T_{\mathrm{s}} = 0.5 \cdot (T_{\mathrm{cs}} + T_{\mathrm{c}}) \tag{3.9}$$

The critical temperature T_{c} depends on the normal magnetic field B and can be calculated using equation 3.10

$$T_{\mathrm{c}} = T_{\mathrm{c,0}} \cdot (1 - B/B_{\mathrm{c.20}})^{(1/n)} \tag{3.10}$$

Here $T_{\mathrm{c,0}}$ is the critical temperature at atmospheric conditions. The factor $_{\mathrm{c.20}}$ is the critical magnetic field at the same conditions. The current sharing temperature T_{cs} can be estimated with equation (3.11).

$$T_{\mathrm{cs}} = T_{\mathrm{c}} - (T_{\mathrm{c}} + T_0) \cdot \frac{J_{\mathrm{m}}}{J_{\mathrm{c,0}}} \tag{3.11}$$

Here are the temperature T_{c} is the previously estimated critical temperature, J_{m} the current density with respect to the conductor surface and the critical current density $J_{\mathrm{c,0}}$ at operating magnetic field and operating temperature.

3.2 Model generation using STEAM-SIGMA

STEAM-SIGMA [1] is a tool for automated generation of high energy accelerator magnets models. The idea behind STEAM-SIGMA is to ensure consistency between different tools and minimize the chance of input errors. The model generation occurs within a program IntelliJ IDEA©, which is an integrated development environment for Java. After all settings and updates are done, in principle two files are necessary for generating the model using IntelliJ IDEA©. The first file contains the cable parameters and the second file contains the description of the magnet geometry and the domain allocations. Within IntelliJ two files, the input file and the file with the cable parameters, are relevant for generating the file containing the model. The input file contains the geometrical information about the cable, the iron yoke and the air domains (see Annex for chapter 4). The general structure of the geometrical classification to form an element is shown in figure 3.6.

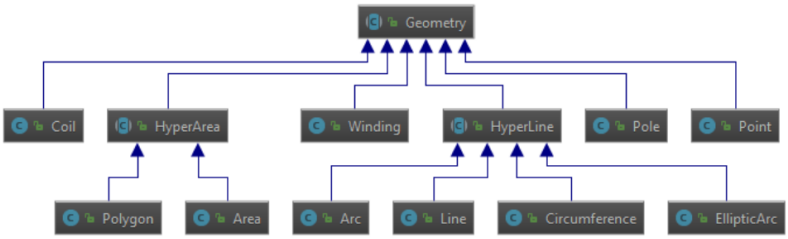

Figure 3.6: Class for the air domain within the input file

From figure 3.6 it becomes clear that different forms of HyperAreas and HyperLines can be used, which allows to generate complex geometrical structures in a simple way and is a big advantage of using STEAM-SIGMA© for the model generation. Another advantage is that material properties can also be assigned without extensive allocation within COMSOL©, but directly within STEAM-SIGMA© as well. The complete STEAM-SIGMA© classes used to generate the magnet model of the LHC main quadrupole magnets can be considered in the annex.

```
public Element[] air() {
    // POINTS

    double r = 1.0;

    Point kpc = Point.ofCartesian(0, 0);
    Point kp1 = Point.ofCartesian(r, 0);
    Point kp2 = Point.ofCartesian(0, r);

    // LINES
    Line ln1 = Line.ofEndPoints(kpc, kp1);
    Arc ln2 = Arc.ofEndPointsCenter(kp1, kp2, kpc);
    Line ln3 = Line.ofEndPoints(kp2, kpc);

    // AREAS
    Area ar1 = Area.ofHyperLines(new HyperLine[]{ln1, ln2, ln3});

    // ELEMENTS
    Element el1 = new Element("AIR_E11", ar1);


    // ELEMENTS DISTRIBUTED OVER QUADRANTS
    Element[] quad1 = {el1};

    return new Element[]{el1};
}
```

Figure 3.7: Structure of geometrical elements within STEAM-SIGMA [37]

The Element[] structure of the method air() is visible within figure 3.10. Every element contains points that are combined to lines that are combined to areas and returning the respective element. In this case of the air() Element[], the first quadrant of a circle is defined. In the main class, which is necessary for starting the model generation, every element will be related to a domain with the specific material properties. After all elements within the input file for the magnet model are declared, the file with the specific cable parameters has to be generated. This file contains information about the cable, like the RRR value or the filament twist pitch. The list of used parameters is described within the Annex for chapter 4. As soon as the input file and the file with the cable parameters of the LHC main quadrupole magnet are defined, the model will be generated by starting the main class. The main class is not coupled to the magnet model, but is needed for parsing the configuration file and generating the magnet model for COMSOL©. After

the model is generated as an .mph-file, it can be opened with the finite element program COMSOL©. The limitations for STEAM-SIGMA© are for the moment the possibility to include 1-dimensional quench heater models and couple it with the 2-dimensional model of the magnet and the possibility to include copper wedges and heat transfer between the cable layers. These additional changes were done manually and are discussed in chapter 3.3.

3.3 Simulation of the magnet behaviour using the program COMSOL©

COMSOL© is a finite element program for multiphysical simulations. After the model is generated using STEAM-SIGMA, already first simulations can be done after opening the model for the first time in COMSOL©. Therefore, only the solver settings has to be initially set. During the automated configuration of the model within STEAM-SIGMA, the model already includes the thermal and the electromagnetic domain for the simulations. Within the generated COMSOL© model, also dynamic effects like inter-filament (IFCC) and inter-strand coupling currents (ISCC) within the conductor are present. The effects are very important during transient magnet behaviour, for example during the pre-operation cycle with high ramp rates. Particularly, for the LHC main quadrupole magnet model following modifications were added to generate more accurate model behaviour, which is important for the validation process in chapter 4. These modifications are as follows:

- Generating a 1D model of quench heaters and thermally couple it to the 2D model of the magnet
- Adding heat transfer between cable layers and poles to the LHC main quadrupole magnet model
- Adding copper wedges to the LHC main quadrupole magnet model
- Adding of additional 1D resistance growth

3.4 Magnet model generation and simulation using STEAM-LEDET

As explained above, a 2D magnet model can be generated with the application STEAM-LEDET [6, 7]. Within this application simulations can be done as well. LEDET stands for Lumped-Element-Dynamic-Electro-Thermal and this application does not use the method of finite elements, but uses the STEAM-LEDET method, where the electro-magnetic and the thermal domain is modelled by sub-networks of lumped-elements [7]. The STEAM-LEDET technique is shown within figure 3.8.

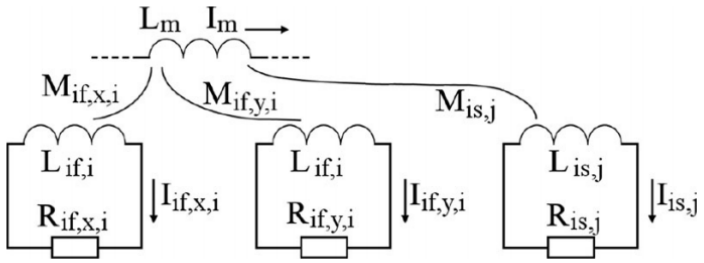

Figure 3.8: STEAM-LEDET technique [6, 7].

The STEAM-LEDET technique allows to model electro-magnetic and thermal transients in a superconducting magnet using a network of lumped-elements. In total three sub-networks are used to reproduce the completed behaviour during the simulation. The first two networks are reproducing the electrical transient behaviour in the circuit and the thermal transient behaviour in the cable cross section. The third network represents the electro-magnetic transient of the inter-filament (IFCC) and inter-strand coupling currents (ISCC) in the superconductor [19, 20]. The model and simulation parameters are defined in a so-called STEAM-LEDET input file. This input file contains the geometric and material parameters like strand diameters, number of strands in a cable, the RRR and others that were discussed in chapter 2. In contrast to the COMSOL© model, within STEAM-LEDET copper wedges are not included. The heat transfer between the inner and the outer layer of the cable coil don't have to be added manually, because it is already embedded within the definition of the thermal connections between the cable half-turns. The additional 1D resistance growth is also added within STEAM-LEDET and will be used as well for representing the first part of the resistance growth of the hot-spot. STEAM-LEDET will be used for the co-simulation together with the program PSpice©.

3.5 Generation of the circuit model within PSpice©

PSpice© is a program for generating and simulating of electrical circuit models. The circuit model will be generated as a netlist without using the graphical interface of PSpice©. A netlist is a description of the connectivity between different electrical parts within a circuit. A netlist contains basic electrical elements, like voltage or current sources, resistors, capacitors, inductors, and diodes. The following advantages are the reason for using netlists for simulating electrical circuits.

- Correction of mistakes within the circuit can be done very fast
- Generation of circuits with many identical components (i.e. magnet circuits) can be easily automated
- Change and adaption of circuits and circuit components can be done very fast

The disadvantage of using a netlist is the missing graphical user interface, which would guide the user through the settings and the simulation of the circuit.

3.6 Co-simulation of the magnet and the circuit model using COSIM

After the magnet and the circuit model are generated, both models will be combined within a co-simulation. By using COSIM, a purely electrical magnet model within the LHC main quadrupole circuit will be replaced by a magnet model coming from the application STEAM-LEDET. This is the advantage of using the co-simulation principle. The execution of the respective co-simulation part on the domain-specific software allows to run the co-simulation faster and to change and analyze each specific model. However, the most software does not support such multi-domain co-simulations, which force the user to have two programs. This can bee seen in general as a disadvantage. In the magnet model and the circuit model two modifications were added, to provide a co-simulation. In figure 3.9 the principle of signal exchange between the domains during a co-simulation is shown.

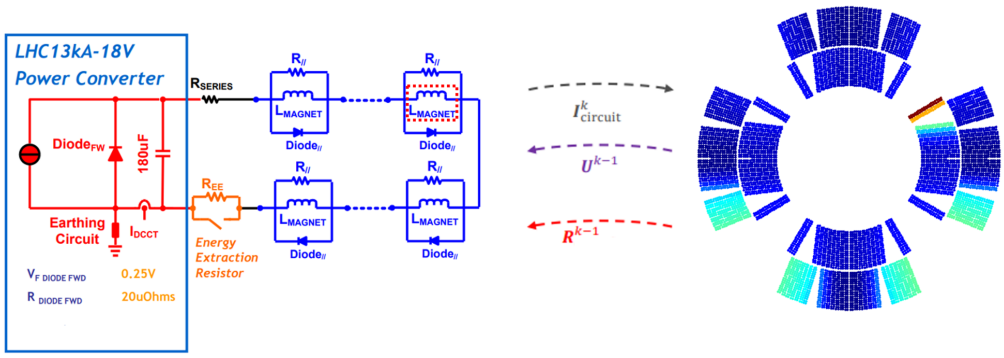

Figure 3.9: Working principle of the co-simulation on the example of the LHC main quadrupole circuit [28] and magnet

The circuit model is providing a calculated current to the magnet (field) model. And the field model uses the current to calculate a coil resistance and a voltage of the quenched magnet. The quenched magnet is marked in red in the circuit. The co-simulation starts with running the circuit for a defined time-window k with a defined time-step. After simulating the circuit model, PSpice© is providing a current value to the magnet model for STEAM-LEDET. In the next step STEAM-LEDET is running a simulation with this current value for the same time-window and provides a resistance and voltage value to the replaced electrical model within the circuit in PSpice©. The iteration within the time-window will be repeated until the convergence level in terms of the set relative and absolute error is achieved. The algorithm to provide the magnet and circuit coupling is called waveform relaxation [2]. This algorithm can be used in general, when the exchange of specific variables between domains or sub-systems is required. Start of the iteration is done by using an initial guess of the solution, implemented within the pre-conditioner. During the iteration steps better and better approximations of the results are reproduced within the algorithm over the entire time interval at once. Figure 3.10 shows the field and circuit coupling and the graphical representation of the algorithm [2, 47]. Figure 3.10

shows the field and circuit solutions according to the number of performed iterations.

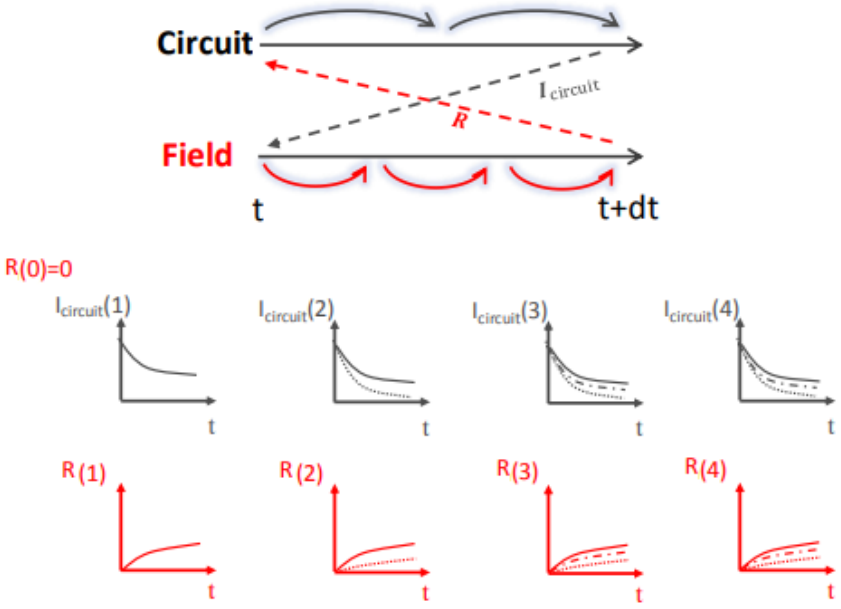

Figure 3.10: Field and circuit coupling within the co-simulation and the graphical representation of the waveform relaxation in a test circuit. [47]

Chapter 4

LHC main quadrupole magnet models

Within this chapter the generated LHC main quadrupole magnet models will be discussed and validated against test results done for extracted magnets in the CERN magnet test facility (SM18). In the course of the chapter the main parameters for the validation process and their influence on the simulation results will be discussed more in detail. The tests used for the validation were performed at a current level very close the nominal current level of $I_{\mathrm{nom}} = 11870$ A [9]. During the validation process the influence of several model parameters, like the helium fraction, the RRR, inter-filament- and inter-strand coupling losses will be investigated. Moreover, the influence of a new feature developed during the validation process will be discussed in detail. This additional feature affects the initial resistance growth in the magnet during a quench. The validation of the magnet model individually is needed to understand the magnet behaviour, proof the assumptions and model parameters, analyze its performance and provide the co-simulation with the correct magnet model. Finally, using more simulation results the behaviour of the magnet during the transient will be investigated further in detail.

4.1 Experimental and simulation setup

First, the experimental setup for testing this magnet and the effects in the magnet during a quench has to be discussed. Understanding the events in the magnet and the circuit allows to set correct the main parameters for the simulation and reproduce more accurately the magnet behaviour during the transient.

4.1.1 Experimental setup

In the LHC the main quadrupole magnets both apertures of one main quadrupole cold mass are connected within two separate circuits (focussing and de-focussing). For testing the magnet behaviour, several test were done one different magnets of the same magnet type (in this case quadrupole magnet). For the test, both apertures of the magnet were

connected in series to test the behaviour of both apertures. Thus, the inductance of the magnet due to this test is doubled. Figure 4.1 shows the simplified experimental setup.

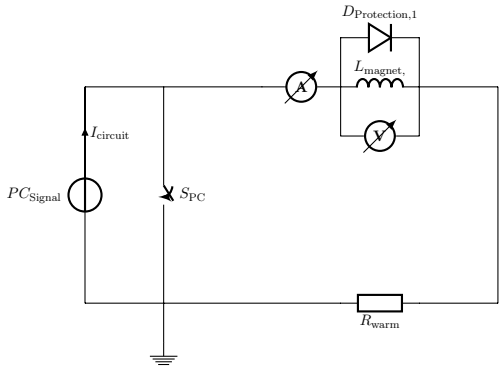

Figure 4.1: Experimental setup (simplified) for testing extracted magnets in the CERN magnet test facility

In figure 4.1 the magnet is represented as a simple inductance with $L_{\text{magnet}} = 11.2$ [mH]. For these specific magnet tests both apertures were connected in series, which doubles the inductance. Within the power converter PC_{Signal} an internal switch is used to open the power rack connection in case of a triggered fast power abort. The resistance R_{warm} of the circuit contains the resistance of current leads and connections to the power converter. The value of this resistance will be estimated by using measured current and voltage signals (see section 4.1.3). During the test the voltage across the magnet and the magnet current will be measured. The protection diode is embedded within the cold mass and will start by-passing the current when its opening voltage is reached.

For better understanding the behaviour of the magnet the events during the quench have to be described more in detail. As known from previous chapters, a quench is a phase transition from the superconductor to normal state. During the test or during normal operation in the LHC a quench can appear somewhere in the magnet. In normal state, the resistance of the superconducting filaments is higher than the resistance of the copper matrix in which the filaments are embedded (see figure 1.3). The current starts by-passing the filaments and flows through the resistive copper matrix, developing heat due to ohmic losses [7, 17]. This heat starts propagating along the cable with a certain quench propagation velocity [12, 48, 49] and heating up other parts of the coil. Together with the propagating heat, the resistance increases because more and more parts of the magnet are quenched. Together with the resistance also a voltage starts developing [12]. The voltage across the magnet is permanently measured during operation. When the voltage across the magnet reaches a threshold of 100 mV, the quench protection system is triggered. After the quench protection system is triggered two counteraction to the quench can be observed. First, the the quench heaters will be triggered and second, a fast power abort will be initiated with a certain delay. Within both models this delay was assumed to be 10 ms.

After triggering the quench heaters start heating up a part of the coil, so that the stored magnetic energy (about 0.8 MJ [9]) can be distributed in a large volume. This results into

a small temperature growth in a large volume, instead of an excessive temperature growth in a small volume. When the fast power abort is initiated, the internal switch within the power supply will open so that the power rack connection will be interrupted. In parallel, the switch S_{PC} will close generate a discharging loop for the magnet. The magnet discharges himself over the developing coil resistance and the warm resistance R_{warm} of the circuit.

4.1.2 Simulation setup

Since the behaviour of the magnet is described, optimal parameters have to be worked out to reproduce this behaviour within the simulation. Several assumptions and simplifications are present in the model physics (see chapter 3) and in the simulation setup. The first assumption is related to the quench. The location where the quench starts during the test (and during the operation of the LHC) is not known. However, it is more likely that the quench will start developing in the cables located within high field region [50]. Due to limitations of the superconducting state due to critical values of current density, magnetic field and temperature, the half-turns located at higher field carry a higher risk to quench [14]. It is not impossible that a quench could start in a area with lower field but as a first guess this assumption was used. The influence of several important model parameters has to be clarified in the following sections. Table 4.1 can be considered to compare the initial and final models parameters used for the simulation of the main quadrupole magnet models within COMSOL© and STEAM-LEDET [6, 51]. The final parameters were developed during the validation process due to parametric sweeps, optimization routines and discussions with quench protection system experts [34].

Table 4.1: Main simulation parameters for the first test at $I_{\mathrm{test,1}} = 11.69$ kA. Comparison between the first guess and final settings after optimization.

Parameter	**Initial parameters**	**Final parameters**
Warm circuit resistance, R_{warm}	0.63 mΩ	0.63 mΩ
Residual resistance ratio, RRR	209	**100**
Helium fraction, $frac_{\mathrm{He}}$	4.14%	**3.5**%
Initial hot-spot size, s_{hs}	10 mm	10 mm
Quench time of the hot-spot, t_{quench}	0 s	0 s
Quench propagation velocity, v_{qp}	-	**25 m/s**
Triggering time for the quench heaters, $t_{\mathrm{trigger,QH}}$	17 ms	17 ms

The value of the Warm circuit resistance R_{warm} is estimated by using the measured circuit current and the measured voltage (see section 4.1.3). This resistance remains due to connections between the cold circuit part like the magnet chain and the warm circuit part like the power converter. The RRR with a value of 209 was determined from measurements done for extracted strands from the cables 03C00312A and 03C00316B [52]. Therefore,

this value for the RRR was considered within the initial parameters. The helium fraction $frac_{\mathrm{He}}$ is the part of the insulated cable filled with superfluid helium (see section 4.1.2.1). It can be assumed that the quench starts with a hot-spot size of $s_{\mathrm{hs}} = 10$ mm at the time of $t_{\mathrm{quench}} = 0$ s. According to the measured voltage, the time when the quench heaters should be triggered ($t_{\mathrm{trigger,QH}} = 17$ ms) was approximately estimated. Initially, no function reproducing the longitudinal quench propagation was used. The assumption for a purely 2D model were present. In terms of quench propagation this means that a quench in some part of the half-turn quenches the cable along the complete length.

4.1.2.1 Estimating the fraction of helium within the cable for the simulation

The value of 4.14 % for the helium fraction is determined by the geometrical fractions of the superconductor, the copper and the insulation. As explained in chapter 2.2.1, the remaining void area can be calculated as the difference between the area of the bare cable and the area of the superconducting strands. The calculation of this area using the equations 2.2 up to 2.8 is the first part of estimating the helium fraction $frac_{\mathrm{He}}$ in the insulated cable. All following equations can be considered in [37]. First, the twist-pitch angle $\theta_{\mathrm{tp,st}}$ has to be calculated and used for the calculation of the strand area Ω_{st}.

$$\theta_{\mathrm{tp,st}} = \arctan\left(\frac{w_{\mathrm{bare}} - d_{\mathrm{s}}}{0.5 \cdot l_{\mathrm{tp,st}}}\right) = \arctan\left(\frac{15.1\,\mathrm{mm} - 0.825\,\mathrm{mm}}{0.5 \cdot 100\,\mathrm{mm}}\right) = 15.934\,[\mathrm{deg}] \tag{4.1}$$

$$\Omega_{\mathrm{st}} = \frac{1}{\cos\theta_{\mathrm{tp,st}}} N_{\mathrm{s}} \pi \left(\frac{d_{\mathrm{s}}}{2}\right)^2 = \frac{1}{\cos(15.934)} \cdot 36 \cdot \pi \left(\frac{0.825\,\mathrm{mm}}{2}\right)^2 = 20.0132\,\mathrm{mm}^2 \tag{4.2}$$

Since the area of the strands is calculated, the area of the bare cable is needed.

$$\Omega_{\mathrm{bare}} = w_{\mathrm{bare}} \cdot h_{\mathrm{bare}} = 15.1\,\mathrm{mm} \cdot 1.48\,\mathrm{mm} = 22.348\,\mathrm{mm}^2 \tag{4.3}$$

As explained in chapter 2.2.1, the void area is the difference between the area of the bare cable and the area of the strands. For the cable used for the LHC main quadrupole magnet this area can be calculated as shown below.

$$\Omega_{\mathrm{voids}} = \Omega_{\mathrm{bare}} - \Omega_{\mathrm{st}} = 22.348\,\mathrm{mm}^2 - 20.0132\,\mathrm{mm}^2 = 2.3348\,\mathrm{mm}^2. \tag{4.4}$$

The calculated value for Ω_{voids} is the total area of voids. This value has to be subdivided into the area of inner voids and the area of outer voids. For the first approximation to calculate the helium fraction $frac_{\mathrm{He}}$, the area filled with helium Ω_{He} [m^2] is considered to be the same as the area of the inner voids $\Omega_{\mathrm{in,voids}}$, calculated using equation 4.5.

$$\Omega_{\mathrm{in,voids}} = \frac{(n_{\mathrm{s,l}} - 1)(n_{\mathrm{l}} - 1)}{n_{\mathrm{s,l}} n_{\mathrm{l}}} \Omega_{\mathrm{voids}} = \frac{(18 - 1)(2 - 1)}{18 \cdot 2} \cdot 2.3348\,\mathrm{mm}^2 = 1.102575\,\mathrm{mm}^2 \tag{4.5}$$

Finally, the area of the insulated cable has to be calculated. This can be done by using equation 2.8.

$$\Omega_{\text{cable,ins}} = (w_{\text{bare}} + 2w_{\text{ins}})(h_{\text{bare}} + 2h_{\text{ins}}) = 26.7\,mm^2 \tag{4.6}$$

Here the narrow and the wide side of the bare cable are given from the cable properties with $w_{\text{bare}} = 15.1$ mm and $h_{\text{bare}} = 1.48$ mm, respectively. The insulation is taken into account by using $w_{\text{ins}} = 0.11$ mm and $h_{\text{ins}} = 0.13$ mm. The fraction of helium can now be estimated with 4.7.

$$frac_{\text{He}} = \frac{\Omega_{\text{in,voids}}}{\Omega_{\text{cable,ins}}} = \frac{1.1026\,mm^2}{26.7\,mm^2} = 0.0414 \rightarrow 4.14\% \tag{4.7}$$

4.1.2.2 Estimating the warm resistance from the experimental setup

The warm circuit resistance was calculated using the test current and the voltage signal before the fast power abort triggering, which were measured during the test as well. Using equation 4.8 the resistance value was calculated.

$$R_{\text{warm}} = U_{\text{meas}}/I_{\text{meas}} = 7.4\,\text{V}/11.69\,\text{kA} = 0.63\,\text{m}\Omega \tag{4.8}$$

4.1.3 Validation against test data

The validation process of the COMSOL© and STEAM-LEDET magnet models requires test data from specific magnet tests. Within this thesis, the following tests were used to validate the magnet model.

- MQLAD532-2-MQLAD532-2-A0606190953-a040-0-tdms ($I_{\text{test,1}} = 11.69$ kA)
- MQLAD532-2-MQLAD532-2-A0606190730-a030-0-tdms ($I_{\text{test,2}} = 7.5$ kA).

Here the validation against the first test is the most important one, because this test was performed at a current level very close to the nominal operating current level ($I_{\text{nom}} = 11.87$ kA). The validation against the second test will be discussed more in detail in section 4.1.4. These tests were performed with the same magnet and on the same day. Thus, it can be assumed that the test conditions are identical. Following signals were used for the validation:

- Measured current through the magnet over time,
- Coil resistance over time. This is deduced from the measured current and the measured voltage using: (U_{m} - $L_0 \cdot dI_{\text{m}}/dt$)/ I_{m} and is only an approximation value.

To call a model validated, in principle two criteria have to be fulfilled. The general shape of the signal should be reproducible and special important events should be represented

as good as possible with the model assumptions and simplifications. Figure 4.2 shows the comparison between the simulation results using the initial and final parameters (see table 4.1) together with the measured current during the first test. To see the important events in the beginning of the discharge, Figure 4.3 can be considered.

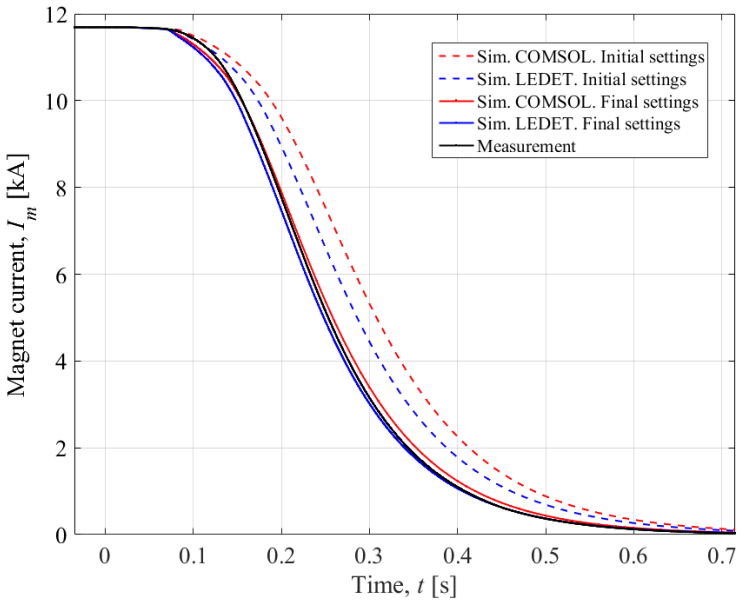

Figure 4.2: Comparison between the measured current and the simulated current STEAM-LEDET and COMSOL© for the initial and final set of parameters. $I_{\text{test},1} = 11.69$ kA, RRR and $frac_{\text{He}}$ corresponding to table 4.1

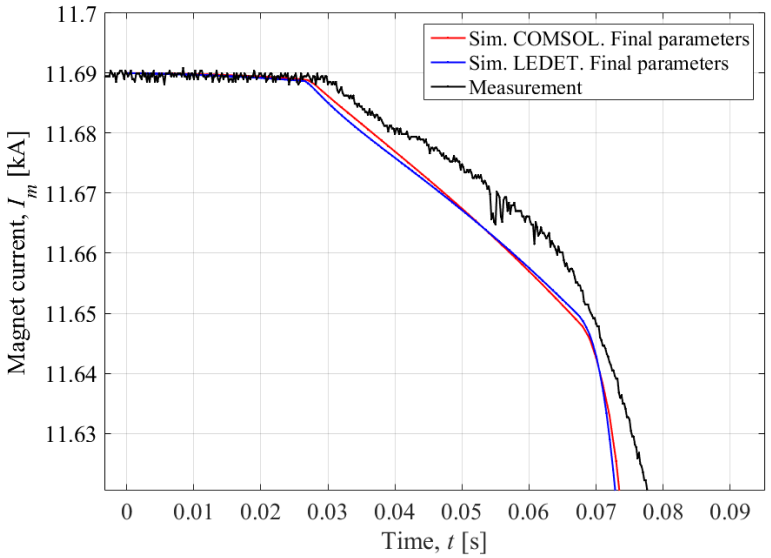

Figure 4.3: Comparison between the measured current and the simulated current STEAM-LEDET and COMSOL© for the final set of parameters. $I_{\text{test},1} = 11.69$ kA, RRR and $frac_{\text{He}}$ corresponding to table 4.1. Detailed view.

First, it can be noticed that the simulation results with the initial set of parameters

are in bad agreement with the measured current signal. After optimizing the parameters the simulation results coming from both programs match very well the measured current signal. Thus, the model validation against the data coming from the first test can be called validated. Although both models are based on two different principles because COMSOL© is using the FE-method and STEAM-LEDET is using the method of lumped elements, the successful validation can be achieved also with different program assumptions and simplifications. Second, the important events in the beginning of the discharge can be generally noticed looking at the current plot 4.3. The quench was set to start at t_{quench} = 0 s. The quench heaters were triggered at $t_{\text{trigger,QH}}$ = 17 ms and the fast power abort initiated at t_{FPA} = 27 ms. The significant start of the discharge can be noticed at t_{FPA}. Due to the delay that the heat coming from the quench heaters needs to migrate to the half-turns and quench them (heater-induced quench) can be considered as $\Delta t_{\text{QH}} \approx 48$ ms. It can be noticed that these events are almost identical within the measured current signal. Thus, not only the general shape of the simulation signal, but also separated events can be successfully reproduced. Moreover, the magnet current reaches 10 % (I_{m} = 1169 A) of the initial test current level within t = 0.394 s. This corresponds to a dI_{m}/dt of approximately 30 kA/s. The inductive voltage in this case is $U_{\text{ind}} \approx 330$ V. Based on the experience of quench protection and simulation experts from the PE section, several kilo-volts of inductive and resistive voltage can be reached across the magnet during the transient [34]. This interesting observation will be investigated more into detail within chapter 6.

Comparing the current discharge coming from the COMSOL© and STEAM-LEDET simulation still a small difference can be noticed. The simulated current from STEAM-LEDET discharges a bit faster than the one from COMSOL©. Within STEAM-LEDET the cable half-turns, which are usually located on both sides of the copper wedges (see figure 2.14), are directly connected within the model. As a result, the heat propagation from one half-turn to its neighbour is faster due to the absence of the copper wedges in the model. In contrast, within COMSOL© the heat has to pass through the copper wedge as well, which results in longer heat propagation time from one half-turn to the adjacent half-turn. After the simulated and measured current are discussed, the next important step is to compare the coil resistances coming from the simulations and estimated from the measured current and voltage signals (see figure 4.4).

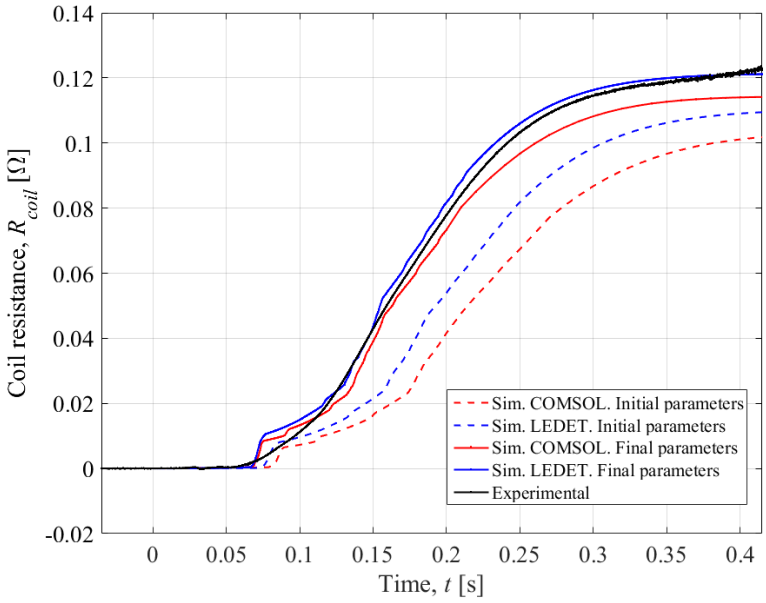

Figure 4.4: Comparison between the coil resistance estimated from measured values and the simulated coil resistance from STEAM-LEDET and COMSOL© for the initial and final set of parameters. $I_{\text{test},1}$ = 11.69 kA, RRR and $frac_{\text{He}}$ corresponding to table 4.1

With respect to the plot of the coil resistance it can be noticed as well that the initial set of parameters does not reproduce the behaviour of the coil resistance estimated from the measured current and voltage plot. The resistance value achieved with the initial set of parameters at t = 0.4 s from the STEAM-LEDET and COMSOL© simulations is $R_{\text{Coil,LEDET,0.4s}}$ = 0.1082 Ω and $R_{\text{Coil,LEDET,0.4s}}$ = 0.1011 Ω, respectively. This is a difference to the experimental value ($R_{\text{Coil,exp.,0.4s}}$ = 0.1215 Ω) of 11 % and 17 %, respectively. With the final set of parameters this difference coming from STEAM-LEDET and COMSOL© can be reduced to 0.5 % and 6.2 %, respectively. Thus, using the final set of parameters, an improvement can be achieved and the magnet behaviour can be better reproduced. Moreover, the difference between STEAM-LEDET and COMSOL© in terms of the current can be more clearly noticed within the resistance. As explained above, the absence of copper wedges in the STEAM-LEDET magnet model can be the reason for this difference. The initial part of the resistance plot simulated with the initial parameters, shows that the resistance growth starts 12 ms later than the resistance growth simulated with the final set of parameters. The initial part of the resistance plot will be discussed more in detail within section 4.1.3.5.

Another general comparison between the measured and simulated results can be performed by comparing the quench load of the different measurements performed on different LHC main quadrupole magnets at different current levels. The quench load is roughly proportional to the energy deposited in the hot-spot during the discharge and is calculated as:

$$QL = \int_{t_{\text{quench}}}^{\infty} I_{\text{m}}^2 dt \tag{4.9}$$

The value of the quench load calculated by using the measured current for the first test is $QL_{\text{meas}} = 26.49$ MA^{2}s. Using the final parameters of the simulated models a quench load of $QL_{\text{sim}} = 26.19$ MA^{2}s can be calculated. This corresponds to a difference of 1.13 % and is absolutely satisfactory.

To understand, how strong the influence of some of the main parameters and assumptions are on the simulation results, some simulations were performed with different parametric sweeps. The main parameters that require further investigation are listed below and will be discussed in detail:

- Influence of the RRR
- Influence of the helium fraction in the cable
- Influence of the IFCL and ISCL
- Influence of the Helium cooling
- Influence of the initial quench development

4.1.3.1 Influence of the RRR

As described above, the RRR value (Residual Resistance Ratio) can vary from magnet to magnet or even from inner to outer layer within one magnet. To see the influence of this parameter, three cases are simulated, with RRR = 100, 150 and 209. Figure 4.5 shows the simulated current results for the different cases for changing the RRR value together with the measured current. Figure 4.6 shows the estimated coil resistance from the measured current and voltage together with the simulated coil resistance.

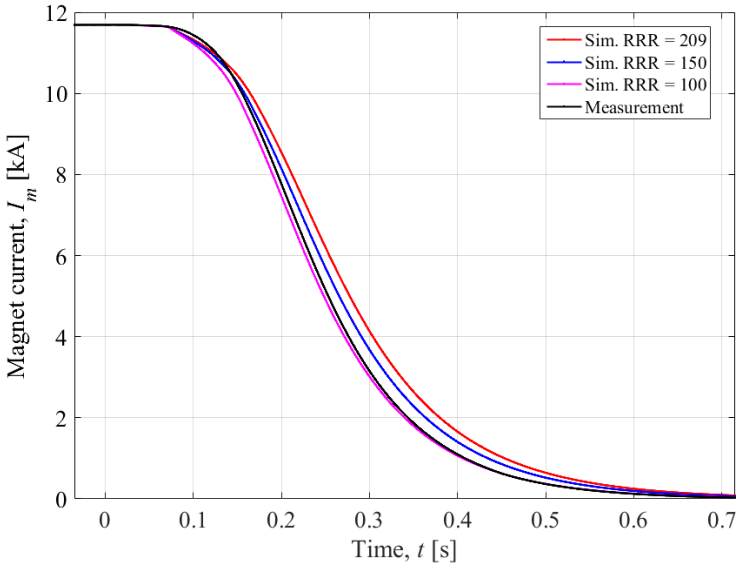

Figure 4.5: Comparison between the measured current and the simulated current from STEAM-LEDET. $I_{\text{test,1}} = 11.69$ kA. $frac_{\text{He}} = 3.5$ %. Parametric sweep of RRR

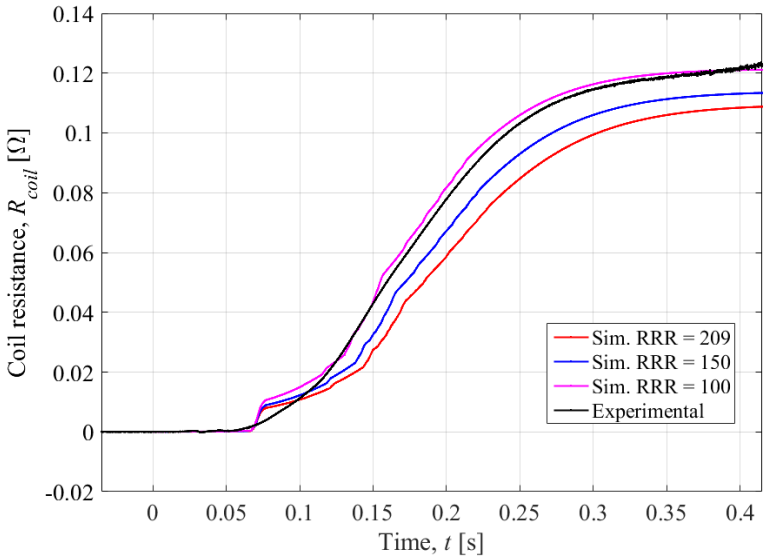

Figure 4.6: Comparison between the calculated coil resistance coming from the measured data and from the simulated data from STEAM-LEDET. $I_{\text{test},1} = 11.69$ kA. $frac_{\text{He}} = 3.5$ %. Parametric sweep of RRR

From figure 4.5 it becomes clear that the increase of the RRR value also increases the discharging time during the simulation. The reason for this behaviour is the fact that a higher RRR value represents a higher material purity and as a result a higher conductivity. Thus, the resistance per unit length of a conductor with lower RRR value is higher at cryogenic temperature and increases faster. This is confirmed with the figure 4.6, where the coil resistance over time for the different cases is shown.

Figure 4.6 shows that the resistance plot with an RRR value of 100 reproduces experimental coil resistance better than with the other RRR values. The initial value of RRR = 209 was coming from measurements done for extracted strands. Referring to discussions with simulation experts, the RRR for extracted strands is strongly depending on the cable manufacturing process. In example the outer layer of LHC the main dipole magnets and both layers of the LHC main quadrupole magnets are made of the same cable. For the outer layer of the dipole magnets it is known that the RRR value is 100. Thus, due to variation of the cable even within the magnet it can be assumed that the cable of the LHC main quadrupole magnet could have a RRR value of 100 as well. Thus, the value of RRR = 209 was not included within the final set of parameters. Besides the difference in the final resistance values, the time when the resistance starts instantaneously growing due to the heater-induced quench is identical for all three cases ($t_{\text{QH}} = 67$ ms). Thus, the RRR does not have an influence on the quench start, which is expected.

4.1.3.2 Influence of the helium fraction in the cable

The fraction of helium cannot be measured for a real magnet and is depending on the stability of the cable manufacturing process. Therefore, during the validation process this value was used as a fitting parameter. Due to the geometrical limit of 4.14 % for the area filled with helium in a 2D model, this parameter can vary between 0% and 4.14%. To

understand the influence of this parameter, three cases of different helium fractions were simulated within STEAM-LEDET. The results of these simulations are shown in figure 4.7.

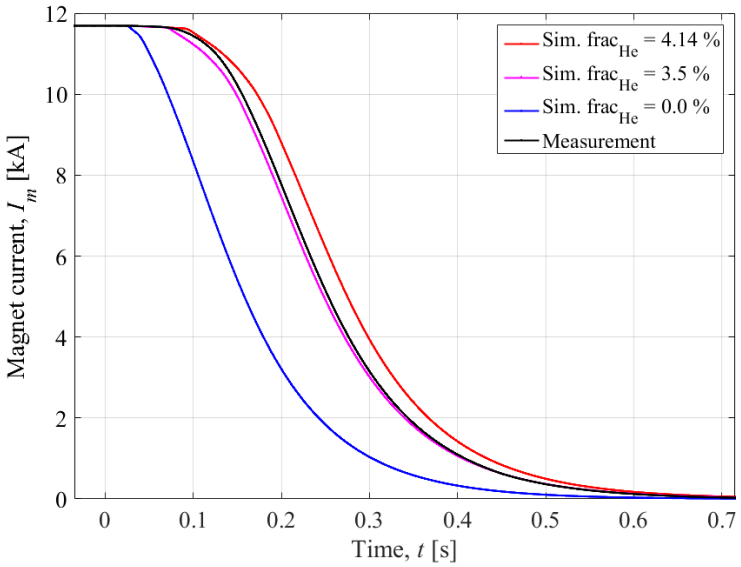

Figure 4.7: Comparison between the measured resistance and the simulated current from STEAM-LEDET. $I_{\text{test},1}$ = 11.69 kA. RRR = 100. Parametric sweep of $frac_{\text{He}}$

Figure 4.7 shows that the difference of a few percent within the helium fraction can completely change the simulation results. From figure 4.7 it can be noticed that the fraction of helium has an influence on the starting time of the discharge. Comparing the current discharge with 0.0 % helium and 3.5 % helium included in the model it can be noticed that the current signal with 0.0 % starts discharging almost immediately, due to heater-induced quench. In this case not much energy is needed to quench some parts of the magnet and introduce a discharge. In contrast, the quench heaters need more time for heating up some part of the coil because the present helium takes out the heating power which introduces a delay with respect to the simulation without helium. Due to the large value of heat capacity at cryogenic temperatures, helium has a large influence on the quench behaviour. Considering simulations with helium, the energy required for a quench increases by about a factor 10. Thus, the presence and the amount of helium in the model plays a significant role for the validation. In fact the helium parameter can vary between validation of different magnets even from the same magnet type, probably due to different cable manufacturing processes. The value of helium fraction that allows reproducing most accurately the experimental results is 3.5 %.

4.1.3.3 Influence of the IFCL and ISCL

The inter-filament coupling losses (IFCL) and inter-strand coupling losses (ISCL) are two contributions of transitory losses that occur in superconducting strand and cables due to magnetic-field variations. To see the influence of IFCC and ISCC, four cases were

simulated. Figure 4.8 shows the current discharge for the four different simulated cases.

- without IFCC, without ISCC
- without IFCC, with ISCC
- with IFCC, without ISCC
- with IFCC, with ISCC

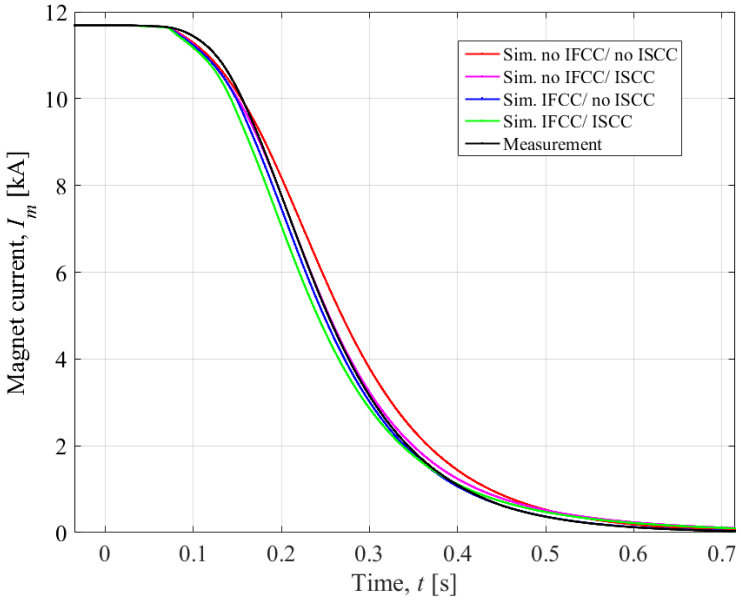

Figure 4.8: Comparison between the measured current and the simulated current from STEAM-LEDET. $I_{\text{test},1} = 11.69$ kA. RRR = 100. $frac_{\text{He}} = 3.5$ %. Parametric sweep of IFCC/ISCC

From the results in figure 4.8 it becomes clear that enabling and disabling of the different coupling losses has an effect on the simulation results in terms of discharging time. Due to the magnet current discharge, the local magnetic field in the superconductor changes. This change introduces coupling currents between filaments in a strand and contact point between strands in a cable [7, 17, 19]. The coupling losses introduced in a strand is proportional to the square of the total magnetic field change (see chapter 3.1.1). Comparing the case with only disabled IFCC and only disabled ISCC it can be noticed that the absence of IFCC has a stronger impact on the current discharge. This is due to the fact that the ISCC are developing slower with respect to the IFCC. Within COMSOL©, the option for enabling inter-strand coupling losses was not used, because implementation of this function considerably slows down the calculation. For this reason, in most STEAM-LEDET simulations the option of inter-strand coupling losses was also disabled, to make it comparable to the results coming from COMSOL©. The influence of the IFCC or ISCC can be underlined calculating the quench load. The quench load within the simulation results varies from $QL_{\text{no.IFCC,no.ISCC}} = 27.96$ MA^{2}s to $QL_{\text{IFCC,ISCC}} = 25.4$ MA^{2}s, which corresponds to a difference of about 10 %.

4.1.3.4 Influence of the Helium cooling

As explained in chapter 2, the superconducting coils are located in a helium bath. Within the magnet model used in COMSOL© and in STEAM-LEDET, the influence of helium cooling is disabled for the sake of simplicity. It is important to know how strong the influence of helium cooling is and how large the approximation error is, by neglecting the helium cooling effect. Thus, two cases were simulated, with and without helium cooling. Figure 4.9 shows the influence of the helium cooling in the model on the current discharge. The influence of the helium cooling effect is negligible and will not be used for the final validation model. In COMSOL© this option is not implemented as well.

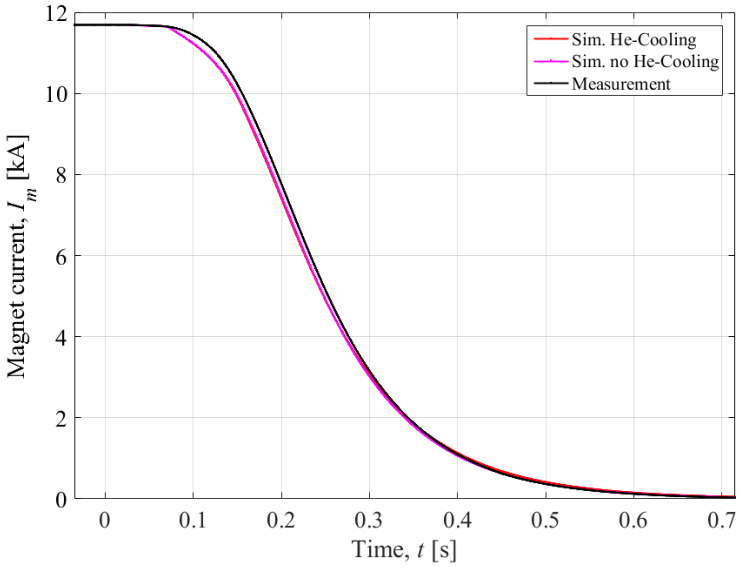

Figure 4.9: Comparison between the measured current and the simulated current from STEAM-LEDET. $I_{\text{test},1}$ = 11.69 kA. RRR = 100. $frac_{\text{He}}$ = 3.5 %. With and without helium cooling (He-Cooling).

4.1.3.5 Influence of the initial quench development

The hot-spot is the location where the quench starts. During the operation of the magnet, this hot-spot can appear anywhere in the cable, but the more likely locations are the half-turns which are located in the high magnetic field region. The quench propagation velocity is determined by the current I, the magnetic field B, the material and geometrical properties of the superconductor and the resistive copper matrix (see chapter 3.1.5). From this initially quenched hot-spot, the quench propagates longitudinally along the conductor and azimuthally and radially to adjacent half-turns across insulation layers. Figure 4.10 shows the magnetic field with the marked half-turn, which is set initially to quench at t_{sim} = 0 s.

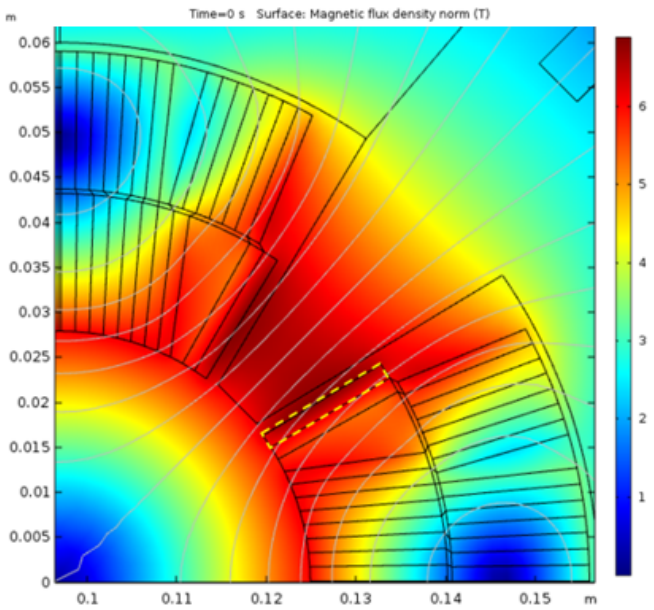

Figure 4.10: Cross section of one pole of the LHC main quadrupole magnet. Magnetic field with test current $I_{\text{test},1} = 11.69$ kA at $t_{\text{sim}} = 0$ s calculated with COMSOL©. Peak field in the conductor $B_{\text{peak,cond}} = 6.68$ T. Marked half-turn where the quench is set to start in the simulation

It is necessary to investigate, how significant the influence of the hot-spot is. Therefore, three different cases are simulated:

- No initial hot-spot,
- hot-spot develops simultaneously in the entire half-turn length (2D model),
- hot-spot grows with a finite propagation velocity of $v_{\text{qp}} = 25$ m/s ("2D + 1D" model).

In the first case, no half-turn within the magnet is set to be quenched initially. In this case the half-turns can be quenched due to quench heaters, due to heat propagation coming from the adjacent half-turns and by inter-filament coupling currents which develop as a reaction of magnetic field change during the discharge (see chapter 3.1.1). In the second case, the hot-spot is a fully quenched half-turn and only model assumptions related to a purely 2D model are present. Thus, when a half-turn quenches in the 2D model, it quenches over the complete length of the magnet. In the third case a new feature was developed for reproducing the initial resistance growth before the heater induced quench due to embedding of a quench propagation velocity. The quench propagates with a velocity of $v_{\text{qp}} = 25$ m/s at $t_{\text{sim}} = 0$ s. Figure 4.11 shows the simulation results for the different quench initiation cases of the initial hot-spot explained above.

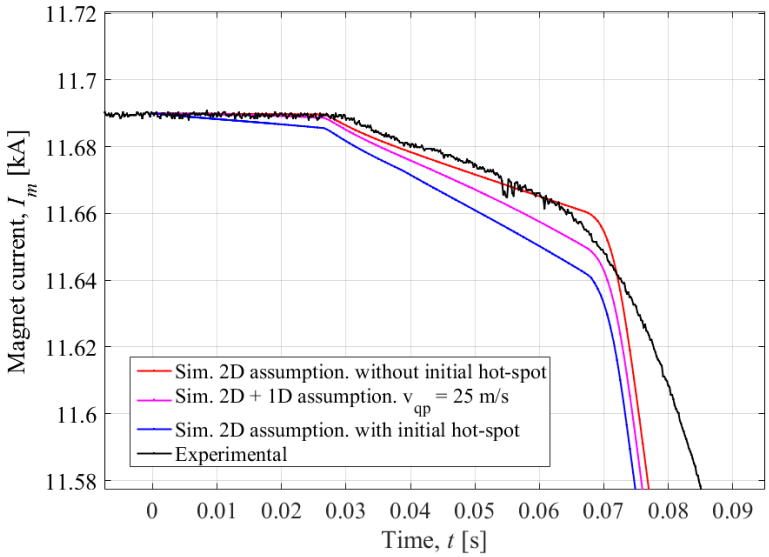

Figure 4.11: Current discharge for three cases of changed hot-spot behaviour for the LHC main quadrupole magnet. $I_{\text{test},1}$ = 11.69 kA. RRR = 100. $frac_{\text{He}}$ = 3.5 %. Parametric sweep of the hot-spot behaviour. Simulated with STEAM-LEDET.

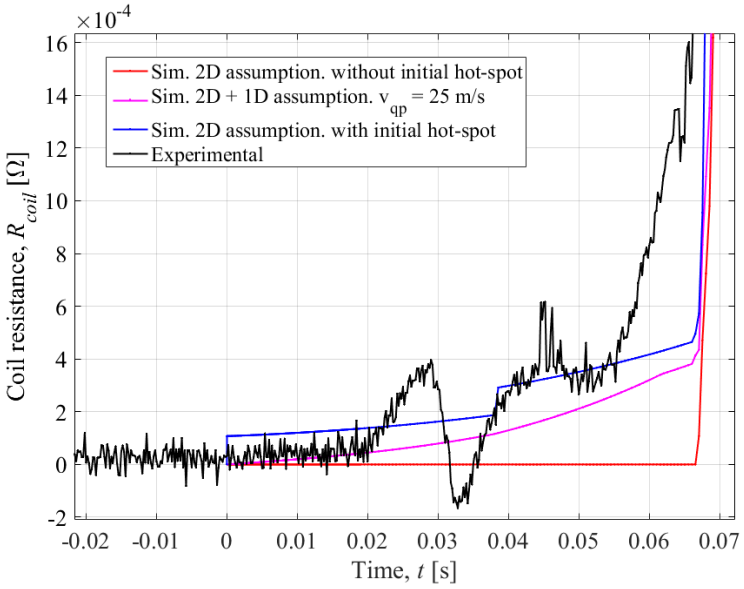

Figure 4.12: Coil resistance growth for three cases of changed hot-spot behaviour for the LHC main quadrupole magnet. $I_{\text{test},1}$ = 11.69 kA. RRR = 100. $frac_{\text{He}}$ = 3.5 %. Parametric sweep of the hot-spot behaviour. Simulated with STEAM-LEDET.

From the figures 4.11 and 4.12 it can be noticed that the quench initiation is determinant for the first part of the simulation. In figure 4.12 the plotted resistance of the case for the purely 2D assumption shows several jumps when the initial hot-spot is set to quench (t = 0 ms in figure 4.12) and when other half-turns are quenching due to heat transfer coming from the initial hotspot (t = 38 ms in figure 4.12). The approach for the quench initiation shows a very smooth resistance growth which in this sense is more realistic than instantaneous step-wise growth. The coil resistance value before the most part is quenched

by the quench heaters is $R_{\text{coil}} = 0.4$ mΩ for the approach using the quench propagation velocity.

4.1.3.6 Short summary of the validation process for the LHC main quadrupole magnet model

Within the previous sections the validation process against test data for the test done at $I_{\text{test,1}} = 11.69$ kA was successfully finished for both models coming from COMSOL© and STEAM-LEDET. This proves that both programs with different simplifications and embedded methods can provide a model representing the real magnet behaviour. The complete current behaviour and the detailed events in the beginning of the discharge, like introducing a fast power abort and a heater-induced quench can be reproduced with both models. Moreover, different parameters within the magnet models were discussed and a couple of parametric studies were simulated to see the influence coming from these parameters on the behaviour of the magnet during the discharge. The parameter that has the largest influence is the helium fraction. Changing this fraction by a few tenths of percent has a strong influence on the behaviour of the magnet. Due to the fact that the helium fraction within the cable can not be measured, it is not easy to predict this parameter correctly.

Besides the helium fraction, enabling or disabling the IFCC and ISCC has a not negligible influence on the behaviour of the magnet model during the discharge. Due to currently progressing changes regarding the implementation of ISCC within STEAM-SIGMA, the final validation model within COMSOL© just had the option for IFCC enabled, but for ISCC disabled. To guarantee consistency between the models, also in STEAM-LEDET the option for ISCC was disabled and for IFCC enabled. The influence of the helium cooling parameter is expected to be very strong, but figure 4.9 shows that the helium cooling does not have a large contribution to the behaviour of the magnet during the discharge. The RRR has a not negligible influence on the simulation results and as explained above, a value of RRR = 100 is present within the final validated model. Another important contribution for representing a more realistic behaviour of the magnet during the discharge comes from implementing a finite quench propagation velocity v_{qp}. From the figure 4.11 it becomes clear that the difference between a purely 2D model where a half-turn quenches over the complete length and the and where the quench propagates with $v_{\text{qp}} = 25$ m/s is not negligible and using the function for calculating the quench propagation velocity is an improvement for the model validation process.

During the parametric sweep of the helium fraction $frac_{\text{He}}$, it becomes clear that the best agreement can be provided with a helium fraction of $frac_{\text{He}} = 3.5$ %. The value of the RRR has changed from initially 209 to 100. This change is based to the fact that the RRR values can be different from the ones of extracted strands. The value of RRR also relies on the manufacturing processes of the superconducting cable and could vary with the manufacturer or even with the machine.

The values for the warm circuit resistance of $R_{\text{warm}} = 0.63$ mΩ and for the triggering

time for the quench heaters of 17 ms is calculated using the measured voltage. Thus, these two parameters do not have to be changed during the simulations.

It was clarified that the helium cooling has no significant impact on the discharge and the absence of helium cooling in COMSOL© does not produce a large error in the simulations. To provide consistency between the models, also within the model from STEAM-LEDET helium cooling was disabled.

4.1.3.7 Analysis of the transient effects during the simulation

The final combination of parameters for the validation of model was discussed above. Moreover, the influence from the main parameters on the simulation results were discussed. In addition, more interesting signals can be considered to prove the consistency of the model during the transient. Figure 4.13 shows the 2D plot of the half-turn peak temperature during the simulation. It can be noticed that some half-turns within the inner and the outer layer do not reach a temperature above 50 K. The parts quenched by the quench heaters reach a peak temperature of about 90 K. Only the hot-spot, which heats up its neighbouring half-turns, reaches about 180 K during the simulation time.

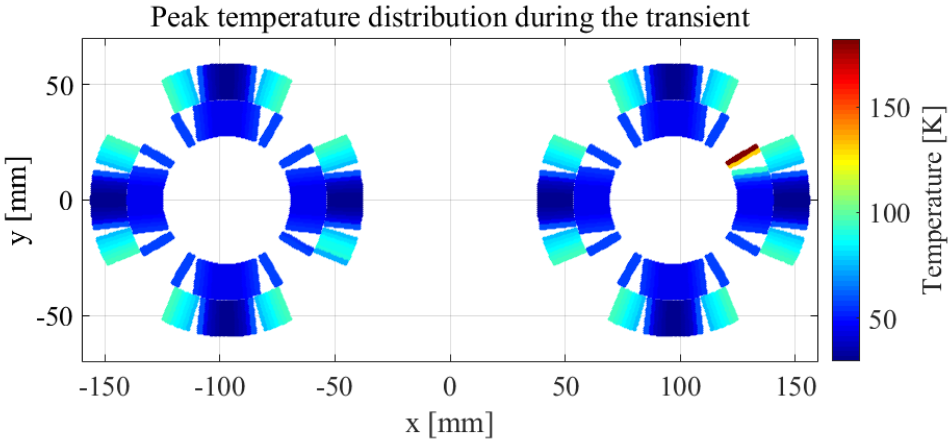

Figure 4.13: 2D peak temperature distribution during the transient simulation time. Simulated with STEAM-LEDET.

To see a more detailed temperature behaviour of the hot-spot and its neighbouring half-turns, the following figure can be considered. This figure shows the temperature plot over the simulation time. This plot can be considered to see, if the temperature behaviour shows instabilities over the simulation time. Thus, no unexpected behaviour can be noticed in figure 4.13.

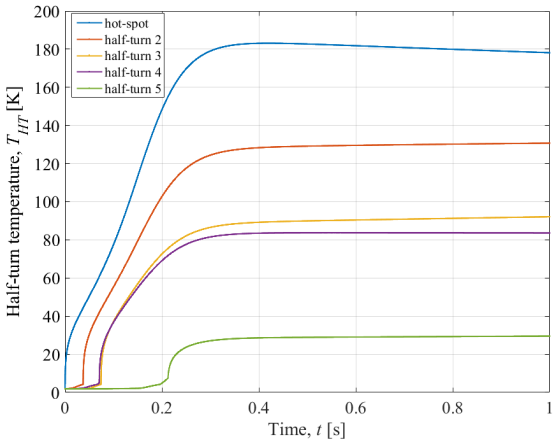

(a) Temperature plot over time for the hot-spot and other half-turns. Simulated with STEAM-LEDET.

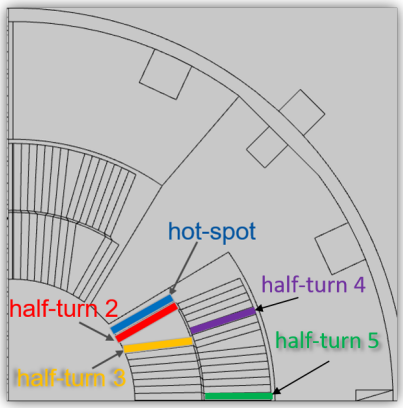

(b) Location of the hot-spot and the neighbouring half-turns within the magnet cross-section. Window from COMSOL©

Figure 4.14: (a) Temperature over time plot of the hot-spot and other half-turns (b) location within the magnet cross-section

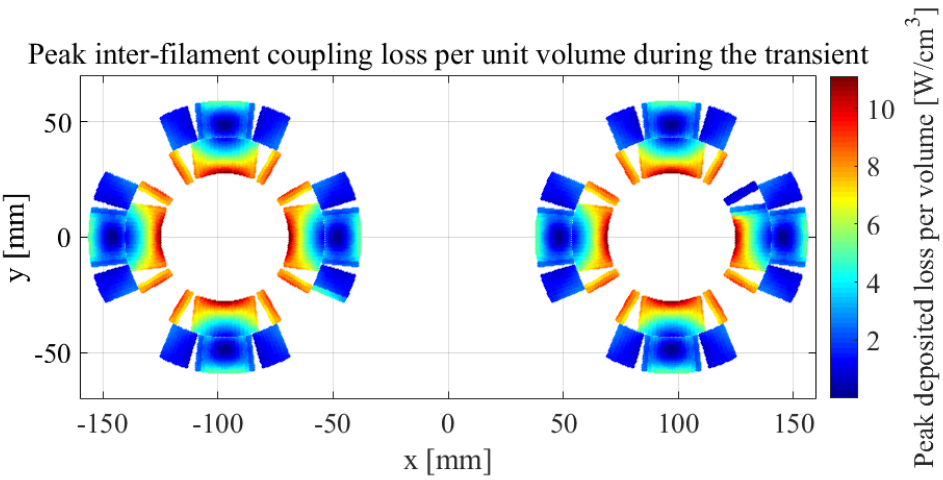

Figure 4.15: 2D peak IFCL distribution over the simulation time. Simulated with STEAM-LEDET.

The temperature growth during the transient for individual half-turns and their location in the cross-section can be noticed in figure 4.14 a and figure 4.14 b respectively. The hot-spot in example shows expected behaviour and quenches at $t = 0$ s. With respect to the hot-spot the adjacent half-turn is quenched by heat propagation after $t = 38.5$ ms. The next adjacent half-turn (half-turn 3) quenches with the same delay.

An Interesting observation is that the quenching time and the final temperature of half-turn 3 and half-turn 4 are almost identical. Half-turn 4 is one of those half-turn which are quenched by the heater-induced quench. The heater-induced quench occurs at $t_{\mathrm{QH}} = 71$ ms. The quenched half-turns (like half-turn 4) are transferring the heat through the insulation between the inner and the outer layer of the coil. In the same time, the

heat generated in the hot-spot is propagating to the adjacent half-turns and quenches them. Considering the time delay for quenching half-turn 5 shows how much time the heat need to propagate across the outer cable layer, quenching one half-turn after the other one. Moreover, due to the symmetrically heater-induced quench the complete magnet was transferred to normal state at $t \approx 200$ ms, while the magnet current at this time is still about $I_{\mathrm{m}} \approx 8$ kA. This also shows that the quench heaters alone do not provide a complete quench protection and the by-pass diode (see chapter **??**) is not less important than the quench heaters.

Another interesting result to discuss is the 2D plot of the IFCL. The IFCL occur due to a magnetic field change. Thus, they are higher where the magnetic field change is stronger. From figure 4.15 it becomes clear that this behaviour occurs also during the final simulation used for the validation of the magnet models. The highest IFCC are developed in the half-turns located in the high field area. It can be noticed that in the hot-spot and its physical neighbour, the IFCL are zero. The hot-spot was initially quenched and its neighbour was rapidly quenched by heat transfer coming from the hot-spot. Since this half-turns are already quenched, the current is bypassing the superconducting strands and no magnetic field change can introduce the IFCC that generate a field opposing the applied field change. Similar observations can be done for the half-turns which are quenched by the quench heaters.

4.1.4 Measurement and simulation at different current levels

The influence of the parameters explained above is tested for the test current level of $I_{\mathrm{test,1}} = 11.69$ kA. The model with the parameters provides very good agreement with the measured data. Thus, the model can be called validated for this current level. The current level can be changed to clarify if the model is valid for another current level. As explained above, the second test current level is $I_{\mathrm{test,2}} = 7.554$ kA. Within COMSOL© and STEAM-LEDET the same final validation settings were used according to table 4.1.

Figure 4.16 shows the comparison between the simulated and measured current discharge at the current level of $I_{\mathrm{test,2}} = 7.554$ kA. The simulation settings were taken from the previous validation at a test current level of $I_{\mathrm{test,1}} = 11.69$ kA. The parameter $v_{\mathrm{qp}} = 11.45$ m/s is recalculated due to the lower current level, and hence lower magnetic field at the hot-spot location. It becomes clear that a good agreement at a current level of $I_{\mathrm{test,2}} = 7.554$ kA is not achieved using the same parameters as for the validation at $I_{\mathrm{test,1}} = 11.69$ kA. The difference between the current plot coming from COMSOL© and STEAM-LEDET is nearly the same as for the previous test at $I_{\mathrm{test,1}} = 11.69$ kA. Thus, the model behaviour in both programs is consistent and their differences caused by the presence of copper wedges within the COMSOL© model and their absence in the STEAM-LEDET model. The discharge within the simulation results starts at the same time as in the measurement data, but the current from the simulations discharges more quickly. To match the measurement results, the helium fraction was increased to 6.5 % to let the simulation current discharge later. Figure 4.17 shows the current discharge of the simulated current,

compared to the measured one. To show the difference, the results from the model with $frac_{\mathrm{He}} = 3.5$ % are still present within figure 4.17.

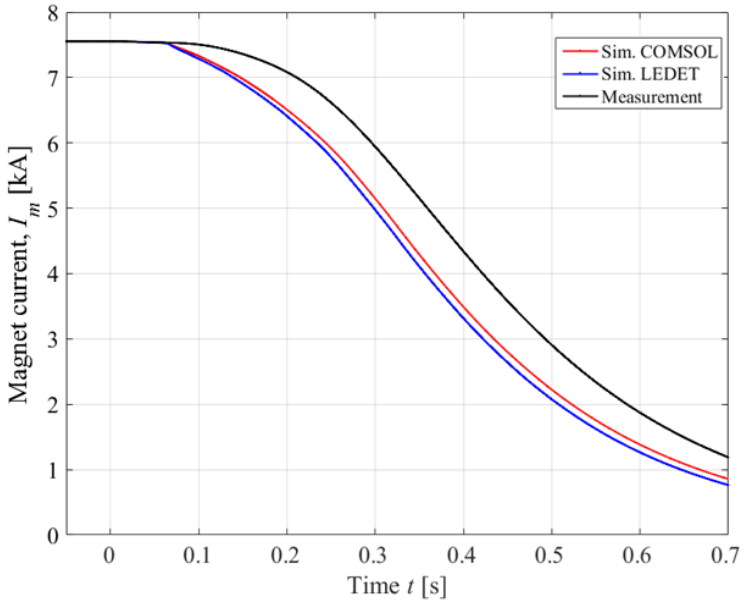

Figure 4.16: Comparison between the measured current and the simulated current from STEAM-LEDET and from COMSOL©. $I_{\mathrm{test},2} = 7.554$ kA. RRR = 100. $frac_{\mathrm{He}} = 3.5$ %

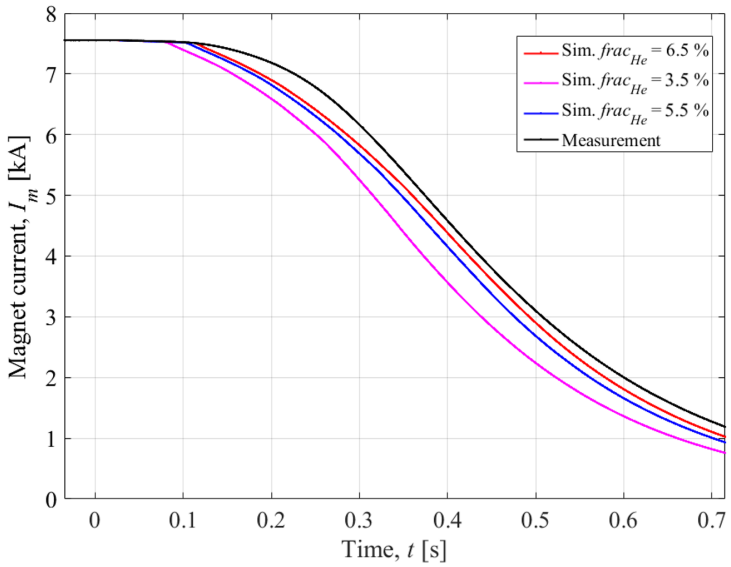

Figure 4.17: Current discharge with changed helium fraction. $frac_{\mathrm{He}} = 6.5$ %. $I_{\mathrm{test},2} = 7.554$ kA for the LHC main quadrupole magnet. Comparison between simulated and measured current. Simulated using STEAM-LEDET.

Figure 4.17 shows that increasing the helium fraction within the model and using the function for the quench propagation velocity, helps to match the measured current discharge. The reasons for the disagreement within the validation of the second test at lower current level have to be discussed in detail. In case of the second test at $I_{\mathrm{test},2} = 7.554$ kA one of the reasons for the disagreement between the simulated and the measured

current could be related to the behaviour of helium. In case of the first test at $I_{\text{test},1} = 11.69$ kA, the power within the start of the discharge could be large enough for heating up the helium more quickly, than within the test at $I_{\text{test},2} = 7.554$ kA. Thus, a helium fraction of superfluid helium is longer present and can take out the energy from the appearing hot-spot. In such a case it is probably worth to investigate the behaviour of superfluid helium within the cable during quench propagation.

Figure 4.18 shows the different quench loads calculated for tests performed on different main quadrupole magnets. In figure 4.18 it can be noticed that even for the same magnet type the differences within the quench load are not negligible. The variation of signals in terms of the quench load decreases with decreasing current. Thus, the influence of the parameters become less strong because the magnet can not be quenched that fast, as at high current. Looking at the spreading of the quench load calculated from the test results it becomes clear that also a variation between different magnets from the same magnet type is present. Thus, variations within the current discharge are not impossible for magnets from the same magnet type.

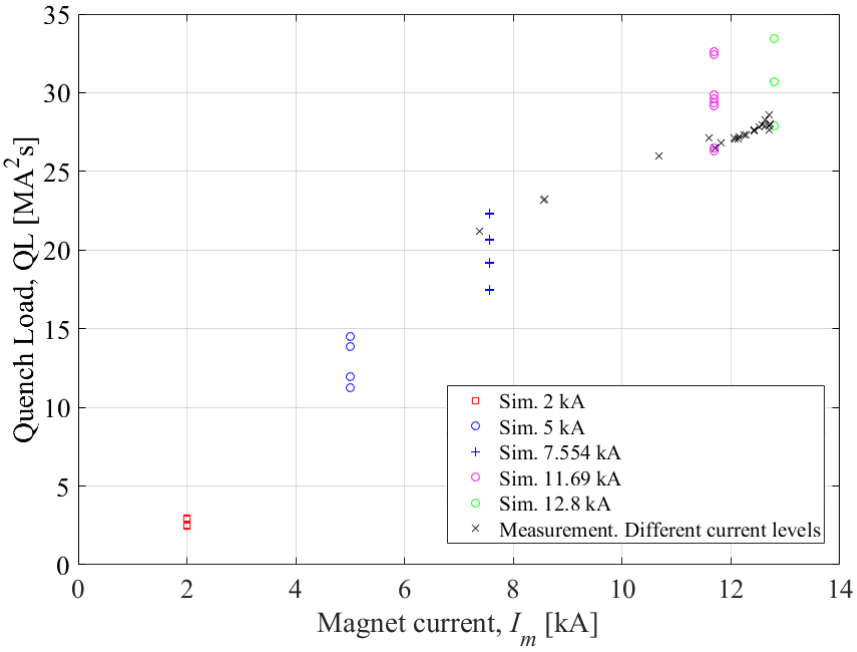

Figure 4.18: Quench-load over current. Comparison between simulation and determined from measurement. Parametric analysis including current change.

Chapter 5

LHC main quadrupole electrical circuit model

This chapter contains the explanations and assumptions for generating the LHC main quadrupole circuit model using the software PSpice©. As explained in chapter 3, PSpice© is a software for simulating analog circuit behaviour [53].

5.1 LHC main quadrupole circuit

The LHC main quadrupole circuit structure can be divided into the following parts (see chapter 2) [28]:

- power converter (PC),
- energy-extraction system (EE),
- main quadrupole magnets (MQ) and their protection system,
- earthing circuit (EC).

The generated models will be discussed within the following chapters.

5.1.1 Power converter

The main module of the power converter consists of different components within different hierarchic levels. The hierarchic structure of the power converter main module is shown in figure 2.2. The following chapters will contain explanations regrading the circuit models of the different hierarchical levels within the power converter main module.

5.1.1.1 Sub Sub Sub module of the power converter

The first hierarchic level according to figure 2.2 is the so-called the sub sub sub module. The main power converter module contains in total 60 sub sub sub modules. Other parts of the sub converter monitoring electronics (see figure 2.5) are not modeled. The following figure shows the circuit of the sub sub sub module, which is implemented as a netlist within PSpice©.

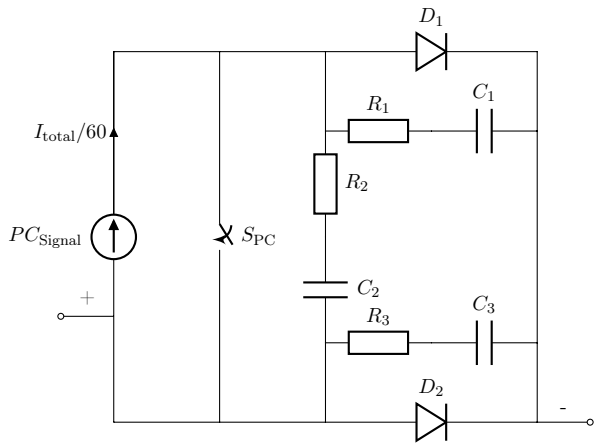

Symbol	Value	Unit
D_1	249NQ150	-
D_2	249NQ150	-
R_1	6.8	Ω
C_1	22	nF
R_2	6.8	Ω
C_2	15	nF
R_3	6.8	Ω
C_3	22	nF

Figure 5.1: Circuit model of the power converter sub sub sub module with value table

The current source contains a power converter signal, which is called PC_{Signal}. The current, coming from each of these current sources, is the total current I_{total} divided by 60, due to the number of sub sub sub modules connected in parallel. According to figure 2.5, the real component is inductively coupled with the sub converter electronics. In case of a fast power abort (FPA), the switch to the power connection rack will open. As a result, the inductive coupling is replaced with a short connection. In the PSpice© model this coupling is modelled by the switch S_{PC}, which is located on a parallel branch to the current source and will close at the same time. The realization of the circuit in figure 5.1 within PSpice© is shown in the Annex of this thesis. The included comments allow to follow the circuit structure.

During the operation of the circuit, the diodes D_1 and D_2 are getting the same current $I_{\text{total}}/(2 \cdot 60)$. If an FPA occurs, just a very tiny leakage current will pass in backward direction through diode D_2. Almost the complete current current $I_{\text{total}}/(60)$ will pass through the D_1 in forward direction, closing in such a way the discharging loop of the current [28].

5.1.1.2 Sub Sub module of the power converter

The next hierarchical level according to figure 2.2 is the power converter sub sub module. This module consists of four parallel connected sub sub sub modules and an additional LC-filter (see chapter 2.1.1). First, the circuit model of the LC-filter has to be discussed.

The circuit model of this LC-filter is shown in the following figure and the additional code listing in the Annex. Figure 5.3 shows the complete sub sub module, which consists of four parallel sub sub sub modules with the additional LC-filter.

The LC-filter consists of several parallel capacitor branches and inductors between the capacitor branches. Three resistors ($R_{\text{filter,1,2}}$, $R_{\text{filter,1,3}}$, $R_{\text{filter,1,4}}$) are connected in parallel with an additional capacitor ($C_{\text{filter,1,11}}$) form the end of the filter [28, 32]. The positive and the negative branch of the filter have a separate capacitance to ground with a parallel resistance. This parallel resistor is not a real component. The need of using this resistor is

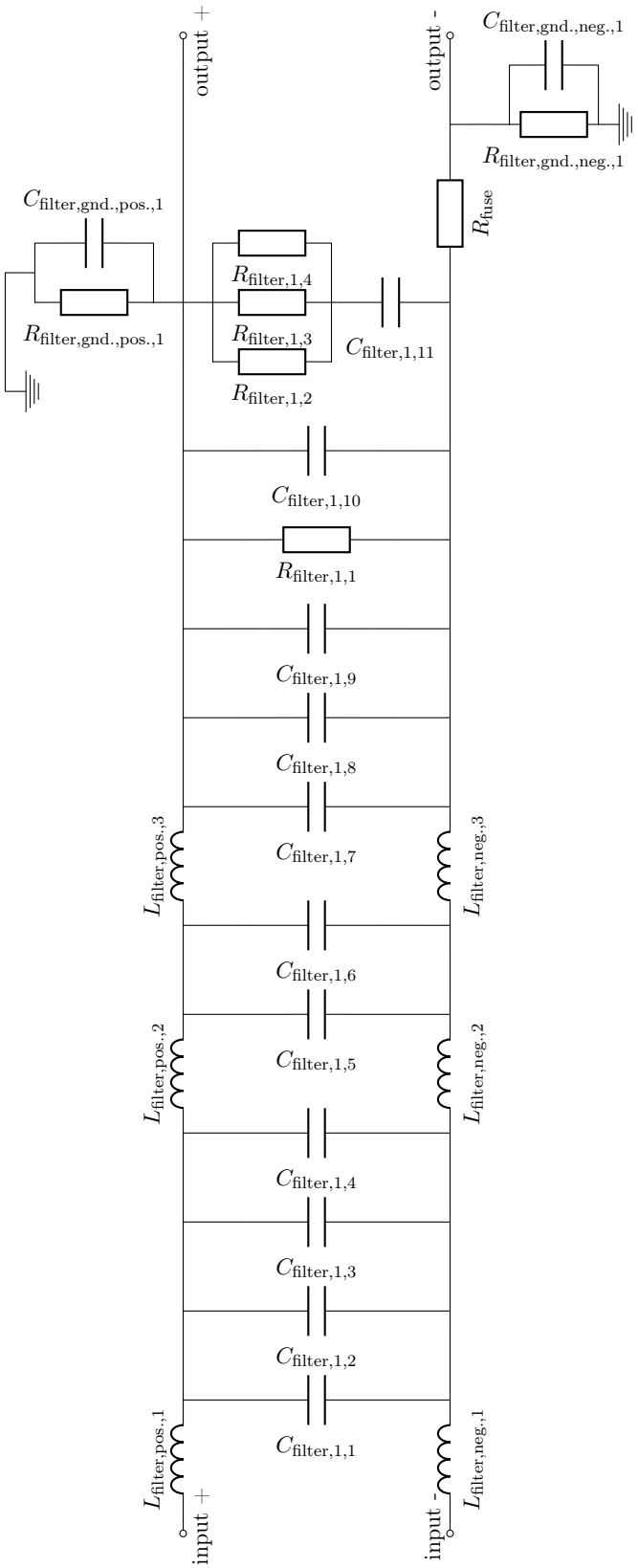

Symbol	Value	Unit
$L_{\text{filter,pos.,1}}$	670	nH
$L_{\text{filter,pos.,2}}$	200	nH
$L_{\text{filter,pos.,3}}$	200	nH
$L_{\text{filter,neg.,1}}$	670	nH
$L_{\text{filter,neg.,2}}$	200	nH
$L_{\text{filter,neg.,3}}$	200	nH
$C_{\text{filter,1,1}}$	470	μF
$C_{\text{filter,1,2}}$	470	μF
$C_{\text{filter,1,3}}$	470	μF
$C_{\text{filter,1,4}}$	470	μF
$C_{\text{filter,1,5}}$	470	μF
$C_{\text{filter,1,6}}$	470	μF
$C_{\text{filter,1,7}}$	470	μF
$C_{\text{filter,1,8}}$	470	μF
$C_{\text{filter,1,9}}$	470	μF
$C_{\text{filter,1,10}}$	10	mF
$C_{\text{filter,1,11}}$	10	mF
$R_{\text{filter,1,1}}$	100	Ω
$R_{\text{filter,1,2}}$	50	mΩ
$R_{\text{filter,1,3}}$	50	mΩ
$R_{\text{filter,1,4}}$	50	mΩ
R_{fuse}	10	nΩ
$R_{\text{filter,gnd.,pos.,1}}$	1	MΩ
$R_{\text{filter,gnd.,neg.,1}}$	1	MΩ
$C_{\text{filter,gnd.,pos.,1}}$	2.2	μF
$C_{\text{filter,gnd.,neg.,1}}$	2.2	μF

Figure 5.2: Power converter sub sub filter with value table

that in PSpice© a capacitance can not be connected to ground without a parallel branch, because the solver would categorize the connected node as a floating node and could not run the simulation. For that reason, a very large resistor (in this model the value of 1 MΩ) is used. During the validation of the circuit model, also the signals of the parallel capacitors within the LC-filter and the capacitors to ground has to be taken into account. Thus, correct modelling of these components is also very important.

The filter has two input nodes, which are connected to the four parallel sub sub sub modules. The two output nodes are connected with output nodes of other sub sub module filters. Figure 5.3 shows the sub sub module, which consists of four parallel-connected sub sub sub modules (see figure 5.1) and the previously discussed LC-filter, connected in series to them.

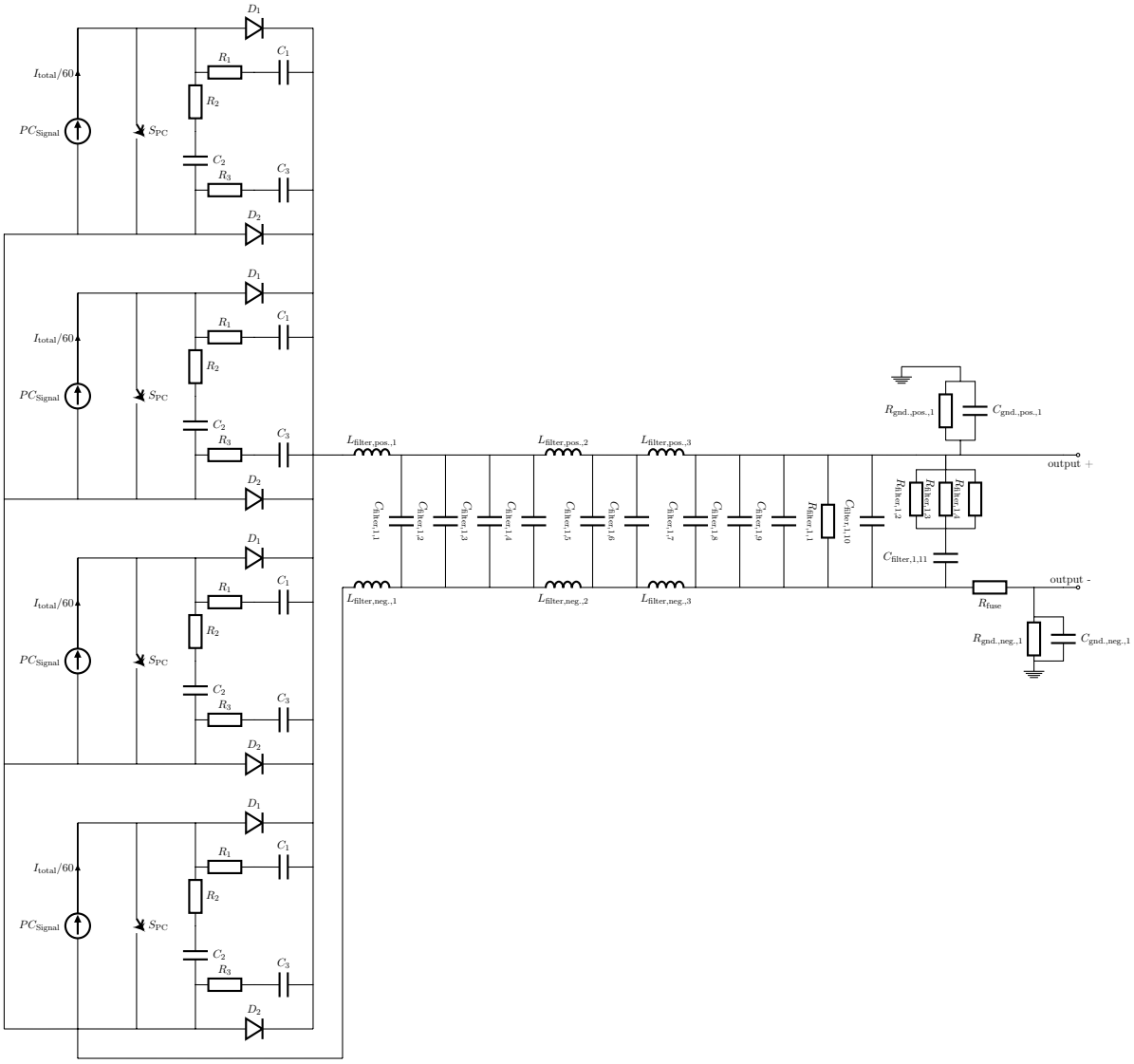

Figure 5.3: Circuit model of the power converter sub sub module

5.1.2 Sub module and main module of the power converter

The next hierarchical level is the sub module. The sub module consists of three parallel connected sub sub modules that are described above. The main module of the power converter is realized by connecting five sub modules in parallel with the main output filter. For reasons of comprehensibility, the schematics of the sub module and the main module are not shown within this chapter. The schematic itself does not provide any additional information, because it consists only of parallel connected modules that described above.

5.1.2.1 Main output filter of the power converter

Within the main module of the power converter the main output filter can be found. as explained in chapter 2, the main output filter is one of the parts of the power converter. The schematic of this output filter is shown in figure 5.4. The main output filter is connected in series with the four parallel-connected sub modules. The filter contains two branches (see figure 2.6) of diodes. 64 parallel-connected diodes forming the first diode branch (see figure 2.6). In addition to the first diode branch, three parallel disc diodes (third diode branch) and twenty parallel capacitors are located within this filter. The circuit of the main output filter is shown in figure 5.4.

Table 5.1: Value table corresponding to the main filter output module

Symbol	**Value**	**Unit**
C_1	18	μF
C_2	10	μF
R_1	150	$\mu\Omega$
R_2	100	nΩ
D_1	440CNQ030	-
D_3	SKN6000	-
$R_{\text{filter,gnd.,pos.}}$	1	MΩ
$R_{\text{filter,gnd.,neg.}}$	1	MΩ
$C_{\text{filter,gnd.,pos.,1}}$	9	μF
$C_{\text{filter,gnd.,neg.,1}}$	9	μF
$C_{\text{filter,gnd.,pos.,2}}$	2.2	μF

5.1.2.2 Earthing system

The next circuit model generated in PSpice© is the earthing system. The schematic of the real earthing system is shown in figure 2.7. The PSpice© model is a simplified version of this circuit and contains only the resistor branches and the current source. The schematic of the earthing circuit model is shown in figure 5.5.

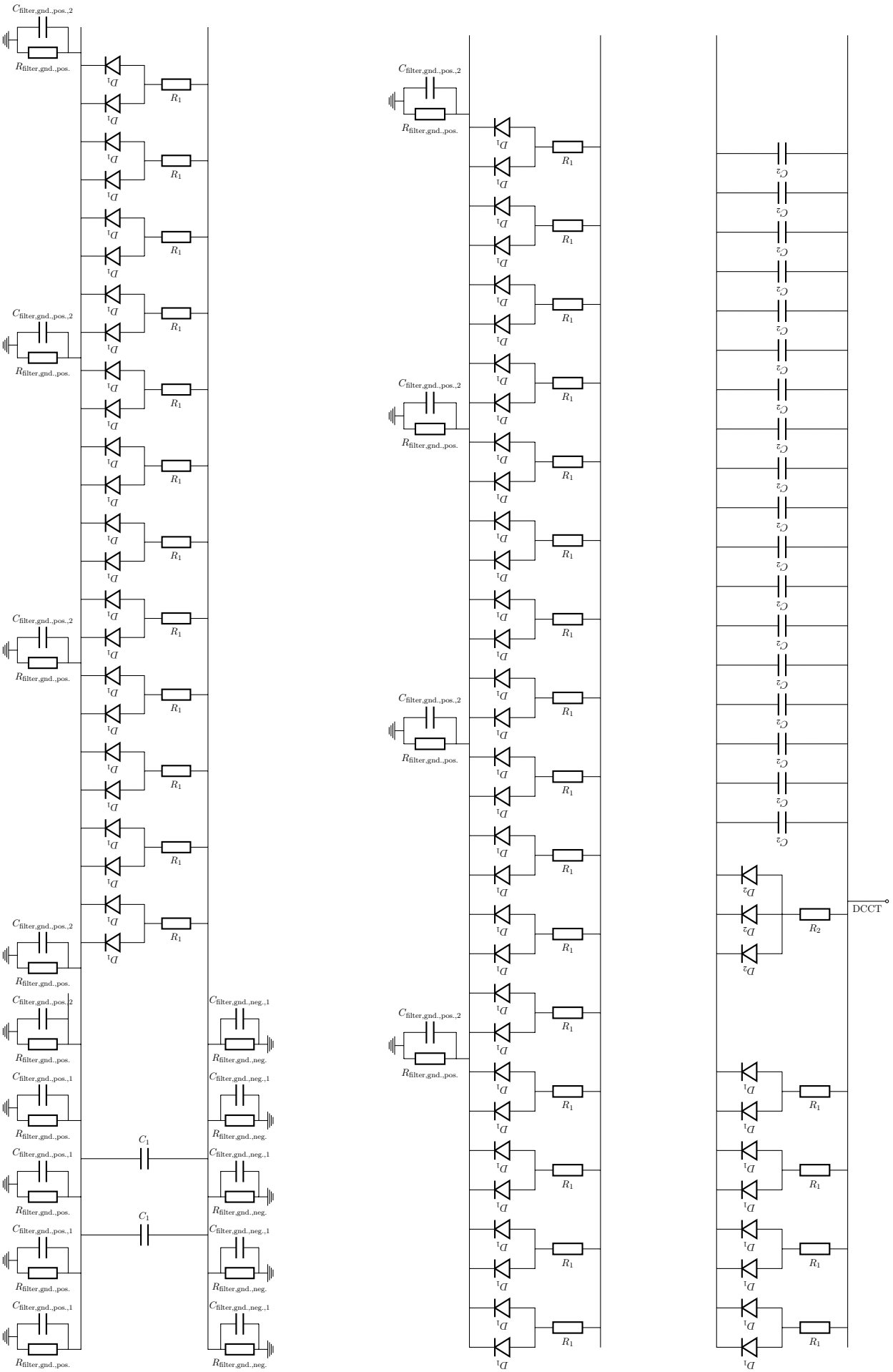

Figure 5.4: Power converter output filter with value table

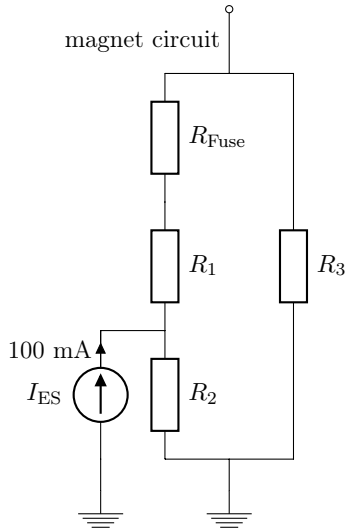

Symbol	Value	Unit
R_{Fuse}	100	nΩ
R_1	10	Ω
R_2	100	Ω
R_3	10	kΩ

Figure 5.5: Circuit model of the earthing system with the value table

During the validation procedure of the circuit model also the current to ground from different test campaigns is compared to the simulated current to ground.

5.1.3 Energy-Extraction-System

The energy-extraction system reduces the time constant during the discharge (see figure 2.8) and takes out (or dumps) the energy stored within the magnets. For that reason, the energy-extraction resistor is also called dump resistor. As explained in chapter 2, the energy-extraction system consists of four parallel-connected switch branches and the energy-extraction resistor in parallel to them. The opening phases of the switches are shown in figure 2.11. These opening phases are modeled with four switches in series within one branch. To model the opening time, a voltage source with a ramp signal is used. Every switch within a single branch will open at a specific voltage. The gradient of the signal is chosen in that particular way, so that the opening voltage of a specific switch is reached, when the particular phase opening time occurs (see figure 2.11). In addition to that, a parameter for the time delay of every switch is embedded in the model. The advantage of this solution, compared to the use of a stimulus, is the flexibility and the possibility to choose in example a parameter for a time-delay of a specific switch. Thus, a failure case can be simulated, in which one of the switches does not open or opens after a certain delay. In such a case, using parameters instead of using a Stimulus, allows to do many simulations with a parametric sweep without generating a new stimulus file for every simulation and every switch. Figure 5.6 shows the circuit model of the energy-extraction system and the value table. In addition to the ideal switches, which represent the opening phases, parasitic resistors and inductors are also included within the model of the energy-extraction system. The code listing of the energy-extraction system and the switches representing the opening phases, is located in the Annex.

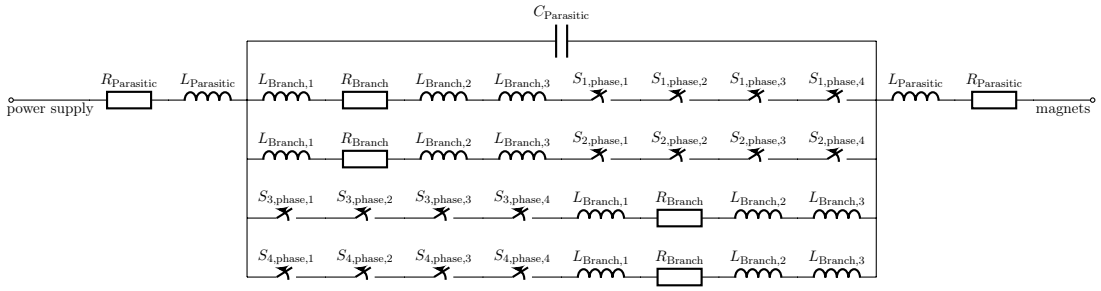

Symbol	Value	Unit
$R_{\text{Parasitic}}$	100	nΩ
$L_{\text{Parasitic}}$	2	μH
$C_{\text{Parasitic}}$	1.25	μF
R_{Branch}	80	μΩ
$L_{\text{Branch,1}}$	1.0	μH
$L_{\text{Branch,2}}$	1.7	μH
$L_{\text{Branch,3}}$	1.1	μH

Figure 5.6: Circuit model energy-extraction system with the corresponding value table

5.1.4 LHC Main quadrupole magnet

As explained in chapter chapter 2.2.1, both apertures within one common mechanical structure of the LHC main quadrupole cold masses are powered independently and belong to two separate electrical circuits. Thus, every aperture is protected independently by quench heaters and a by-pass diodes, working at a operation temperature of $T_{\text{op}} = 1.9$ K [9, 54]. Figure 5.7 shows the circuit model of the LHC main quadrupole magnet. The model is divided in eight half poles. Moreover parasitic capacitors to ground are implemented in the model, as shown in the following figure. Above the by-pass diode, a parallel resistor is located. This parallel resistor is not a part of the protection system, but reduces the high-frequency impedance of the magnet [34]. The complete inductance of one magnet is subdivided into eight inductors within the model. Every of these inductors represents a half pole. Above every second of these half poles, a resistor R_{Bypass} is located. By default this resistor is $R_{\text{Bypass}} = 1$ mΩ, but it could also be changed for simulate the effect of unbalanced magnets, which results in a different dynamic impedance behaviour. This effect was observed for the LHC main dipole magnets during the LHC operation in 2009 and 2010 [55, 56]. To keep the option for simulating this effect within the main quadrupole circuit, these resistors are included within the model.

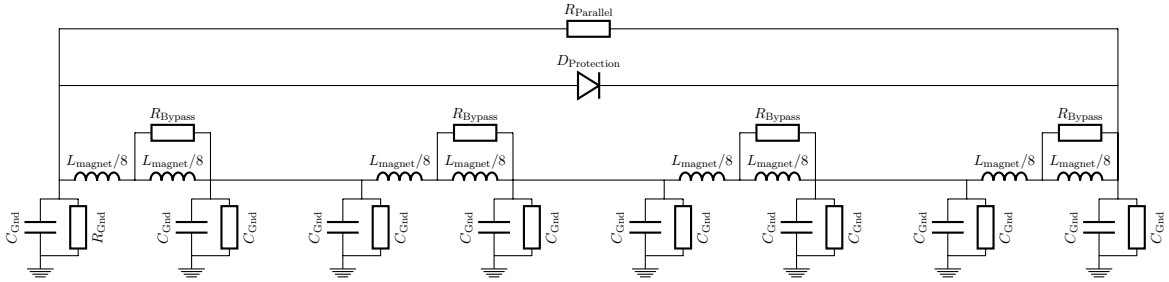

Symbol	Value	Unit
R_{Parallel}	20	Ω
R_{Bypass}	10	MΩ
L_{magnet}	5.6	mH
$D_{\text{Protection}}$		-
R_{Gnd}	10	MΩ
C_{Gnd}	11.25	nF

Figure 5.7: Circuit model of the LHC main quadrupole magnet with the corresponding value table

5.2 Validation of the LHC main quadrupole circuit

After the model of the circuit is generated, separate tests were performed to demonstrate the netlist for logical errors, missing components, model accuracy, other non-linear effects or wrong node numbers. Each sub circuit is tested independently and optimized until the correct, expected behaviour is simulated. These tests are an important part and a preparation for the validation phase of every model. If a circuit or sub-circuit contains failures, the wrong simulation results could introduce wrong interpretation and conclusions, which has to be avoided. However, all kind of different tests for sub circuits of the LHC main quadrupole circuit model are not described within the thesis. The focus is the validation procedure of the LHC main quadrupole circuit against test data.

5.2.1 Hardware Commissioning Tests

For the validation of the circuit model explained in chapter 5.1, two sources of validation data are used. The first category of validation data is coming from the "Hardware Commissioning Tests". These test are performed periodically to guarantee the functionality of the LHC machine. For the main quadrupole circuit, these tests were done the last time in march 2018. The current profiles of the hardware commissioning tests for this circuit are shown in figure 5.8.

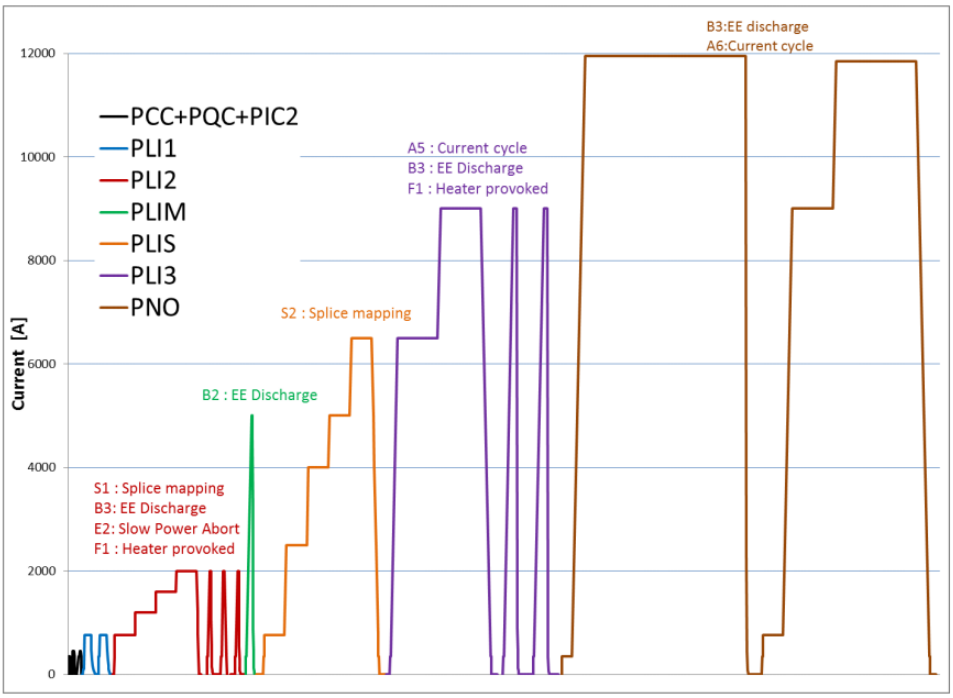

Figure 5.8: Hardware Commissioning test categories [57]

To validate the circuit model for different current levels, the following test categories were chosen:

- **PLI2-B3**: fast power abort with energy-extraction at a current level of $I_{\text{test},1} = 2$ kA
- **PLIM-B2**: fast power abort with energy-extraction at a current level of $I_{\text{test},2} = 5$ kA
- **PNO-B3**: fast power abort with energy-extraction at a current level of $I_{\text{test},3} = 10.35$ kA

All mentioned tests are fast power abort tests with enabling the energy-extraction system. Within every test, first the current will be increased until $I = 350$ A. At $I = 350$ A the power converter controller can be turned on and then the current increases until the testing current level with a ramp rate of $\mathrm{d}I/\mathrm{d}t = 10$ A/s. After the test current level is reached and a certain delay, the switches of the power converter rack within the power converter will open. This is called a fast power abort. After a delay of $\Delta t_{\text{EE,trigger}} = 96$ ms the energy-extraction system is triggered and the energy-extraction switches will open with a delay $\Delta t_{\text{EE,open}} = 6$ ms. The energy-extraction switches are mechanical switches and a slightly variation in opening time of a couple of milliseconds is possible. For the first comparison between test data and simulation results the test PNO-B3 is chosen. The current level within this test is closer to the nominal current and is thus more representative. Table 5.2 summarizes the different test procedures within the hardware commissioning test campaign for the LHC main quadrupole circuit.

The current is measured with an acquisition frequency of $f_{\text{A,signal}} = 1$ kHz at two redundant boards in parallel, board A and board B [52]. The measured current signals are

Table 5.2: Test procedures of the hardware commissioning test campaign for the LHC main quadrupole magnets (1/2)[57]

Name	**Test current level**	**Description**	**Test with EE system**	**Test with QH**
PCC.2 + PQC + PIC2	450 A	Checking the free-wheel diodes (see chapter 2.1.1) and initial calibration of the quench protection system (QPS)	No	No
PLI1.B3	760 A	A quench is simulated from one current lead. This provokes a discharge of energy using the energy-extraction (EE) system. Checking the free-wheel diodes	Yes	No
PLI1.D2	760 A	A powering failure is simulated. Correct function of the power converter has to be verified during a powering failure	No	No
PLI2.S1	2000 A	Ramping the circuit current until the test current level with three plateaus at intermediate levels. Checking the status of the splices and the QPS compensation parameters	No	No
PLI2.B3	2000 A	Checking the performance of the QPS and EE system. Checking the correct current sharing in the different free-wheel diodes	Yes	No
PLI2.E2	2000 A	A slow power abort (SPA) will be provoked. Checking the functionality of the power converter in case of an SPA	No	No

Table 5.3: Test procedures of the hardware commissioning test campaign for the LHC main quadrupole magnets (2/2) [57]

Name	**Test current level**	**Description**	**Test with EE system**	**Test with QH**
PLI2.F1	2000 A	Checking the correct functionality of each equipment in the case of a quench at low current in a magnet	Yes	Yes
PLIM.B3	5000 A	Checking the correct functionality of the energy-extraction system	Yes	No
PLIS.S2	6500 A	Checking the status of the splices while ramping the circuit up and down	No	No
PLI3.A5	9000 A	Checking the correct performance of the current leads	No	No
PLI3.B3	9000 A	Checking the correct performance of the QPS and the EE system. Checking the correct current sharing in the different free-wheel diodes	Yes	No
PLI3.F1	9000 A	Checking the correct functionality of the power converter and the QPS in case of a quench	No	Yes
PNO.B3	RQF: 10450 A, RQD: 10200 A	Nominal current and an additional current margin are applied and the correct performance of each equipment has to be checked during a provoked energy-extraction event	Yes	No
PNO.A6	RQF: 10450 A, RQD: 10200 A	Checking the performance of the current leads and the stability of the circuit at nominal current	Yes	No

I_A and I_B, respectively. Within this thesis the current signal coming from board A (I_A) is used. Another current signal used for the validation is I_{Meas}. This current is the filtered signal of I_A with a $f_{Meas,signal} = 50$ Hz. The need to use both signals for the validation is due to the different time period for which the signal data is saved. The data of I_A is saved only for a time period of $\Delta t_{A,acq.} \approx 8$ s. In contrast, data of I_{Meas} is saved for the complete test period. Thus, the current signal I_A is needed to validate especially the part during the FPA and the enabling of the energy extraction system and the current signal I_{Meas} to validate the course of the current during the discharge. Another important signals for the validation are the measured circuit voltage U_{Meas}, the voltage across the energy-extraction resistor U_{EE} and the current to ground I_{EC}. Table 5.4 summarizes the signals used for the validation of the main quadrupole circuit model within this thesis.

Table 5.4: Circuit signals from the Post Mortem Database

Signal name	**Description**	**Acquisition frequency**	**Representative time period**	**Signal name within PM Browser**
I_{Meas}	Circuit current	50 Hz	$0 \leq$ t $\leq t_{test}$	I_Meas
I_A	Circuit current (see DCCT-point in figure 5.4)	1000 Hz	t_{FPA}-$t_{offset} \leq$ t $\leq$ t_{EE}+$t_{offset,1}$	I_A
U_{Meas}	Voltage across the power converter output nodes	50 Hz	$0 \leq$ t $\leq t_{test}$	V_Meas
$U_{EE,Meas}$	Voltage across the energy-extraction resistor	50 Hz	t_{FPA}-$t_{offset} \leq$ t $\leq$ t_{EE}+$t_{offset,1}$	U_Dump_Res
$I_{EC,Meas}$	Current to ground within the grounding system	50 Hz	t_{FPA}-$t_{offset} \leq$ t $\leq$ t_{EE}+$t_{offset,1}$	I_Earth

The following table shows an overview of the tests mentioned in the document for the "Hardware Commissioning Tests" for the LHC main quadrupole magnets. The specific tests used for the validation within this thesis are marked in red. This table corresponds to figure 5.8. The signals for all tests are stored in the so-called Post Mortem Database and are opened and extracted using the Post Mortem Browser (PM Browser). The file names used within this thesis are referring to the Post Mortem Browser time stamp of these files. The tests chosen for the validation are stored in the PM Browser under the following time stamp.

- **PLI2.B3**: 20180312-215849.840_RPHE.UA47.RQD.A45 ($I_{test,1} = 2$ kA)
- **PLIM.B3**: 20180313-171137.680_RPHE.UA47.RQD.A45 ($I_{test,2} = 5$ kA)
- **PNO.B3**: 20180314-223015.160_RPHE.UA47.RQD.A45 ($I_{test,3} = 10.35$ kA)

The file name contains the date and the time stemp of the event, the sector within the LHC and the circuit type. In this particular case, it is the de-focussing (RQD) circuit within the arc sector 4-5 (A45). The first signal to validate is the circuit current. Figure 5.9 shows the comparison between simulated an measured current over time for all three chosen tests mentioned above in the main quadrupole de-focussing circuit from sector A45.

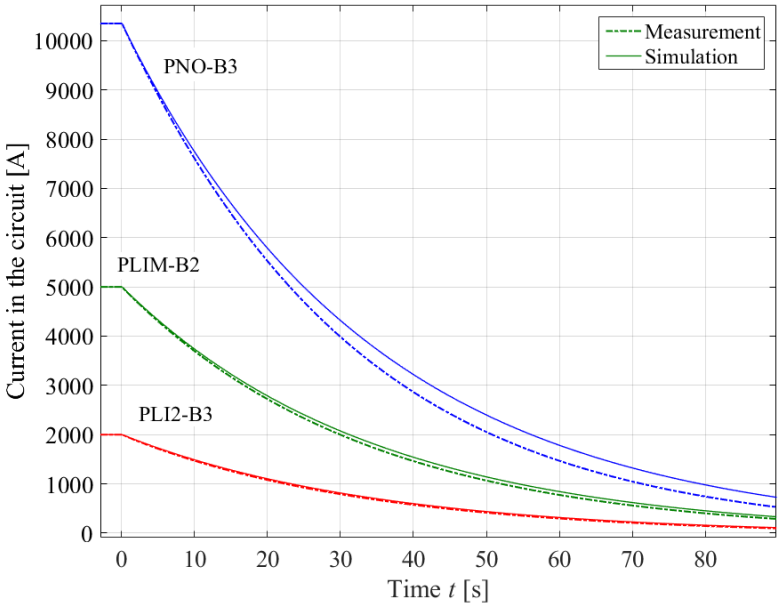

Figure 5.9: Test current levels for PNO-B3, PLIM-B2 and PLI2-B3 of the circuit RQD.A45. Comparison between simulated and measured results. Simulated using PSpice©.

Figure 5.9 shows the part shortly before the FPA and the complete discharge. It can be noticed, that the simulated and measured currents are in good agreement for all three tests. The difference according to test PNO-B3 can be explained with temperature change of the energy-extraction resistor. In fact, this resistor carries the complete circuit current after the energy-extraction activation. When the current is passing through the resistor, its starts slightly heating up the resistor body. The most of the heating power is extracted by the water (see figure 2.10), but since the heat transfer is not ideal the resistor plates start heating up and its resistance value starts increasing. Due to the higher resistance value, the current starts decreasing faster, with respect to the simulations in which the initially set resistance value remains unchanged. These effect can only be noticed at high currents, at which the deposited power ($\sim I^2$) is high enough.

Due to the time window of the data acquisition, the complete ramp cycle up to the test current level is visible only for the test PLI2-B3. The most representing test is the one at the current level of $I_{\text{test},3} = 10.35$ kA, because this test was performed at the current closest to the nominal current [9]. Figure 5.10 shows the current plot over time within the time window -25 ms $\leq$ t $\leq$ 125 ms, to show better the moment of the FPA and the moment, when the energy-extraction is turned on. The moment of triggering the energy-extraction has an estimated delay of $\Delta t_{\text{EE,trigger}} = 96$ ms with respect to the FPA. The switches of the

energy-extraction system open completely $\Delta t_{\mathrm{EE,open}} \approx 6$ ms after triggering. Adding the delay of the energy-extraction triggering time and the time to open the energy-extraction switches to the initial time of the fast power abort, the current starts discharging faster due to the energy-extraction at the absolute time of $t_{\mathrm{EE}} = 82$ ms.

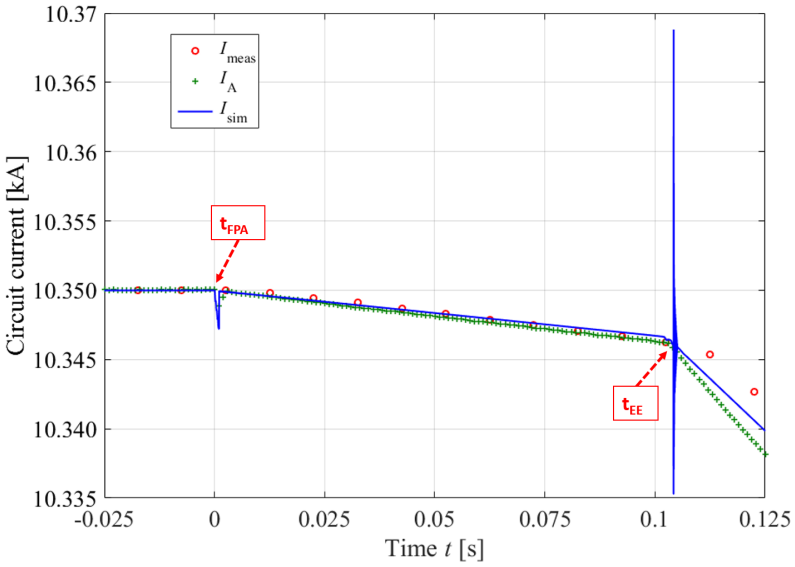

Figure 5.10: Current behaviour at the FPA time for the test PNO-B3. Comparison between measurement and simulation. Simulated using PSpice©.

Considering the curve of I_{A}, the peak value at $t_{\mathrm{FPA}} = 0$ ms indicates the exact time, when the FPA was triggered. After this time, the current starts decreasing. As explained in chapter 2.1.1, an additional energy-extraction (EE) system is installed, which forces the current to decrease faster and as result, takes out the energy of the circuit and protect the circuit components. Both important effects, the FPA and the triggering of the energy-extraction system, are visible within figure 5.10. It can be noticed that the discharge happens with two times constants. As explained in chapter 2.1.3, the energy extraction system is used to reduce the time constant of the discharge and as a result extract the stored energy of the circuit faster. The FPA occurs at $t_{\mathrm{FPA}} = 0$ ms. At this moment, the power rack connection opens and the currents starts discharging. Within the signal I_{A}, a clear indentation is visible which marks the start of the discharge. After the FPA is triggered the time constant for this discharge can be estimated. As mentioned in chapter 2, the magnet inductance is given with $L_{\mathrm{m}} = 5.6$ mH. The number of magnets within this circuit is $N_{\mathrm{m}} = 47$. With the warm part of the circuit resistance ($R_{\mathrm{warm}} = 0.6644$ mΩ) and the value of energy-extraction resistance ($R_{\mathrm{EE}} = 6.85$ mΩ) used for the LHC main quadrupole circuit, the time constant of the discharge before the FPA can be calculated with $\tau_{\mathrm{FPA}} = L_{\mathrm{m}} \cdot N_{\mathrm{m}} / R_{\mathrm{warm}} = 396.144$ s. From here it can be clearly noticed that the discharge without the energy extraction would take more than 6 minutes which would increase the risk of overheating the magnet coils. The energy-extraction system is activated at $t_{\mathrm{EE}} = 96$ ms + 6 ms = 102 ms. After this moment, an increased time-derivative of the current is visible

in figure 5.10. With the activation of the energy-extraction system the time constant of the discharge is reduced and can be estimated to $\tau_{EE} = L_m \cdot N_m / (R_{warm} + R_{EE}) = 35.02$ s. Instead of extracting the stored circuit energy (47·395 kJ= 18.56 MJ) within minutes, using the energy-extraction system reduces the this time to almost 30 s. This underlines the importance of the energy-extraction system for the complete magnetic circuit.

Comparing the measured and the simulated signals, in particular at the enlarged fraction of the plot at t_{FPA}, it becomes clear that such a drop is also visible within the signal I_A. The frequency of the oscillations after the indentation is $f_{signal,sim.} \approx 4.4$ kHz. Compared to the acquisition frequency of the signal coming from board A is $f_{A,signal} = 1$ kHz the complete signal can not be represented during the measurement. An explanation for this could be the acquisition frequency of the signal I_A. Due to limitations of every measurement equipment, also the acquisition frequency of board A and board B is not high enough to completely represent the behaviour of the current at t_{FPA}, when the fast power abort occurs. But among this fact, the simulated current and the measured current I_A are in very good agreement. It is very interesting to see the, where the these oscillations are coming from. Therefore, figure 5.11 and 5.12 can be considered. Figure 5.11 a shows a more detailed view on the oscillations during the FPA and figure 5.11 b shows the sum of the currents from all parallel capacitors located in the main output filter and the filter of the sub sub module within the power converter. The oscillations during the activation of the energy-extraction system are shown more in detail in figure 5.12 a and figure 5.12 b. The reason for the oscillations during the energy-extraction activation can be observed, considering the capacitors to ground located in the power converter [28, 32].

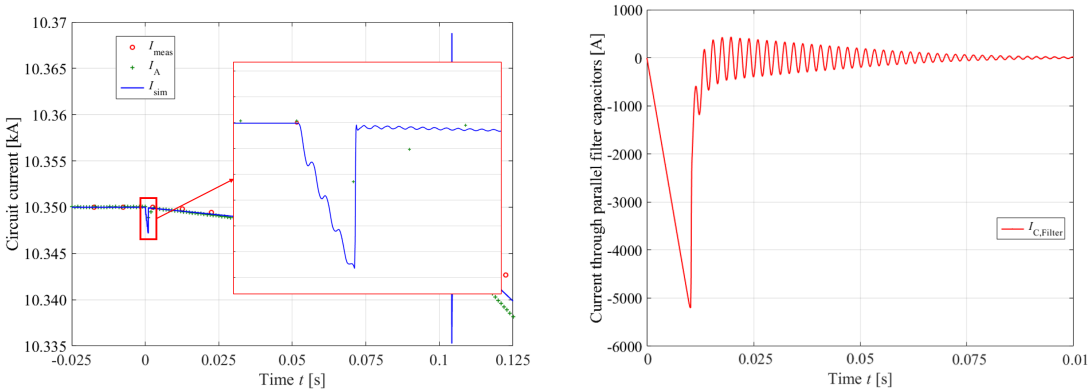

(a) Zooming section on the oscillations during the FPA

(b) Current sum through all parallel capacitors within the main filter and the sub sub filter

Figure 5.11: PSpice© simulated and measured circuit current. (a) Zooming section on the oscillations during the FPA. (b) Current sum through all parallel capacitors in the main output filter an the sub sub filter

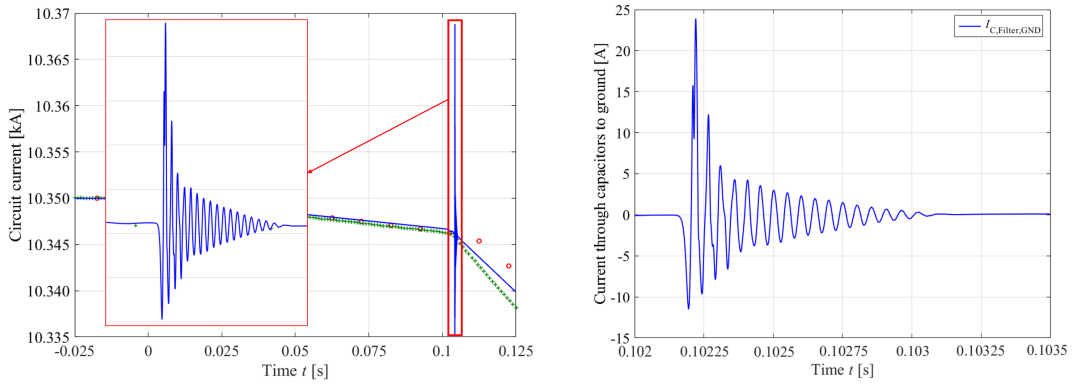

(a) Zooming section on the oscillations during the EE activation

(b) Current sum through all capacitors to ground within the model

Figure 5.12: PSpice© simulated and measured circuit current. (a) Zooming section on the oscillations during the EE activation. (b) Current sum through all capacitors to ground within the model

Figure 5.11 b shows that the current through the capacitors is most of the time 0, except the one at the time of the fast power abort at $t_{\mathrm{FPA}} = 0$ ms. These capacitors are located in parallel to the output nodes of the power converter. In the moment of the FPA, a large voltage change in the order of $dV/dt \approx 14.8$ kV/s introduces a high current through the capacitors that can be estimated by using the total capacitance value of the parallel capacitors (0.364 F). Using $I_{\mathrm{c}} = \Sigma C_{\mathrm{parallel}} \cdot dV/dt$ a current value of $I_{\mathrm{c}} \approx$ 5387 A can be estimated, which corresponds to the peak value in figure 5.11 b. During the energy-extraction activation the main switches of the energy extraction resistor open. This effect introduces an oscillation in main signal, which is coupled to a current through the capacitors to ground. The sum of the capacitor currents to ground is shown in 5.12 b.

The next important signal for the validation is the voltage of the circuit. The most interesting voltage signal is the one from the test PLI2-B3 (2 kA test), because two separate current ramp-ups and plateaux are present. For that reason the circuit voltage of the PLI2-B3 test is shown in figure 5.13. Before the fast power abort, the voltage depends only on the resistance coming from the leads within the circuit (R_{warm}) and the current level I, U_{PC} = $R_{\mathrm{warm}} \cdot$ I . During the fast power abort and the energy-extraction opening, the circuit voltage drops. The simulated voltage is in good agreement with the measured voltage and corresponds to the ramp periods of the current from figure **??**. But a discrepancy between the curves is visible between t = -700 s and t = -600 s, when the current is ramped up from 1500 A up to 2000 A with a ramp rate of about 11 A/s. Due to this ramp rate, a inductive voltage develops with $U_{\mathrm{ind}} = L_{\mathrm{m}} \cdot dI/dt$. The total voltage across the power converter can be easily calculated using Kirchhoff's second law, $U_{\mathrm{PC}} = R_{\mathrm{warm}} \cdot I + U_{\mathrm{ind}}$. Due to saturation effects from previous magnetization cycles, the inductive voltage U_{ind} is not present so strong within the measured voltage with respect to the simulated one. Figure 5.14 shows the time window when this transient occurs.

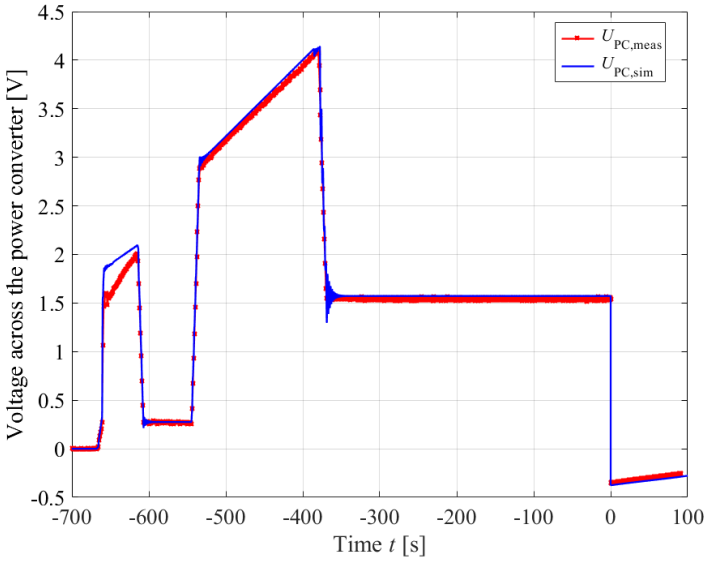

Figure 5.13: Circuit voltage behaviour for the test PLI2-B3. Comparison between measurement and simulation. Simulated with PSpice©.

In figure 5.14 it is visible that the simulated voltage is about 20 % larger than the measured voltage. The reason is the magnetization in the superconductor, which appears during the first rampup after a magnetic cycle of the superconducting magnets. This hysteretic effect has an influence on the differential inductance. A differential inductance reduction of similar amplitude was observed in the LHC main dipole magnets, which are made of a similar superconductor and operate at about the same magnetic field [50]. Another signal in the validation process is the voltage across the energy-extraction resistor U_{EE}. In figure 5.15 these voltages for all mentioned tests are shown.

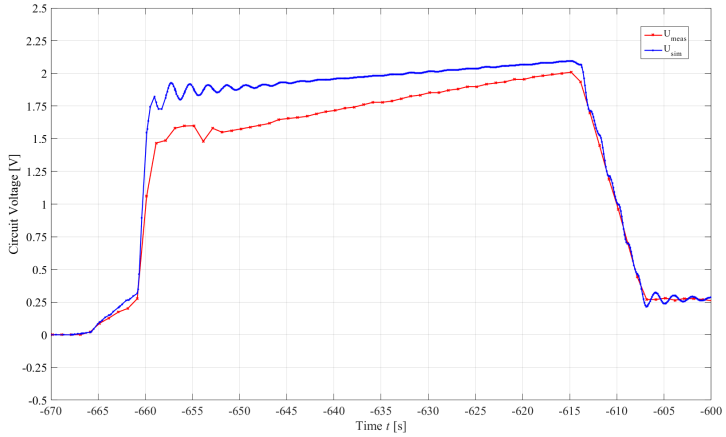

Figure 5.14: Circuit voltage behaviour for the test PLI2-B3. Zoomed section during the first ramp-up of the current. Comparison between measurement and simulation. Simulated with PSpice©.

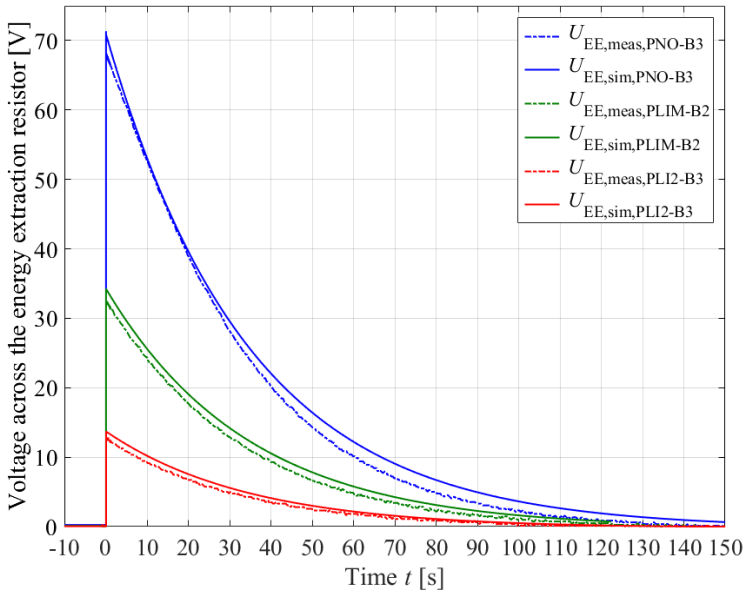

Figure 5.15: Voltage across R_{EE} for all tests. Comparison between measurement and simulation. Simulated with PSpice©.

The voltage U_{EE} starts increasing, when the current starts passing through the EE resistor. It has to be noticed that the variable of R_{EE} can change during the discharge, because the stainless steel plates within the resistor body can heat up and as a result increase the resistance value. The voltage across the energy extraction resistor can be easily estimated with $U_{\mathrm{EE}} = I \cdot R_{\mathrm{EE}}$. For example, the current in the moment of the energy-extraction activation is $I = 10346$ A. With the energy-extraction resistor of $R_{\mathrm{EE}} = 6.85$ mΩ, the voltage corresponds to $U_{\mathrm{EE}} = 70.87$ V. This peak value can be noticed, looking at the peak value of $U_{\mathrm{EE,sim,PNO\text{-}B3}}$. Thus, the curves in figure 5.15 shows that the voltages across the energy-extraction resistor from the simulations and from the test data are in good agreement.

The next signal used for the validation within the list of signals taken out from the hardware commissioning tests, is the current to ground I_{EC}. Figure 5.16 shows the plot of the current to ground I_{EC} versus time for the test PNO-B3 (10.35 kA) from the measurement and the simulation data. Two events are visible in I_{EC} signals within figure 5.16. The first peak is due to the FPA and the negative, second peak is due to the opening of the energy-extraction switches. From the plot it can be also noticed that the simulated current to ground reaches a peak of 37.5 mA at the moment of the FPA. According to the measurement data, the maximum current to ground is 25 mA. This difference can be relied as well to the fact that the measurement signals are depending on a finite acquisition frequency. Thus, some part of the behaviour is maybe not represented within the measurement data and the peak of 25 mA within the measurement signal could be higher in reality, but was not measured during the test due to the acquisition frequency.

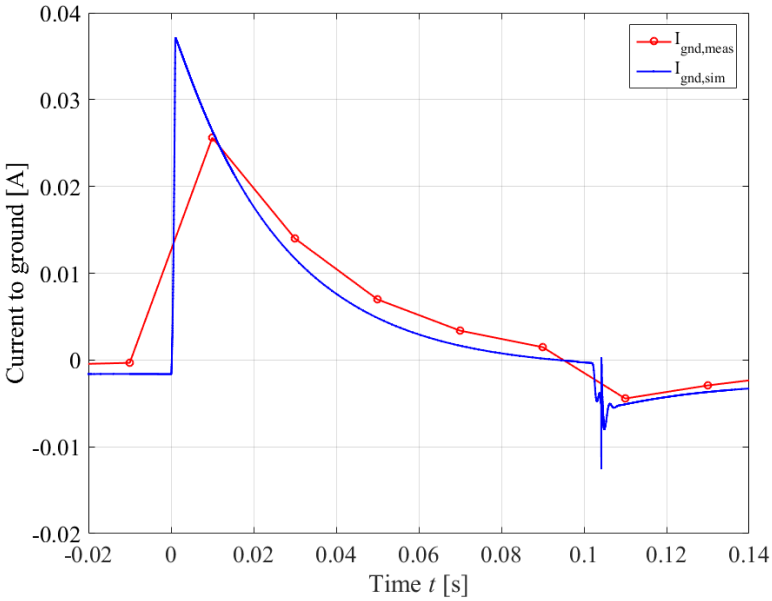

Figure 5.16: Current to ground for the test PNO-B3. Comparison between measurement and simulation

5.2.2 Short summary of the validation process for the circuit model

After the validation of the PSpice© circuit model, it can be concluded that the model is in good agreement with the tests performed at different current levels after triggering the energy-extraction system. Due to magnetization effects in the magnet superconductor, the simulated circuit voltage shows at low currents a $\approx$ 20 % higher voltage than the measured value [50]. In some cases, validating simulation results against measurements with relatively low acquisition frequency proved challenging. In particular, the high-frequency oscillations during the opening phase of switches could probably not completely be measured due to the low acquisition frequency. The circuit model can be called finally validated and it can be used for the co-simulation of magnet and circuit model (see chapter 6).

Chapter 6

Co-simulation of the LHC main quadrupole circuit

This chapter describes the co-simulation studies of the LHC main quadrupole magnet and its circuit and their validation against experimental results. After finishing the validation process the transient during the discharge will be studied further in detail together with simulating the two failure cases in which the quench heaters are completely and partially not triggered during the transient.

6.1 Simulation setup for the co-simulation

Before the validation results can be observed, the circuit model used within the simulation and the co-simulation settings have to be discussed. This provides understanding for the events in the circuit when one magnet within the magnet chain quenches. Figure 6.1 shows the quenched magnet within the LHC main quadrupole circuit. As explained above, the magnet chain of the LHC main quadrupole circuits can contain from 47 up to 51 magnets [9]. In this case the circuit contains 47 magnets. Every magnet has a parallel resistor and a protection by-pass diode. Moreover, every magnet is protected as well by quench heaters, which trigger in case of a detected quench and transfer parts of the coil to normal state and reducing in that sense the temperature of the hot-spot. For providing consistency to the later discussed validation data, magnet Nr. 14 is the one that quenches and develops a resistance. This resistance is embedded in the circuit model coming from the field model of STEAM-LEDET [6, 58] together with inductive voltage across the magnet. As explained in chapter 2.2.1, both apertures of the main quadrupole magnets are powered in two separate circuits. Figure 6.1 refers to the de-focussing circuit within sector 4-5 of the LHC (see figure 1.1).

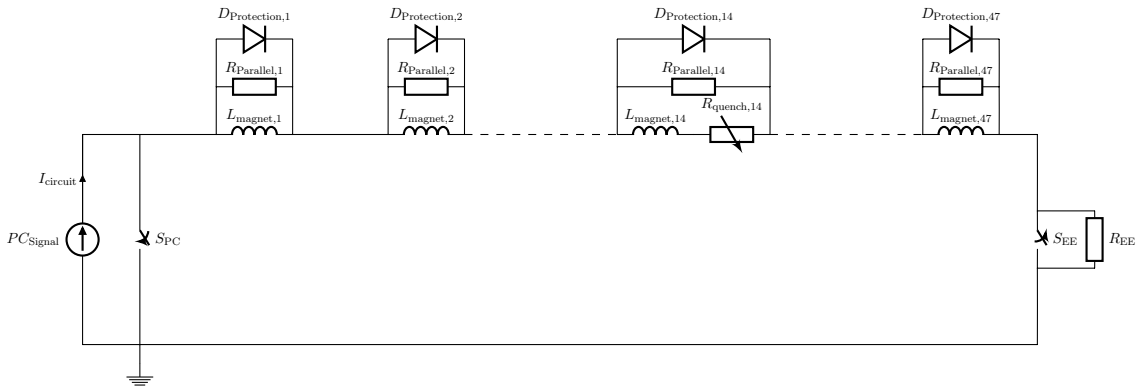

Figure 6.1: Circuit model with quenched magnet used for the co-simulation. Quenched magnet is Nr. 14.

As explained in chapter 3.6 COSIM is a program developed at CERN which allows coupling two or more physical models using a specific algorithm and tool adapters [1, 2]. The tool adapters are interfaces, which allow to control the used tools and perform certain tasks according to the model. Examples of these tasks include settings of the input-file, to run a dedicated study and to retrieve the output. The tool adapters have to contain ports for exchange coupling parameters and an Application Programming Interface (API). Within this thesis the coupled tools were PSpice© for the circuit modelling and STEAM-LEDET for the field modelling.

The magnet (field) model used for the co-simulation was already discussed and validated in chapter 4 an the circuit model used for the co-simulation is the one already validated in chapter 5. Both models were coupled by using the waveform relaxation method (see chapter 3). In addition, a so-called pre-conditioner is used within the circuit model. A pre-conditioner in terms of co-simulation is a lumped element within the circuit model that represents the 2D field model and provides the first order approximation of the field model to the circuit model [2]. In this case a 2D magneto-thermal field model of a quenched main quadrupole magnet will be represented as a lumped element of the LHC main quadrupole circuit model. Figure 6.2 shows the pre-conditioner used for co-simulation.

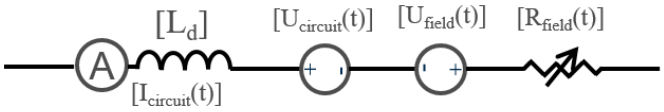

Figure 6.2: Pre-conditioner for the co-simulation. First-order approximation of the 2D field model in the circuit model [2, 47].

The pre-conditioner contains the coupling parameters of both models (see figure 6.2). These coupling parameters are in this case a circuit current I_{circuit}, previously calculated by the circuit model, an inductive voltage U_{field} calculated by the field model and a component for modeling analog behaviour (ABM), which contains the voltage and current characteristic V = f(I(t)) of a resistance R_{field} which represents the resistance of the quenched magnet.

The co-simulation is subdivided into several time-windows as explained in chapter 3.6 [2, 47]. In a configuration file the settings in terms of time-step and size of the time-windows can be specified. Figure 6.3 shows the setting used for the co-simulation performed within this thesis. The configuration file contains the paths for both programs that need to be coupled, as well as the names of the model solvers and the individual configuration of the field and the circuit model. The size of the time-window to solve is defined between t_0 and t_{end}. Moreover, the maximum step-size and the relative and absolute tolerance can be specified.

```
"coSimulationDir": "C:\\COSIM\\MQ_LEDET_PSpice\\Output\\2\\",
"coSimulationModelDirs" : ["C:\\COSIM\\MQ_LEDET_PSpice\\Input\\20181208-143232.340_RPHE.UA47.RQD.A45_test\\PSpice\\",
                           "C:\\COSIM\\MQ_LEDET_PSpice\\Input\\20181208-143232.340_RPHE.UA47.RQD.A45_test\\LEDET\\"],
"coSimulationModelConfigs": ["PSpiceConfig.json",
                             "LedetConfig.json"],
"coSimulationModelSolvers": [PSPICE,
                             LEDET],
"coSimulationPortDefinitions": ["PSpiceInputOutputPortDefinition.json",
                                "LedetInputOutputPortDefinition.json"],
"convergenceVariables": ["I(xmagnet.L_diff_1)",
                         null],
"t_0":   [0.00, 1.90, 2.20, 2.40, 2.70, 3.20, 3.80],
"t_end": [1.90, 2.20, 2.40, 2.70, 3.20, 3.80, 4.30],
"t_step_max": [[1e-3, 1e-4, 1e-4, 1e-4, 1e-3, 1e-3, 1e-3],
               [1e-3, 1e-4, 1e-4, 1e-4, 1e-4, 1e-4, 1e-4]],
"relTolerance": [1e-3,
                 null],
"absTolerance": [10,
                 null],
"executionOrder": [1,
                   2],
"executeCleanRun": [true,
                    true]
```

Figure 6.3: Settings used in this thesis for running co-simulations between the STEAM-LEDET field model and the PSpice© circuit model.

Since now both models are combined in a co-simulation, the effect of a quenched magnet on the complete main quadrupole circuit has to be discussed further in detail. The sequence of events during a quench is summarized by following points:

1. The circuit is in normal operation mode or in a current ramp-up mode.
2. A quench occurs in one of the magnets (in this case: magnet number 14, external aperture of the cold mass 30L5). The part of the superconductor that initially quenched is the hot-spot.
3. The coil resistance starts developing and growing.
4. The developing resistance multiplied by the current flowing through the magnet gives a voltage drop across the magnet.
5. The voltage drop reaches the quench protection threshold of $U_{\text{QP,thr.}} = 100$ mV.
6. Fast power abort is triggered and quench heaters are activated.
7. The coils of both apertures heat up due to thermal diffusion from the quench heater strips.
8. Parts of the coils of both apertures are transferred to the normal conducting state and the resistance starts developing more quickly.

9. Voltage drop reaches cold by-pass diode opening voltage, which in operating conditions at a temperature of 1.9 K corresponds to $U_{\mathrm{D,open,1.9K}} \approx 6$ V [41].
10. Diode opens and the current starts by-passing the quenched magnet.
11. Coil hot-spot temperature is kept to an acceptable value.
12. Energy-extraction system is triggered $t_{\mathrm{EE,trigger}} \approx 96$ ms after the FPA.
13. Energy within the circuit is transferred to the energy-extraction resistor.
14. Cryogenic diode temperature is kept to an acceptable value.

6.2 Validation of the co-simulation model

The validation of the co-simulated behaviour is important, because it represents the complete behaviour of the main quadrupole circuit during a quench of a specific magnet within this circuit. During a special campaign for the LHC main quadrupole circuits, one of the magnets quenched during the current ramp of the magnets. After having the model validated, unexpected events occurring in the circuit can be reproduced, and failure cases can be investigated. For example, a quench heater failure can be simulated, when the quench heaters power supplies are only partially triggered or not triggered at all or triggered with a time delay. To validate the co-simulation model composed of a PSpice© electrical circuit model coupled with a STEAM-LEDET electro-thermal magnet model, data from a natural quench occurred in the in the LHC main quadrupole circuit was used. The validation data is coming from the Post Mortem Browser and the test data has the following time-stamp:

- 20181208-143232.340_RPHE.UA47.RQD.A45

The first validation signal is the circuit current. Figure 6.4 shows the circuit current during the ramp up and after the fast power abort with energy-extraction. The left-hand figure shows the complete ramp up and the discharge. The right-hand figure shows a more detailed overview of the effects during the fast power abort and the opening phase of the energy-extraction switch. The FPA occurs at $t_{\mathrm{FPA}} = 0$ s and the activation of the energy-extraction system at $t_{\mathrm{EE}} = 102$ ms. As explained during the validation of the circuit model in chapter 5, high-frequent oscillations after the power supply switching off and after the activation of the energy-extraction system can be observed. These oscillations are dependent on parallel capacitors in the filters of the sub-components of the power supply as well as the capacitors to ground within the power converter and the magnet models. The current I_{A} is the measured signal with the acquisition frequency of 1 kHz and I_{meas} is the filtered signal of I_{A} with an acquisition frequency of 100 Hz. The simulated current signal and the measured signal are in good agreement. Figure 6.4 b proofs that also detailed events can be reproduced with both models during a co-simulation.

Another interesting signal to observe is the voltage of the quenched magnet. Figure 6.5 shows the voltage growth during the simulation and coming from the measurement which

are in good agreement. The initial resistance growth is coming from the hot-spot. This part of the magnet was the one that quenched initially at t_{quench} = -38 ms. The resistance develops with a certain quench propagation velocity and the visible drop at t_{FPA} = 0 ms is due to the fast power abort. Shortly before the fast power abort, the quench heaters were triggered at $t_{\text{QH, trigger}}$ = -3 ms. The heaters starts heating up parts of the coil and the voltage increases stronger.

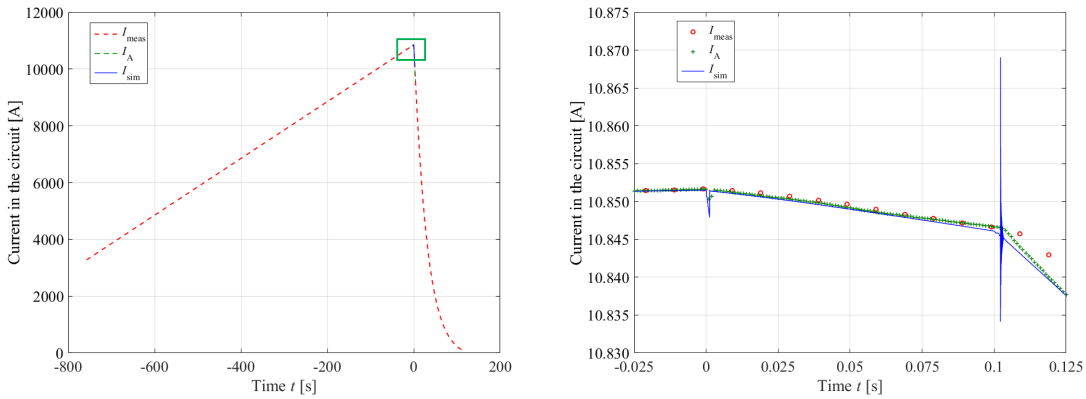

(a) Circuit current for the quench event. Comparison between measurement and simulation.

(b) Circuit current for the quench event. Detailed view of the FPA and the EE-activation. Comparison between measurement and simulation.

Figure 6.4: General (a) and detailed (b) comparison of simulated and measured circuit current. Simulated with COSIM (STEAM-LEDET and PSpice©).

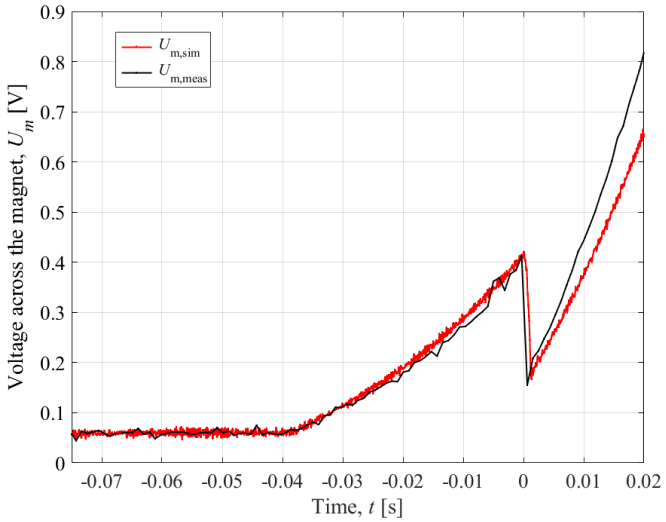

Figure 6.5: Comparison of simulated and measured voltage across the magnet. Extracted from the voltage across the diode before the diode becomes conductive. Simulated with COSIM (STEAM-LEDET and PSpice©).

6.2.1 Cryogenic diode modelling

Within this thesis a new diode model for the protection diodes was developed. Now within the diode model the diode heating effect is taken into account. As explained in chapter 2.2.2.2, the protection diodes are located within the cold masses at the operating temperature of $T_{\mathrm{op}} = 1.9$ K. When the diode opening voltage is reached, the current starts passing through the diode and heating up the diode. Due to the heating up, the diode characteristics start changing. This is qualitatively shown in figure 2.19. With increasing temperature the opening voltage of the diode decreases. At room temperature the diode opens at 0.7 V. For that reason, the assumptions and limitations has to be discussed more in detail. The forward characteristics of the diode model can be described using equation 6.1 [59].

$$I_{\mathrm{D}} = I_{\mathrm{s}} \left(exp \left(\frac{U_{\mathrm{D}}}{N \cdot U_{\mathrm{t}}} \right) - 1 \right) \tag{6.1}$$

Here I_{s} [A] is the reverse bias saturation current, U_{D} [V] is the voltage across the diode, U_{T} [V] is the thermal voltage, and N [-] is the emission coefficient. In PSpice© diode models are already embedded and the characteristic parameters within the diode models can be changed to reproduce a specific diode behavior. However, these models are static and can not change during the simulation time. The goal of developing a new diode model is to adapt the diode characteristics depending on the energy deposited in the diode during the discharge. This represents a rough approximation, since in reality the diode energy E_{D} and the diode temperature T_{D} are non-linearly coupled, as well as the temperature T_{D} and the diode opening voltage U_{D}. Within the new diode model, the emission coefficient was set to change during the transient. The emission coefficient N has to change between 6 and 1.2, which correspond to the opening voltage of the diode at 1.9 K and room temperature respectively. When the voltage across the diode starts growing, the current-voltage behaviour of the diode is calculated according to equation 6.1. From the voltage across the diode and the current passing through the diode, the disappearing power $P_{\mathrm{D}} = U_{\mathrm{D}} \cdot I_{\mathrm{D}}$ and the energy $E_{\mathrm{D}} = \int_{t_{quench}}^{\infty} P_D \, dt$ will be calculated. Then the simplified assumption was used that the emission coefficient changes linearly with the energy deposited within the diode. Equation 6.2 describes the change of the emission coefficient linearly with the deposited energy.

$$N = N_1 - (N_1 - N_2) \cdot f_{\mathrm{E}} \cdot E_{\mathrm{D}} \tag{6.2}$$

Here the factors $N_1 = 6$ and $N_2 = 1.2$ are introduced. The factor f_{E} is used as a fitting parameter and is multiplied with the previously calculated energy deposit within the diode.

As a last step the calculated parameter N_{new} has to replace the emission coefficient within equation 6.1. This happens during every time-step within the simulation and represents the diode behaviour more accurately than the static diode model. Within PSpice© the values calculated with equation 6.2 is limited to remain between 6 and 1.2.

After the model was developed and independently tested, it was embedded within the model of the quenched magnet and used for the co-simulation. Figure 6.6 shows the measured voltage across the diode during the detected quench used for the validation together with the simulated voltage across the static diode model and the voltage across the new diode model. The netlist of the diode model within PSpice© is located in the Annex of this thesis.

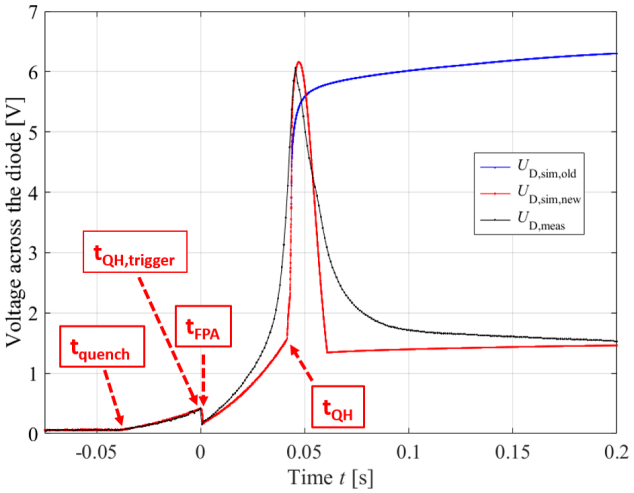

Figure 6.6: Voltage across the protection diode. Comparison between measurement and simulation. Simulated with COSIM (STEAM-LEDET and PSpice©).

The new diode model represents more accurately the real behaviour of the protection diode, because the static diode model behaviour does not change with the diode thermal condition. This can be noticed, looking at the signals after $t_{\text{sim}} = 50$ ms. Within figure 6.6, three distinct phases can be observed, and are discussed more in detail. First, between $t_{\text{quench}} =$ - 38 ms and $t_{\text{sim}} = 0$ s. Before $t_{\text{sim}} = 0$ s, the voltage growth across the diode depends only on the resistance growth of the hot-spot. These signals show that the measured and simulated voltages are in good agreement. Thus, the initial hotspot development model and the set quenching time for the hot-spot currently reproduce this transient.

The second phase is characterized by the forced FPA and the quench heater triggering (between $t_{\text{FPA}} = 0$ s and $t_{\text{QH}} = 50$ ms). A discrepancy between the simulated and the measured voltage signals can be noticed. One reason for this difference could be the assumptions within the temperature modeling between the quench heaters and the outer layer of the cable coil. The heat propagates from the quench heaters through the coil insulation of the quench heaters and the insulation layer of the outer cable coil. When the heat arrives at the cable half-turns, the resistance and with the resistance also the voltage grows instantaneously. Another reason could be the simplified formula for the quench

propagation velocity, which determines the resistance and voltage growth. A third reason could be the modeled diode characteristic. Within the last phase as well a difference can be noticed between the new diode model and the real diode behaviour. The reason therefor is the rough approximation in terms of correlation between energy and temperature. At low temperatures the required energy to be deposited within the magnet to change the diode behaviour is much smaller, compared to the required energy at higher temperatures. Thus, the link between the temperature and the diode opening voltage is more sensitive. Therefore, the almost instantaneous change within the diode model between $t_{\mathrm{QH}} = 50$ ms and $t_{\mathrm{sim}} = 50$ ms is in good agreement with the measured voltage, but between $t_{\mathrm{sim}} = 50$ ms and $t_{\mathrm{sim}} = 100$ ms where the required energy is not so large anymore, the almost instantaneous drop within the diode model behaviour does not represent ideally the real diode behaviour. However, using the model developed within this thesis, the diode behaviour during a real quench can be reproduced more accurately.

6.3 Analysis of transient effects during the simulation

After the co-simulated model and the developed diode model can be called validated, a more detailed analysis of the simulation signals will be performed within the following sections. The first interesting signal to discuss is the coil resistance R_{Coil} (see figure 6.7).

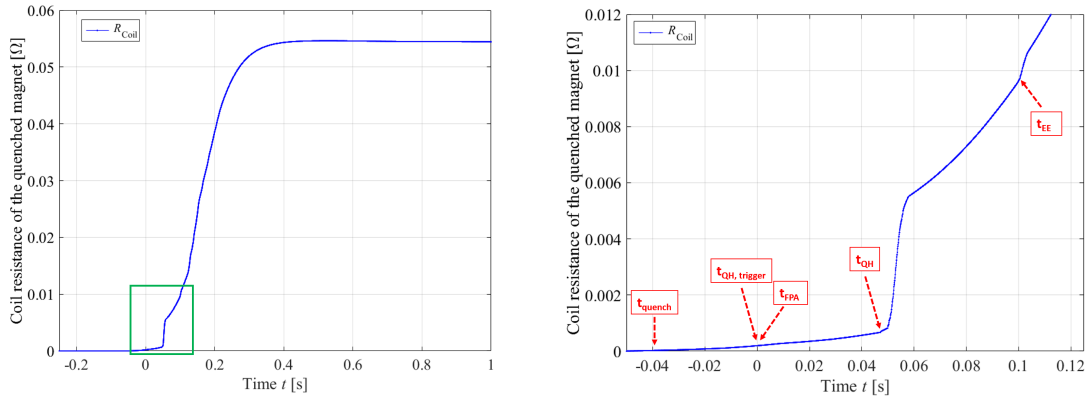

(a) Simulated resistance growth within the quenched magnet

(b) Simulated resistance growth within the quenched magnet. Detailed view of the FPA, QH activation and the EE-activation

Figure 6.7: General (a) and detailed (b) plot of the resistance growth of the quenched magnet. Simulated with COSIM (STEAM-LEDET and PSpice©

Especially 6.7 b shows very good the single events during the simulation. According to the signals from the PM Browser, the quench time of the initial hot-spot of the magnet was specified to be t_{quench} = - 38 ms within the field model in SIGMA-LEDET. The FPA was set to $t_{\mathrm{FPA}} = 0$ s and the quench heater triggering to $t_{\mathrm{QH,trigger}}$ = -3 ms. This assumption relies on the delays of different controllers used for the quench heaters and for the power converter. The heater-induced quench can be noticed at $t_{\mathrm{QH}} = 50$ ms and

forces a part of the coil to heat up. This results in a strong resistance growth. The activation of the energy-extraction system is visible due to another discontinuity appears within the resistance plot. As explained above, the opening voltage of the cold by-pass diode is $U_{\mathrm{D,open,1.9K}} \approx 6$ V. When the voltage across the magnet value reaches this value, the current starts by-passing the quenched magnet and flowing trough the diode (see figure 6.1). This transient is reproduced in figure 6.8, where the current of the circuit, together with the current through the magnet, and the current through the protection diode are plotted.

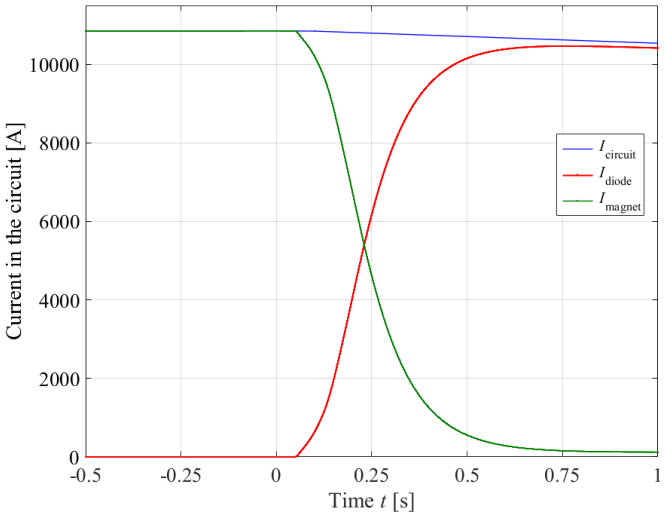

Figure 6.8: Simulated current distribution during the discharge. Protecting the quenched magnet with the diode. Simulated with COSIM (STEAM-LEDET and PSpice©).

As visible in figure 6.8, the current through the magnet (I_{m}) starts significantly decreasing at the time when the heater-induced quench is visible, at $t_{\mathrm{QH}} = 50$ ms. Due to the quench heaters, the resistance growth is much larger and as a result the opening voltage of the diode is reached more quickly and the current starts bypassing the quenched magnet. It can be noticed that this optimal combination of diode and quench heaters can decrease the current through the quenched magnet to a value of almost $I_{\mathrm{m}} \approx 0$ A in less than 1 second to protect him. In fact, the current through the magnet decreases to 10 % ($I_{\mathrm{m}} \approx$ 1085 A) of its initial value within $\Delta t_{\mathrm{sim}} \approx 0.22$ s, with respect to the moment when the current starts decreasing. This results in a large inductive voltage component due to $U_{\mathrm{ind}} = L_{\mathrm{m}} \cdot dI_{\mathrm{m}}/dt = 5.6$ mH $\cdot$ 44600 A/s ≈ 250 V. This inductive component can be noticed within figure 6.9 which is another interesting signal to discuss.

The voltage across the magnet is considered. Figure 6.9 shows the resistive voltage, the inverted inductive voltage and the coil voltage across the magnet U_{coil}, its resistive component U_{res}, and its inductive component U_{ind}. Due to the diode opening the current starts by-passing the magnet. Due to this current change ($\mathrm{d}I_{\mathrm{m}}/\mathrm{d}t$), a voltage starts developing with $U_{\mathrm{ind}} = L \cdot (\mathrm{d}I_{\mathrm{m}}/\mathrm{d}t)$. The developed inductive voltage counteracts resistive voltage. Both of these voltages can reach several hundred volts, as visible in figure 6.9 a. Since the

total voltage is fixed to the value of the diode opening voltage, both voltages cancel each other out almost completely. Only the voltage that developed before the diode opening remains as the resistive part within the coil voltage, because the diode is not open yet. This can be observed in figure 6.9 b.

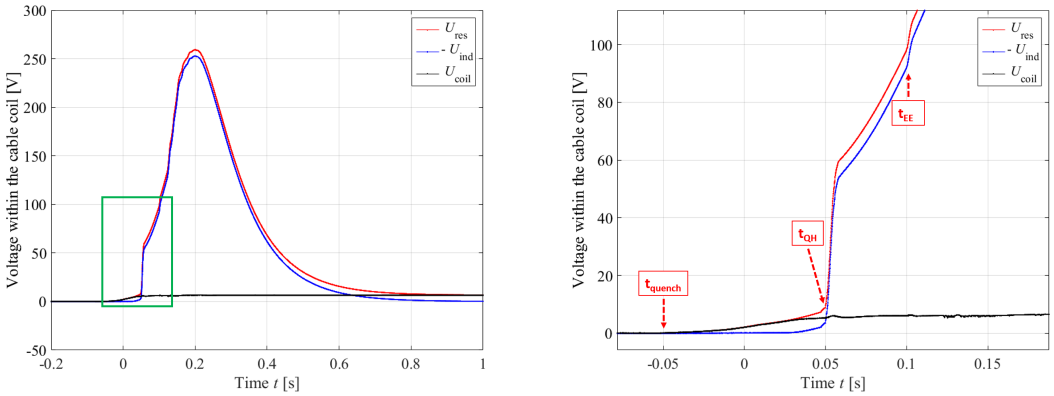

(a) Simulated resistive, dynamic and coil voltage of the quenched magnet

(b) Simulated resistive, dynamic and coil voltage of the quenched magnet. Zoomed section of the quench, the QH activation and the EE-activation

Figure 6.9: General (a) and zoom (b) plot of the different voltages across the quenched magnet. Simulated with COSIM (STEAM-LEDET and PSpice©).

The diode characteristics start changing, due to the energy deposit in the diode coming from the current. As explained in chapter 2.2.2.2, the forward characteristic of the diode depends on the temperature. When the diode opening voltage of $U_{\mathrm{D}} = 6$ V is reached, the current will start passing through the diode. After $t_{\mathrm{sim}} \approx 0.6$ s the complete current is passing through the diode. In this sense, the current passing through both diode models should be almost identical. Therefore, figure 6.10 can be considered and shows the current passing though the diode for the static and the new diode model. The current through the diode is unfortunately not measured and thus it cannot be compared with the simulated currents of both models.

Another comparison between the static and the new diode model could be the power deposited within the diode during the transient, which is shown in figure 6.11. From figure 6.11 it becomes clear that the calculated difference with the calculated power from these two different models is significant. The calculated power is the product between the voltage across the diode and the current through the diode. The power calculated with the new diode model is four times lower than with the static model. Thus, the new diode model provides a more accurate behaviour.

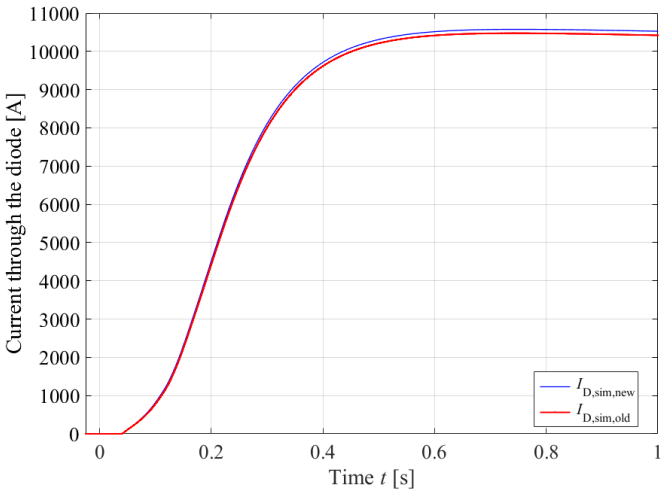

Figure 6.10: Simulated current through the protection diode. Comparison between static and new diode model. Simulated with COSIM (STEAM-LEDET and PSpice©).

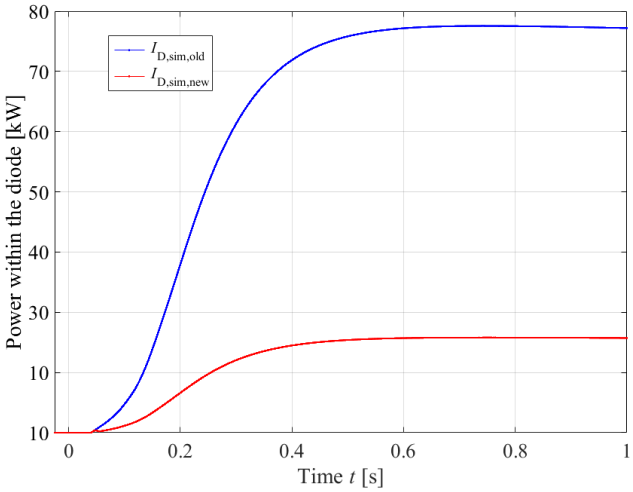

Figure 6.11: Simulated power deposited in the protection diode. Comparison between static and new diode model. Simulated with COSIM (STEAM-LEDET and PSpice©).

To see the behaviour of the magnet (field) model during the discharge more detailed, the simulated temperature signals can be considered. At first, the temperature of the half-turns over time can be considered in figure 6.12.

In figure 6.12 the hot-spot temperature starts increasing at the quench time of the magnet (see also figure 6.7). This occurs about 38 ms before the time at which the power rack connection of the power converter is opened at $t_{\mathrm{FPA}} = 0$ s. Due to the heat propagation between the half-turns the neighboring turns of the hot-spot are heated up and finally transferred to the normal conducting state as well. Considering the behaviour of the hot-spot temperature, it can be noticed that the magnet is well protected, because its hot-spot temperature remains below 180 K. Another interesting temperature plot to see the heat propagation is the two-dimensional temperature plot within the magnet cross-section. Therefore, figure 6.13 and 6.14 can be considered.

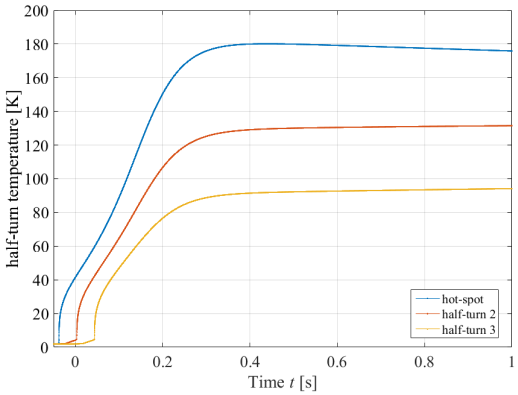

(a) Simulated temperature of the half-turns close to the hot-spot

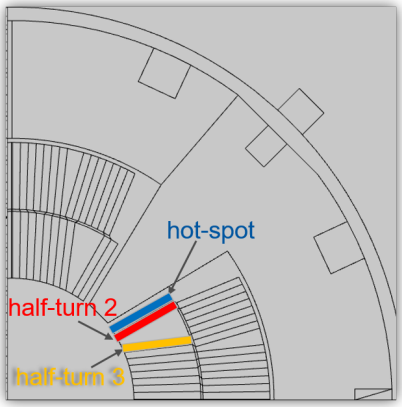

(b) Location of the hot-spot and the neighbouring half-turns within the magnet cross-section. Window from COMSOL©.

Figure 6.12: (a) Temperature over time plot of the hot-spot and his neighboring half-turns (b) corresponding and location within the magnet cross-section. Simulated with COSIM (STEAM-LEDET and PSpice©).

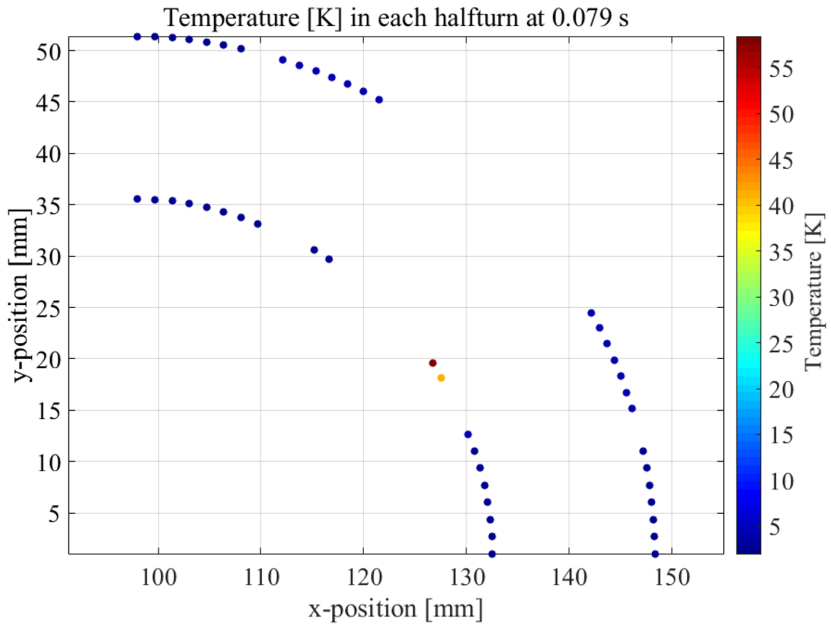

Figure 6.13: Simulated temperature of the half-turns within the cross-section of one pole of the LHC MQ magnet at $t_{\text{sim}} = 79$ ms. Heat propagation from the hot-spot. Quench heaters are already triggered, but not visible. Simulated with COSIM (STEAM-LEDET and PSpice©).

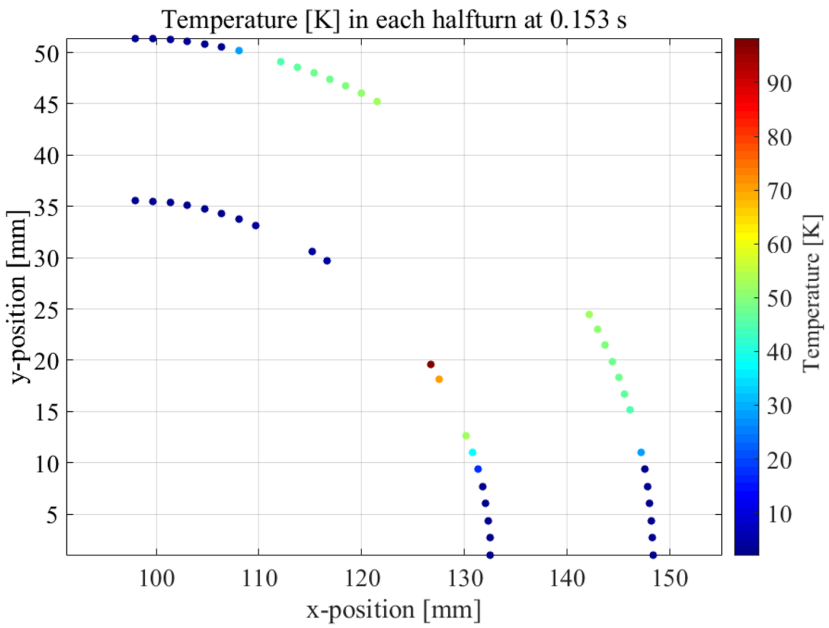

Figure 6.14: Simulated temperature of the half-turns within the cross-section of one pole at t_{sim} = 153 ms. Quench heaters are heating up the connected half-turns. Simulated with COSIM (STEAM-LEDET and PSpice©).

To better understand the behaviour of thermal propagation within the magnet, figure 6.13 and 6.14 have to be discussed more in detail. The several events during the discharge are mentioned in figure 6.7 b. The electrical resistance of the hot-spot starts developing at t_{quench} = -38 ms. Since the high current is still passing through the magnet, high ohmic loss develops in the hot-spot, whose temperature reaches 60 K after 79 ms. The quench heaters are already activated and start heating up the half-turns to which they are glued. This becomes more clear from the temperature distribution at t_{sim} = 153 ms. The temperature of the cable half-turns close to the quench heaters increases visibly. Furthermore, the heat propagates from the hot-spot to its neighboring half-turns, as shown in figure 6.14. The heat exchange between the inner and the outer cable layer is properly modelled by adding heat exchange properties between this layers (see chapter 3).

6.4 Simulating failure cases

After the validation of the model against measurement data of a quench event is successfully accomplished and the transient event is discussed in detail, it is interesting to simulate a failure scenario, when half or all of the quench heaters of the quenched magnet are not activated. For redundancy reasons, the quench heaters are connected within two independent circuits. In case one of the quench heater power supplies will not be able to trigger the quench, the other circuit is designed to transfer enough of the coil to the normal state to safely discharge the magnet. To simulate such events, the STEAM-LEDET magnet model was adapted while the circuit model remained unchanged.

In the first failure case, the quench heaters glued to the coil of the upper magnet poles

are not activated. Such a failure is not unlikely to happen and simulating such a case can provide important information about the development of the hot-spot temperature and the voltages across the magnet.

The second failure case simulates the complete absence of protection by quench heaters. In this case none of the quench heaters are triggered. This case was not observed during the LHC operation and it is extremely unlikely to occur. In fact, the probability that both quench heater power supplies fail simultaneously and as a result none of the quench heaters is triggered is very low. Thus, investigating this case has purely academic interest.

For both cases no validation data are available. Therefore, it is interesting to compare the simulated results of the cases with full, half, and missing quench heater protection. As a first signal the coil resistance is considered. Figure 6.15 shows the coil resistance for all three cases.

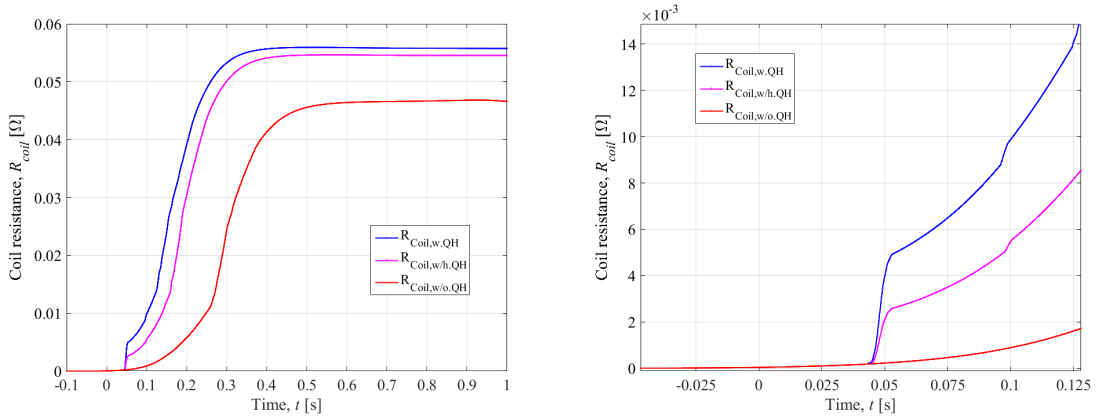

(a) Simulated resistance growth within the quenched magnet. Comparison between full, half, and missing quench heater protection

(b) Simulated resistance growth within the quenched magnet. Comparison between triggered and non-triggered quench heaters. Zoomed initial section.

Figure 6.15: Simulated resistance growth within the quenched magnet. Comparison between full, half, and missing quench heater protection. (a) General (b) Zoomed initial section. Simulated with COSIM (STEAM-LEDET and PSpice©).

In figure 6.15 b the difference of resistance growth comparing the cases can be noticed. The quench is set to occur in all three cases at t_{quench} = - 38 ms. According to the previously discussed events, here the quench heaters and the FPA are triggered as well at $t_{\text{QH,trigger}}$ = -3 ms and t_{FPA} = 0 s, respectively. Due to the heater induced quench in case of all quench heaters are triggered or partially triggered, the resistance starts growing stronger after t_{sim} = 50 ms and reaches a value of $R_{\text{Coil,w.QH}} = \approx 0.056\ \Omega$ and $R_{\text{Coil,w/h.QH}}$ = 0.055 Ω, respectively. Thus, the absence of half of the quench heaters reduces the final resistance development only by 1.8 %. Comparing the resistance growth from the simulation with quench heater and partially non-triggered quench heaters, the heater-induced quench occurs at the same time, but the resistance value in the first moment of the heater-induced quench (t_{sim} = 50 ms) is twice lower. In the case half of the quench heaters are triggered, only parts of the coil located in one half of the magnet aperture are quenched

which results in a resistance value of $R_{\mathrm{Coil,w/h.QH}} \approx 2$ mΩ. In contrast the resistance value developing in the simulation with fully triggered quench heaters is $R_{\mathrm{Coil,w.QH}} \approx 4$ mΩ. When all quench heaters are not triggered, the cable half-turns can only be quenched by the initially quenched hot-spot, heat transfer from already quenched half-turns, and the inter-filament coupling currents (quench-back). This can be clearly seen, considering figure 6.15 a. The resistance grows slower because no quench heaters are triggered. The detailed view of the developed coil resistance (see figure 6.15 b) shows better the difference between activating and not activating the quench heaters. As explained in chapter 2.2.2.1, the quench heaters are part of the quench protection system of this magnet. When the quench heaters are not triggered the energy stored within the magnet ($\approx$ 395 kJ) is distributed significantly less uniformly in the coil windings. As a consequence, a larger fraction of energy is deposited in the hot-spot, its neighboring half-turns, and the half-turns quenched to a quench-back. The temperature development in this case is extreme and interesting to observe (see figure 6.16).

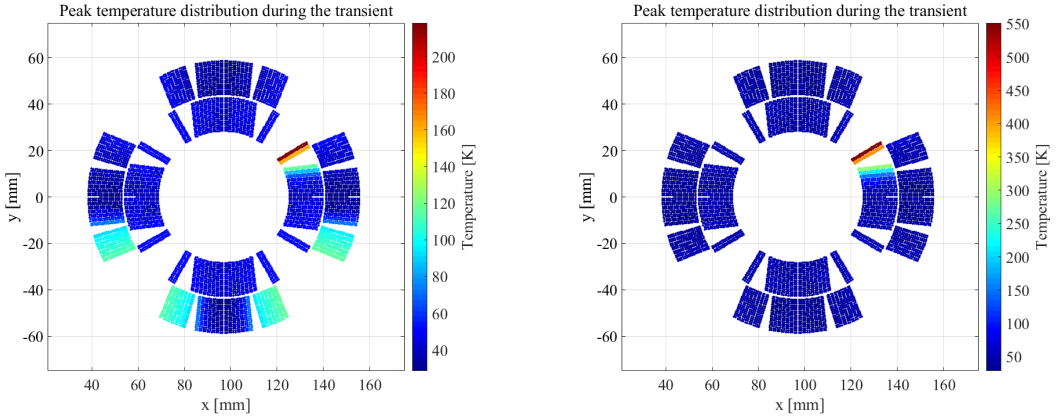

(a) Simulated peak temperature in the magnet cross-section during the transient. Case with half quench heater protection.

(b) Simulated peak temperature in the magnet cross-section during the transient. Case with missing quench heater protection.

Figure 6.16: Simulated peak temperature in the magnet cross-section during the transient. (a) Case with half quench heater protection. (b) Case with missing quench heater protection. Simulated with COSIM (STEAM-LEDET and PSpice©).

In case of partially not triggered quench heaters, the hot-spot temperature remains below 250 K. In terms of magnet design a maximum permissible temperature is often set to be 300 K. Thus, even with only one half of the quench heaters triggered, the magnet is well protected. In case of non of the quench heaters will be triggered, the hot-spot temperature reaches more than 500 K. At this temperature, the insulation of the cable coil would likely be damaged and the magnet destroyed. If this accident happened during the operation of the LHC machine, the result would be the stop of the LHC operation for several months. During the discharge, the large current passes through a small volume of quenched half-turns. This results in large ohmic losses within these half-turns and finally in a very high temperature as visible in figure 6.16 b.

Another interesting signal to consider is the current distribution between the quenched magnet and its protection diode during the transient. As explained before, when the diode opening voltage is, reached the current starts by-passing the magnet. It is interesting to see, when the current starts by-passing the magnet in all three cases. Therefore, figure 6.17 can be considered.

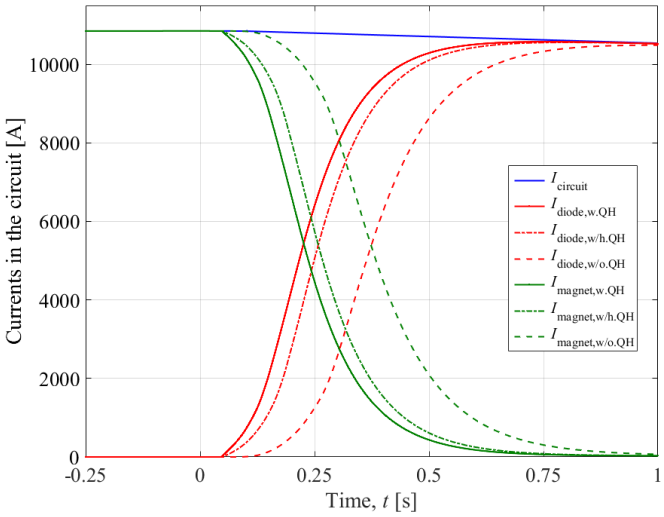

Figure 6.17: Simulated current distribution. Comparison of the cases with full, half, and missing quench heater protection. Simulated with COSIM (STEAM-LEDET and PSpice©).

In figure 6.17 the current through the diode starts increasing and simultaneously the current through the magnet starts decreasing. In fact, the sooner the current starts passing through the diode the better this is in terms of magnet protection. The development of the voltage across the magnet is linked with the coil resistance development which depends on the presence of the quench heaters. Thus, the small difference between developed resistance can also be noticed in the current signal. Due to the slower resistance growth in case of fully not triggered quench heaters, the current decreases more slowly, with respect to the reference case. The magnet current related to the case with partially not triggered quench heaters starts decreasing at the same time like the one in case with completely triggered quench heaters. Thus, with only half of the quench heaters present the magnet is still protected and the energy in terms of current is extracted almost at the same time as with fully present quench heaters.

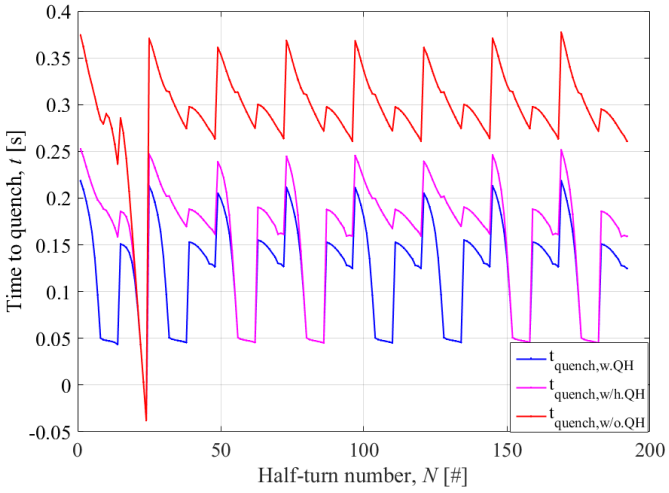

Figure 6.18: Simulation results for Time to quench over the half-turn number. t_{quench} = - 38 ms. Comparison of the cases with full, half, and missing quench heater protection. Simulated with COSIM (STEAM-LEDET and PSpice©).

Finally, the time at which each half-turn individually quenched over the number of this half-turn is analyzed. This is shown in figure 6.18. Half-turn Nr. 24 quenched initially at t_{quench} = - 38 ms in all three cases. Comparing the signal related to the cases with partially and fully triggered quench heaters, the half-turns which were quenched due to heat propagation or due to a quench-back can be identified. In fact, their time to quench is up to 150 ms later with respect to the ones that were quenched by quench heaters. In case of completely not triggered quench heaters, the time to quench is significantly higher with respect to the reference case which causes most of the energy to be deposited in the hot-spot and increase its temperature.

6.4.1 Short summary related to the co-simulation results

Within this chapter, the co-simulation results were discussed. Within the co-simulation one magnet was set to quench within the main quadrupole circuit. The current discharge can be reproduced and is in very good agreement with the measured current. Moreover, the initial resistance growth can be reproduced by using the new developed function of quench propagation velocity. The distribution of the circuit current between the quenched magnet and the cold by-pass diodes shows clearly the relation to the initial resistance growth coming from the hotspot and the strong resistance growth coming from enabling the quench heaters. During the process of co-simulation a new model of the cold by-pass diodes was developed, tested and validated against the measured voltage of the diode. The new diode model reproduces the measured behavior more accurately than the previously used model which is an improvement not only for modelling main quadrupole circuits, but also for the main dipole circuits. Thus, the co-simulation model and the new developed diode model are successfully validated and can be used for further investigations, reproducing unexpected events during LHC operation for example.

Chapter 7

Conclusion and Outlook

7.1 Conclusion

In this thesis, the main goal was to develop, validate, and characterize the model of the LHC main quadrupole superconducting magnet and its circuit using the STEAM (Simulation of Transient Effects in Accelerator Magnets) framework. Thematically this topic is located within the quench protection studies. Therefore, the simulation of transient effects related to a quench and to magnet protection are of particular interest within this thesis. Coupled electro-magnetic and thermodynamic transients in superconducting magnets are complex processes, which require expertise from different fields and dedicated software. For this aim the STEAM framework was developed at CERN. The framework includes multiphysical simulation tools, automated model generation, and a cooperative-simulation program. Its applications include reproducing unexpected events occurred in the LHC circuits, simulating failures cases, and analyzing proposed improvements to the existing quench protection system. During the last project within the STEAM framework, several magnet models for the LHC, the HL-LHC and the FCC were developed.

The LHC main quadrupole magnets are responsible for focussing and de-focussing the particle beams, hence controlling their width and height. These magnets are located in each of the LHC arcs. The LHC main quadrupole magnet features two electrically-separated apertures located in a common cold-mass, which are operated at cryogenic temperature of 1.9 K. At a nominal current of 11870 A , a magnetic field gradient of 223 T/m in the aperture and a peak field of 6.85 T in the conductor are achieved [9]. This magnet's protection system is based on quench heaters and individual by-pass diodes.

The generation of the 2D electro-magnetic and thermal model of this magnet was performed using the programs STEAM-SIGMA and STEAM-LEDET. Within STEAM-SIGMA, a model for a finite-element solver (here COMSOL ©) was generated. Within STEAM-LEDET, a model based on an equivalent lumped-element approach was developed. Both models consider the effect of quench heaters, heat transfer between adjacent turns and layers, coupling currents, and the effect on the heat capacity of helium impregnating the conductor. During the modelling process within this thesis, a new model feature was developed and implemented both in SIGMA and LEDET. This feature provides a

more accurate calculation of the initial resistance growth in the hot-spot without recurring to a full 3D model. The quench propagation is modelled using a function calculating a certain quench propagation velocity. Due to this velocity the initial resistance growth is modelled more accurate than used a pure 2D assumption where the complete half-turn is quenched immediately. This feature is determinant for the simulation of the first phase of the transient, where the only resistance in the coil is that developed in the hot-spot. The validation of both models was performed with measurement data from tests performed at the CERN magnet test facility. During the validation process, the measured current during the discharge and the experimental coil resistance, calculated using the measured current and coil voltage, were compared to simulated signals and found in good agreement. Moreover, the influence of the main model parameters was investigated. The most significant influence on the simulation results is coming from the implemented helium fraction, due to its very high contribution of heat capacity at cryogenic temperatures, which greatly increases the amount of energy required to quench the conductor.

Furthermore, the LHC main quadrupole circuit model was generated and validated. The main circuit components include a series of 47 or 51 magnets (focussing or defocussing), a power supply, a crowbar-switch, an energy-extraction system, an earthing system, and resistances in the non-cryogenic parts of the circuit. The model was developed using the software PSpice ©). The models and library components were generated using netlists, which allows increased modelling flexibility and modularity and the possibility of rapidly modifying and versioning the model and its components. After the model was generated and all components were individually tested, it was validated using experimental data from an LHC hardware commissioning test campaign. The signals used for the validation were the circuit current, the voltage across the power converter, the voltage across the energy-extraction resistor, and the current to ground passing through the earthing system of the circuit. After successfully validating separately the electromagnetic and thermal magnet model and the electrical circuit model, they were both used in a cooperative-simulation using the software STEAM-COSIM. A cooperative-simulation allows to combine field (magnet) and circuit models within one simulation exchanging information between the domains. In the present application, this allowed to simulate a quenching magnet within a chain of magnets remaining at superconducting state, which achieves a more accurate simulation of the transients occurring in the circuit during a quench transient. The co-simulation is performed by a specific tool, which at each time-window assigns the current wave-form calculated with the circuit model to the field model. Using this current wave-form, the field model simulates the same time-window and provides the calculated magnet voltage and coil resistance of the quenched magnet to the circuit model. This iteration of simulations and the information exchange is repeated until the set residual relative and absolute error is reached. The measurement data for validating the co-simulation results come from a training quench occurred in a magnet of the LHC main quadrupole circuits, at a current level close to the nominal value. The signals used for the validation were the circuit current and the voltage across the magnet, which is by-passed

by a protection diode. Both signals are in good agreement with the measurement data during different phases of the analyzed transient. Thus, the co-simulated model can be considered successfully validated in this operating condition.

During this validation process another new feature was developed and implemented in the PSpice© circuit model. The model of the protection by-pass diode was significantly improved by including the dependence of the diode voltage-current characteristic on its thermal condition. In nominal operations, the diode works at cryogenic temperature. After a sufficient resistive voltage develops in the quenched magnet and the diode opening voltage is reached, a current starts flowing through the diode. The high current produces ohmic losses in the diode and as a result the diode heats up. As a consequence, its voltage-current characteristic varies due to the temperature change. The new model accounts for this mechanism in a simple way, where a linear correlation between the deposited energy in the diode and one parameter defining its characteristics is assumed. With this approximation, a good agreement with the measured data can already be achieved. It was demonstrated that the STEAM framework allows to generate superconducting magnet and circuit models including complex multiphysics phenomena. The models were developed within the framework of this thesis, and successfully validated against experimental results. Furthermore, various new feature were developed to improve the model accuracy when simulating specific transients, such as the initial quench development in the hot-spot and the cryogenic diode thermal behavior. These features can be easily implemented in similar models within the STEAM framework. The cooperative-simulation model can be used for simulating several failure cases during the LHC operation.

7.2 Outlook

The co-simulated model of the LHC main quadrupole magnet and circuit, as well as the developed diode model and the developed function for implementing a finite quench propagation velocity can be used for subsequent investigations and projects. For example, the circuit and magnet models can be used for simulating unexpected events or failure cases within the LHC main quadrupole circuit. This would allow to predict some events and propose optimization for the quench protection system. Moreover, it could be interesting to launch a special test campaign for the LHC main quadrupole circuit, where several cases during the LHC operation could happen. The main quadrupole circuit model could be used to validate the simulation results against measured signals from this test campaign.

Moreover, the developed diode model could be used also for the LHC main dipole circuit model. The protection by-pass diodes used for the main quadrupole circuits are the same as for the main dipole circuits. Within the LHC main dipole circuits the effect of propagating voltage waves were observed as a reaction of a quench within one magnet [60]. This cause to trigger the quench protection system of the neighboring magnets. With an improved diode model for the protection diodes this effect could be simulated more accurately and allows to propose improvements for the quench protection system of the LHC main dipole circuit. An improvement of the diode model is also conceivable approach for further developments. For example a finite-element model of the protection by-pass diode could be generated, where the correct correlation between stored energy, increasing diode temperature and changing diode characteristics could be implemented. This model could be validated against tests done for this protection diode [61]. It could be even considered, coupling this diode model with the main quadrupole circuit model using a co-simulation.

The procedure shown within this thesis using the tools provided in the STEAM framework for automated model generation and simulating of transient behaviour in complex circuit and magnet models can be adapted on more circuits of the LHC, the HL-LHC and the FCC. Moreover, this approach can be extended for superconducting circuits of other accelerator complexes like FAIR.

Bibliography

[1] L. Bortot and et al. "STEAM: A Hierarchical Co-Simulation Framework for Superconducting Accelerator Magnet Circuits". In: Transactions on Applied Superconductivity LHC-Project-Report-485. CERN-LHC-Project-Report-485 (2017), p. 3. DOI: 10.1109/TASC.2017.2787665.

[2] Michal Maciejewski. "Co-Simulation of Transient Effects in Superconducting Accelerator Magnets". Presented 10 May 2019. Oct. 2018. URL: https://cds.cern.ch/record/2675039.

[3] D. Hagedorn, W. Nägele. Quench Protection Diodes for the Large Hadron Collider. Tech. rep. 148. June 1991. URL: https://cds.cern.ch/record/227194/files/CM-P00063402.pdf.

[4] L. Bortot, B. Auchmann, I. Cortes Garcia, A.M. Fernandez Navarro, M. Maciejewski, M. Prioli, S. Schops, and A.P. Verweij. "A 2-D Finite-Element Model for Electro-Thermal Transients in Accelerator Magnets". In: LHC Project Report 623 (Mar. 2018), p. 4. URL: http://cds.cern.ch/record/2302445/files/arXiv:1710.01187.pdf.

[5] Maciejewski, Michal. "Automated Object-Oriented Simulation Framework for Modelling of Superconducting Magnets at CERN". Presented 11 Sep 2014. Sept. 2014. URL: https://cds.cern.ch/record/2025032.

[6] E. Ravaioli et al. "Lumped-Element Dynamic Electro-Thermal model of a superconducting magnet". In: Cryogenics 80 (2016). Chats on Applied Superconductivity 2015 University of Bologna, Italy, 14-16 September 2015, pp. 346–356. ISSN: 0011-2275. DOI: https://doi.org/10.1016/j.cryogenics.2016.04.004. URL: http://www.sciencedirect.com/science/article/pii/S0011227516300832.

[7] Emanuele Ravaioli. "CLIQ. A new quench protection technology for superconducting magnets". English. PhD thesis. University of Twente, June 2015. ISBN: 978-90-365-3908-1. DOI: 10.3990/1.9789036529081.

[8] LHC Study Group. Design Study of the Large Hadron Collider. Tech. rep. CERN-91-03. May 1991. URL: https://cds.cern.ch/record/220493/files/CERN-91-03.pdf.

[9] O. S. Bruening et al. LHC Design Report, Volume I, The LHC Main Ring. CERN Yellow Reports: Monographs. Geneva: CERN, 2004. DOI: 10.5170/CERN-2004-003-V-1. URL: http://cds.cern.ch/record/782076.

[10] Facts and Figures abotu the LHC. https://home.cern/resources/faqs/facts-and-figures-about-lhc. Accessed: 2019-06-20.

[11] Pettersson, Thomas Sven and Lefevre, P. The Large Hadron Collider: conceptual design. Tech. rep. CERN-AC-95-05-LHC. Oct. 1995. URL: https://cds.cern.ch/record/291782.

[12] M. Wilson. Superconducting Magnets for Accelerators. Lecture Slides 1. 2006.

[13] L. Bottura. Superconductors. Lecture Slides. Nov. 2012.

[14] L. Bottura. Cable Stability. CERN Yellow Reports: Monographs. Geneva: CERN, 2014. DOI: 10.5170/CERN-2014-005.401. URL: http://cds.cern.ch/record/782076.

[15] P. Schmüser K.H. Meß and S. Wolff. Superconducting Accelerator Magnets. Singapore: World Scientific, 1996.

[16] Lucio Rossi. "Superconductivity and the LHC: the early days". In: CERN Courier (2011).

[17] M.N. Wilson. Superconducting Magnets. Monographs on Cryogenics. Clarendon Press, 1983. ISBN: 9780198548102.

[18] D. Larbalestier, A. Gurevich, D.M. Feldmann, and A. Polyanskii. "High-Tc superconducting materials for electric power applications". In: Nature 414 (Nov. 2001).

[19] A P Verweij. "Electrodynamics of superconducting cables in accelerator magnets". Presented on 15 Sep 1995. 1995. URL: https://cds.cern.ch/record/292595.

[20] E. Ravaioli et al. "Modeling of Interfilament Coupling Currents and Their Effect on Magnet Quench Protection". In: IEEE Transactions on Applied Superconductivity 27.4 (June 2017), pp. 1–8. ISSN: 1051-8223. DOI: 10.1109/TASC.2016.2636452.

[21] W. J. Carr Jr. "AC loss in a twisted filamentary superconducting wire". In: Applied Physics 45 (1974).

[22] G. H. Morgan. "Theoretical Behavior of Twisted Multicore Superconducting Wire in a Time-Varying Uniform Magnetic Field". In: Journal of Applied Physics 41 (1970).

[23] Alan Herve. "The CMS Detector Magnet". In: IEEE Transactions 10.1 (2000).

[24] L. Bottura. Accelerator Magnets. Lecture Slides. 2001.

[25] L. Bottura. "Magnet Quench 101". In: Proceedings, WAMSDO 2013. [,1(2014)]. 2013, pp. 1–9. DOI: 10.5170/CERN-2013-006.1.

[26] K.H. Meß. Quench Protection. Tech. rep. Status Report. 1996, p. 4. URL: https://cds.cern.ch/record/399567/files/p143.pdf.

[27] M. Wilson. Superconducting Magnets for Accelerators. Lecture Slides 3. 2006.

[28] L. Charnay and V. Montabonnet. LHC13kA-18V LHC MQ Power Converter Guide. English. Version EDMS Doc. N973221 V.2. CERN. 2009, p. 22.

[29] Dahlerup-Petersen, K and Rodriguez-Mateos, F and Schmidt, R and Sonnemann, F. "Energy Extraction for the LHC Superconducting Circuits". In: LHC-Project-Report-484. CERN-LHC-Project-Report-484 (Aug. 2001), p. 4. URL: https://cds.cern.ch/record/514346.

[30] SCHOTTKY RECTIFIER. 440CNQ030. Data-sheet. International Rectifier.

[31] Rectifier Diode. SKN6000. Data-sheet. SEMICRON.

[32] V. Montabonnet, et al. Modular Power Converter [13KA, 16V]. Report. Tech. rep. 2001, p. 9.

[33] SCHOTTKY RECTIFIER. 249nq135-150. Data-sheet. International Rectifier.

[34] E. Ravaioli. personal communication. Apr. 15, 2019.

[35] K. Dahlerup-Petersen, B. Kazmine, V. Popov, V. Sytchev, L. Vassiliev and V. Zubko. "Energy Extraction resistors for the main dipole and the main quadrupole circuits of the LHC". In: (2000), p. 4. URL: http://accelconf.web.cern.ch/Accelconf/e00/PAPERS/THP1B09.pdf.

[36] Lucio Rossi. "The LHC Main Dipoles and Quadrupoles Toward Series Production". In: LHC Project Report 623 (Dec. 2002), p. 9. URL: https://cds.cern.ch/record/514346.

[37] STEAM team. SIGMA documentation v1.2. EDMS nr. 2141579. CERN. Geneva, Switzerland, 2019, p. 107.

[38] F Rodriguez-Mateos and F Sonnemann. "Quench Heater Studies for the LHC Magnets". In: LHC-Project-Report-485. CERN-LHC-Project-Report-485 (Aug. 2001), p. 4. URL: https://cds.cern.ch/record/514347.

[39] F Rodriguez-Mateos et al. "Quench Heater Experiments on the LHC Main Superconducting Magnets". In: LHC-Project-Report-418. CERN-LHC-Project-Report-418 (Sept. 2000), p. 4. URL: https://cds.cern.ch/record/466520.

[40] Florian Meuter. "Accelerator Magnet Quench Heater Technology and Quality Control Tests for the LHC High Luminosity Upgrade". Presented 21 Mar 2017. 2017. URL: http://cds.cern.ch/record/2258133.

[41] M. Albert R. Giachino. "LHC REPORT: A BRIEF DECELERATION". In: CERNBulletin (2015).

[42] Michal Maciejewski. STEAM Architecture. Workshop Slides. June 2019.

[43] Matthias Mentink. Development of the STEAM Comsol Magnet Simulation Tool. Tech. rep. EDMS 2054126. Geneva: CERN, 2018.

[44] NIST WEBBOOK. https://webbook.nist.gov/chemistry/. Accessed: 2019-03-30.

[45] L.J.M. can de Klundert H.H.J. ten Kate H. Boschman. "Longitudinal Propagation Velocity of the Normal Zone in Superconducting Wires". In: IEEE Transactions 23.2 (1987), p. 4.

[46] Giovanni Volpini. "Quench Propagation in 1-D and 2-D Models of High Current Superconductors". In: Proceedings of the COMSOL Conference (2009), p. 6.

[47] Michal Maciejewski. Steam Workshop Slides. Co-Simulation. June 2019.

[48] L. Dresner. "Analytic Solution for the Propagation Velocity in Superconducting Composites". In: IEEE Transactions 15.1 (1979), p. 3.

[49] L. Bottura. "Magnet Quench 101". In: WAMSDO 2013. 2013, p. 79. DOI: 10.5170/CERN-2013-006.1.

[50] E. Ravaioli, B. Auchmann, and A. P. Verweij. "Fast Method to Quantify the Collective Magnetization in Superconducting Magnets". In: IEEE Transactions 23.3 (June 2013), p. 4700204. ISSN: 1051-8223. DOI: 10.1109/TASC.2012.2227649.

[51] E. Ravaioli. LEDET manual (Lumped-Element Dynamic Electro-Thermal model). English. Version Version 1.06.03. CERN. Mar. 2019, p. 19.

[52] Z. Charifoulline. personal communication. May 3, 2019.

[53] PSpice Reference Guide. CADENCE Design Systems.

[54] R. Schmidt, C. Giloux, A. Hilaire, A. Ijspeert, F. Rodriguez-Mateos, and F. Sonnemann. Protection of the Superconducting Corrector Magnets for the LHC. Tech. rep. 419. 2000. URL: https://accelconf.web.cern.ch/accelconf/e00/PAPERS/THP2A08.pdf.

[55] E. Ravaioli et.al. "Impact of the Voltage Transients After a Fast Power Abort on the Quench Detection System in the LHC Main Dipole Chain". In: IEEE Transactions 22.3 (2012).

[56] E. Ravaioli et.al. "Modeling of the Voltage Waves in the LHC Main Dipole Circuits". In: IEEE Transactions 22.3 (2012).

[57] MP3. Hardware Commissioning Test procedure for the LHC main quadrupole circuits. Tech. rep.

[58] E. Ravaioli. STEAM LEDET - Tutorial. English. Version "Version 0.2". CERN. Mar. 2019, p. 37.

[59] W. Shockley. "The Theory of p-n Junctions in Semiconductors and p-n Junction Transistors". In: The Bell System Technical Journal 28.3 (1949).

[60] E. Ravaioli, A.P. Verweij, and H.H.J. ten Kate. "Unbalanced Impedance of the Aperture Coils of Some LHC Main Dipole Magnets". In: IEEE Transactions (June 2013), p. 4. URL: https://ieeexplore.ieee.org/document/6353175.

[61] A Monteuuis. HL-LHC Inner Triplets 18kA cold bypass diode irradiation campaign. Dec. 2018.

Chapter 8

Annex for chapter 4

This Annex contains information about the chosen cable parameters and excerpts from the with STEAM-SIGMA generated model.

Table 8.1: Main parameters of the conductor used in the main quadrupole magnet model

Variable name	**Description**	**Unit**	**Value**
label	Custom name for cable	-	
wInsulNarrow	Thickness of insulation along narrow side of cable	m	0.15e-3
wInsulWide	Thickness of insulation along wide side of cable	m	0.13e-3
dFilament	Diameter of filament in strand	m	6e-6
dstrand	Diameter of strand in cable	m	0.825e-3
fracCu	Fraction of copper in conductor	1	1.95/(1+1.95)
fracSc	Fraction of non-copper material in conductor	1	1/(1+1.95)
RRR	Residual-resistivity ratio (RRR) of copper	1	150
TupRRR	Reference temperature for RRR measurements	K	295
Top	Operation temperature of cable	K	1.9
Rc	Cross-contact resistance between strands	Ω	100e-6
Ra	Adjacent contact resistance between strands	Ω	10e-6
fRhoEff	Effective parameter for the transverse resistivity of copper	1	1
lTp	Filament twist-pitch	m	15e-3
wBare	Width of bare cable	m	1.51e-2
hInBare	Smaller height of cable	m	1.362e-3
hOutBare	Larger height of cable	m	1.598e-3
noOfStrands	Number of strands in each cable	1	36
noOfStrandsPerLayer	Number of strands in each layer of cable	1	18
noOfLayers	Number of layers in each cable	1	2

Continued on next page

Table 8.1 – continued from previous page

Variable name	Description	Unit	Value
lTpStrand	Strand twist pitch	l	0.100
wCore	Width of cable core	m	0
hCore	Height of cable core	m	0
thetaTpStrand	Strand twist-pitch angle; by default, this can be calculated as atan2((wBare-dstrand),(lTpStrand/2))	rad	-
fracHe	Fraction of helium relative to cable conductor surface area	1	0.035
fracFillInnerVoids	Filling fraction of insulation in inner voids	1	1
fractFillOuterVoids	Filling fraction of insulation in outer voids	1	1
resitivityCopperFit	The fit used for copper	-	-
criticalSurfaceFit	Defines scaling relationship used to discribe the critical current density of the superconductor	-	-
insulationMaterial	Insulation material	-	-
materialInnerVoids	Inner voids insulation material	-	-
materialCore	Cable core material	-	-
materialOuterVoids	Outer voids insulation material	-	-

Listing 8.1: Input file for the magnet generation within IntelliJ©. Written in JAVA.

```
1  package input.Others.MQ;
2
3  import model.domains.Domain;
4  import model.domains.database.*;
5  import model.geometry.Element;
6  import model.geometry.basic.*;
7  import model.geometry.coil.*;
8  import model.materials.database.MatDatabase;
9  import input.UtilsUserInput;
10
11
12   // Created by Dimitri Pracht on 15/03/2019.
13
14 // (...)
15
16
17
18      public Element[] airFarField() {
19          // POINTS
20
21          double r = 1;
```

```
22
23          Point kpc = Point.ofCartesian(0, 0);
24          Point kp1 = Point.ofCartesian(r, 0);
25          Point kp2 = Point.ofCartesian(0, r);
26
27          Point kp1_far = Point.ofCartesian(r * 1.05, 0);
28          Point kp2_far = Point.ofCartesian(0, r * 1.05);
29
30          // LINES
31          Line ln1_far = Line.ofEndPoints(kp1, kp1_far);
32          Arc ln2_far = Arc.ofEndPointsCenter(kp1_far, kp2_far, ↩
                kpc);
33          Line ln3_far = Line.ofEndPoints(kp2_far, kp2);
34          Arc ln4_far = Arc.ofEndPointsCenter(kp2, kp1, kpc);
35
36          Area ar1_far = Area.ofHyperLines(new HyperLine[]{↩
                ln1_far, ln2_far, ln3_far, ln4_far});
37
38
39          Element el1_far = new Element(columns"columnsFAR_El1↩
                columns", ar1_far);
40
41
42          // ELEMENTS DISTRIBUTED OVER QUADRANTS
43          Element[] quad1 = {el1_far};
44
45
46          return new Element[]{el1_far};
47      }
48
49
50      public Coil coil() {
51
52
53          Point kp0 = Point.ofCartesian(0, 0);
54
55
56  //      first qauter of the right "tube"
57
58          Point kp11 = Point.ofCartesian(139.5222e-3-beamd, ↩
                11.0877e-3);
59          Point kp12 = Point.ofCartesian(140.7287e-3-beamd, ↩
                0.1378e-3);
60          Point kp13 = Point.ofCartesian(156.0430e-3-beamd, ↩
                0.1378e-3);
61          Point kp14 = Point.ofCartesian(154.7481e-3-beamd, ↩
                12.7316e-3);
```

```
62
63
64
65
66
67          Point kp21 = Point.ofCartesian(134.8117e-3-beamd, ↩
                22.3833e-3);
68          Point kp22 = Point.ofCartesian(138.9950e-3-beamd, ↩
                12.1936e-3);
69          Point kp23 = Point.ofCartesian(153.7051e-3-beamd, ↩
                16.4534e-3);
70          Point kp24 = Point.ofCartesian(148.9795e-3-beamd, ↩
                28.1974e-3);
71
72
73          Point kp31 = Point.ofCartesian(122.4836e-3-beamd, ↩
                12.5449e-3);
74          Point kp32 = Point.ofCartesian(124.9158e-3-beamd, ↩
                0.1373e-3);
75          Point kp33 = Point.ofCartesian(140.2301e-3-beamd, ↩
                0.1373e-3);
76          Point kp34 = Point.ofCartesian(137.6824e-3-beamd, ↩
                14.4225e-3);
77
78
79
80
81          Point kp41 = Point.ofCartesian(119.7246e-3-beamd, ↩
                16.3806e-3);
82          Point kp42 = Point.ofCartesian(121.3343e-3-beamd, ↩
                13.6815e-3);
83          Point kp43 = Point.ofCartesian(134.6869e-3-beamd, ↩
                21.1808e-3);
84          Point kp44 = Point.ofCartesian(132.8404e-3-beamd, ↩
                24.2865e-3);
85
86
87
88          //      second qauter of the right "tube"
89
90
91  //          Point kp0 = Point.ofCartesian(-97e-3, 0);
92
93          Arc ln11 = Arc.ofEndPointsCenter(kp12, kp11, kp0);
94          Line ln12 = Line.ofEndPoints(kp12, kp13);
95          Arc ln13 = Arc.ofEndPointsCenter(kp13, kp14, kp0);
96          Line ln14 = Line.ofEndPoints(kp11, kp14);
```

```
97  //
98          Arc ln21 = Arc.ofEndPointsCenter(kp22, kp21, kp0);
99          Line ln22 = Line.ofEndPoints(kp22, kp23);
100         Arc ln23 = Arc.ofEndPointsCenter(kp23, kp24, kp0);
101         Line ln24 = Line.ofEndPoints(kp21, kp24);
102
103
104
105         Arc ln31 = Arc.ofEndPointsCenter(kp32, kp31, kp0);
106         Line ln32 = Line.ofEndPoints(kp32, kp33);
107         Arc ln33 = Arc.ofEndPointsCenter(kp33, kp34, kp0);
108         Line ln34 = Line.ofEndPoints(kp31, kp34);
109
110
111         Arc ln41 = Arc.ofEndPointsCenter(kp42, kp41, kp0);
112         Line ln42 = Line.ofEndPoints(kp42, kp43);
113         Arc ln43 = Arc.ofEndPointsCenter(kp43, kp44, kp0);
114         Line ln44 = Line.ofEndPoints(kp41, kp44);
115 //
116         Area ha11p = Area.ofHyperLines(new HyperLine[]{ln11, ↩
               ln12, ln13, ln14});
117         Area ha12p = Area.ofHyperLines(new HyperLine[]{ln21, ↩
               ln22, ln23, ln24});
118         Area ha13p = Area.ofHyperLines(new HyperLine[]{ln31, ↩
               ln32, ln33, ln34});
119         Area ha14p = Area.ofHyperLines(new HyperLine[]{ln41, ↩
               ln42, ln43, ln44});
120
121
122         Area ha11n = ha11p.mirrorY().rotate(-0.5*(Math.PI));
123         Area ha12n = ha12p.mirrorY().rotate(-0.5*(Math.PI));
124         Area ha13n = ha13p.mirrorY().rotate(-0.5*(Math.PI));
125         Area ha14n = ha14p.mirrorY().rotate(-0.5*(Math.PI));
126
127
128
129
130         Winding w11_R = Winding.ofAreas(new Area[]{ha11p, ↩
               ha11n}, new int[]{+1,-1}, 7, 7, new Cable_MQ());
131         Winding w12_R = Winding.ofAreas(new Area[]{ha12p, ↩
               ha12n}, new int[]{+1,-1}, 7, 7, new Cable_MQ());
132         Winding w13_R = Winding.ofAreas(new Area[]{ha13p, ↩
               ha13n}, new int[]{+1,-1}, 8, 8, new Cable_MQ());
133         Winding w14_R = Winding.ofAreas(new Area[]{ha14p, ↩
               ha14n}, new int[]{+1,-1}, 2, 2, new Cable_MQ());
134
135         // poles:
```

```
136         Pole p1 = Pole.ofWindings(new Winding[]{w11_R, w12_R, ↩
                w13_R, w14_R}).translate(0,0);
137
138
139         Pole p2 = p1.mirrorY();
140
141         Pole p3 = p1.mirrorY().mirrorX();
142         Pole p4 = p1.mirrorX();
143
144
145         // Coil:
146         Coil c1 = Coil.ofPoles(new Pole[]{p1, p2});
147
148         return c1;
149
150     }
151
152
153
154
155     public Element[] iron_yoke() {
156
157
158         // KEYPOINTS
159
160         Point kp0 = Point.ofCartesian(0, 0);
161         Point kp0_1 = Point.ofCartesian(97e-3, 0);
162
163
164         Point kpbt1 = Point.ofCartesian(beamd+rbt,0);
165
166
167         Point kpbt2 = Point.ofCartesian(beamd+(rbt+dbarbt)*↩
                Math.cos(phibt),(rbt-dbarbt)*Math.sin(phibt));
168         Point kpbt3 = Point.ofCartesian(beamd+(rbt-dbarbt)*↩
                Math.cos(phibt),(rbt+dbarbt)*Math.sin(phibt));
169         Point kpbt4 = Point.ofCartesian(beamd+(rbt-dbarbt)*↩
                Math.cos(phibt+Math.PI/2),(rbt+dbarbt)*Math.sin(↩
                phibt+Math.PI/2));
170         Point kpbt5 = Point.ofCartesian(beamd+(rbt+dbarbt)*↩
                Math.cos(phibt+Math.PI/2),(rbt-dbarbt)*Math.sin(↩
                phibt+Math.PI/2));
171         Point kpbt6 = Point.ofCartesian(beamd-rbt,0);
172
173         Point kpyoke_1 = Point.ofCartesian(ryok,0);
174
175
```

```
176
177         Point kpyoke_2 = Point.ofPolar(ryok, Math.PI/2-phibar-↩
                psicorn_1);
178
179         Point kpyoke_3 = Point.ofPolar(rcorn, Math.PI/2-phibar↩
                -psicorn_1);
180
181         Point kpyoke_4 = Point.ofPolar(rcorn, Math.PI/2-phibar↩
                -psibar);
182
183         Point kpyoke_5 = Point.ofPolar(rcorn, Math.PI/2-phibar↩
                +psibar);
184
185
186         Point kpyoke_6 = Point.ofPolar(rcorn, Math.PI/2-phibar↩
                +psicorn_2);
187
188
189         Point kpyoke_7 = Point.ofPolar(ryok, Math.PI/2-phibar+↩
                psicorn_2);
190
191
192         Point kpyoke_8 = Point.ofCartesian(xar05,yar05);
193         Point kpyoke_9 = Point.ofCartesian(0,ryok);
194         Point kpyoke_10 = Point.ofCartesian(0,yar05);
195         Point kpyoke_11 = Point.ofCartesian(0,yh1+rh1);
196         Point kpyoke_11a = Point.ofCartesian(rh1,yh1);
197         Point kpyoke_12 = Point.ofCartesian(0,yh1-rh1);
198         Point kpyoke_13 = Point.ofCartesian(0,0);
199
200         Point kph2_1 = Point.ofCartesian(xh2,yh2+rh2);
201         Point kph2_2 = Point.ofCartesian(xh2,yh2-rh2);
202
203         Point kph3_1 = Point.ofCartesian(xh3,yh3+rh3);
204         Point kph3_2 = Point.ofCartesian(xh3,yh3-rh3);
205
206         Point kpar05h_1 = Point.ofCartesian(xar05h_1,yar05h_1)↩
                ;
207         Point kpar05h_2 = Point.ofCartesian(xar05h_2,yar05h_2)↩
                ;
208
209         Point kpbar_1 = Point.ofPolar(ryok, Math.PI/4-psiscr);
210
211
212         Point kpbar_2 = Point.ofPolar(ryok, Math.PI/4+psiscr);
213
214
```

```
215 //            -- LINES
216
217           Arc lnyoke_1 = Arc.ofEndPointsCenter(kpbar_1, kpyoke_1↩
                  , kp0);
218
219           Arc lnyoke_2 = Arc.ofEndPointsCenter(kpbar_1, kpbar_2,↩
                   kp0);
220
221
222           Arc lnyoke_3 = Arc.ofEndPointsCenter(kpyoke_2, kpbar_2↩
                  , kp0);
223
224           Line  lnyoke_4 = Line.ofEndPoints(kpyoke_3,kpyoke_2);
225
226
227           Arc lnyoke_5 = Arc.ofEndPointsCenter(kpyoke_4, ↩
                  kpyoke_3, kp0);
228
229           Arc lnyoke_6 = Arc.ofEndPointsCenter(kpyoke_4, ↩
                  kpyoke_5, kp0);
230
231           Arc lnyoke_7 = Arc.ofEndPointsCenter(kpyoke_6, ↩
                  kpyoke_5, kp0);
232
233           Line  lnyoke_8 = Line.ofEndPoints(kpyoke_7,kpyoke_6);
234
235
236           Arc lnyoke_9 = Arc.ofEndPointsCenter(kpyoke_8, ↩
                  kpyoke_7, kp0);
237
238           Line  lnyoke_10 = Line.ofEndPoints(kpyoke_10,kpar05h_2↩
                  );
239
240
241           Line  lnyoke_11 = Line.ofEndPoints(kpyoke_11,kpyoke_10↩
                  );
242
243           Line  lnyoke_12 = Line.ofEndPoints(kpyoke_11,kpyoke_12↩
                  );
244
245           Line  lnyoke_13 = Line.ofEndPoints(kpyoke_12,kpyoke_13↩
                  );
246
247           Line  lnyoke_14 = Line.ofEndPoints(kpyoke_13,kpbt6);
248
249           Line  lnar05_1 = Line.ofEndPoints(kpyoke_8,kpyoke_9);
250
```

```
251         Line  lnar05_2 = Line.ofEndPoints(kpyoke_10,kpyoke_9);
252
253         Line  lnar05h_1 = Line.ofEndPoints(kpyoke_8,kpar05h_1)↩
                ;
254
255         Line  lnar05h_2 = Line.ofEndPoints(kpar05h_2,kpar05h_1↩
                );
256
257         Arc lnbt1 = Arc.ofEndPointsCenter(kpbt2, kpbt1, kp0_1)↩
                ;
258
259         Arc lnbt2 = Arc.ofEndPointsCenter(kpbt3, kpbt2, kp0_1)↩
                ;
260
261
262         Arc lnbt3 = Arc.ofEndPointsCenter(kpbt4, kpbt3, kp0_1)↩
                ;
263
264         Arc lnbt4 = Arc.ofEndPointsCenter(kpbt5, kpbt4, kp0_1)↩
                ;
265
266         Arc lnbt5 = Arc.ofEndPointsCenter(kpbt5, kpbt6, kp0_1)↩
                ;
267
268         Line  lnyoke_15 = Line.ofEndPoints(kpbt1,kpyoke_1);
269
270         Line  lnh2 = Line.ofEndPoints(kph2_1,kph2_2);
271
272         Line  lnh3 = Line.ofEndPoints(kph3_1,kph3_2);
273
274
275 //           -- AREAS
276
277 //           aryoke = HyperArea(lnyoke_1,lnyoke_2,lnyoke_3,↩
    lnyoke_4,lnyoke_5,lnyoke_6,lnyoke_7,lnyoke_8,lnyoke_9,↩
    lnar05h_1,lnar05h_2,lnyoke_10,lnyoke_11,lnyoke_12,lnyoke_13↩
    ,lnyoke_14,lnbt5,lnbt4,lnbt3,lnbt2,lnbt1,lnyoke_15,BHiron2)↩
    ;
278         Area aryoke = Area.ofHyperLines(new HyperLine[]{↩
                lnyoke_1,lnyoke_2,lnyoke_3,lnyoke_4,lnyoke_5,↩
                lnyoke_6,lnyoke_7,lnyoke_8,lnyoke_9,lnar05h_1,↩
                lnar05h_2,lnyoke_10,lnyoke_11,lnyoke_12,lnyoke_13,↩
                lnyoke_14,lnbt5,lnbt4,lnbt3,lnbt2,lnbt1,lnyoke_15})↩
                ;
279
280 //           ar05 = HyperArea(lnyoke_10,lnar05h_2,lnar05h_1,↩
    lnar05_1,lnar05_2,BHiron2);
```

```
281             Area ar05 = Area.ofHyperLines(new HyperLine[]{↩
                    lnyoke_10,lnar05h_2,lnar05h_1,lnar05_1,lnar05_2});
282
283
284             Element el2_1 = new Element(columns"columnsIY_El1columns"↩
                    , aryoke);
285             Element el2_2 = new Element(columns"columnsIY_El2columns"↩
                    , ar05);
286
287             Element[] quad1 = {el2_1};
288             Element[] quad2 = {el2_2};
289
290             return new Element[]{el2_1, el2_2};
291
292
293         }
294
295
296
297
298         public Element[] BoundaryConditions(){
299             double length = 10;
300             double eps  = 1e-4;
301
302             //POINTS
303             Point kpx1 = Point.ofCartesian(-length, 0-eps);
304             Point kpx2 = Point.ofCartesian(length, 0-eps);
305             Point kpx3 = Point.ofCartesian(length, 0+eps);
306             Point kpx4 = Point.ofCartesian(-length, 0+eps);
307
308             Point kpy1 = Point.ofCartesian(0-eps, -length);
309             Point kpy2 = Point.ofCartesian(0+eps, -length);
310             Point kpy3 = Point.ofCartesian(0+eps, length);
311             Point kpy4 = Point.ofCartesian(0-eps, length);
312
313             // LINES
314             Line lnx1 = Line.ofEndPoints(kpx2, kpx1);
315             Line lnx2 = Line.ofEndPoints(kpx2, kpx3);
316             Line lnx3 = Line.ofEndPoints(kpx3, kpx4);
317             Line lnx4 = Line.ofEndPoints(kpx1, kpx4);
318
319             Line lny1 = Line.ofEndPoints(kpy2, kpy1);
320             Line lny2 = Line.ofEndPoints(kpy2, kpy3);
321             Line lny3 = Line.ofEndPoints(kpy3, kpy4);
322             Line lny4 = Line.ofEndPoints(kpy1, kpy4);
323
324             // AREAS
```

```
325             Area xBC_Sel = Area.ofHyperLines(new HyperLine[]{lnx1,↩
                    lnx2, lnx3, lnx4});
326             Area yBC_Sel = Area.ofHyperLines(new HyperLine[]{lny1,↩
                    lny2, lny3, lny4});
327
328             // ELEMENTS
329             Element xBC = new Element(columns"columnsxBCcolumns", ↩
                   xBC_Sel);
330             Element yBC = new Element(columns"columnsyBCcolumns", ↩
                   yBC_Sel);
331
332             return new Element[]{xBC, yBC};
333         }
334
335     }
```

Chapter 9

Annex for chapter 5

Within these listings the included comments allow to understand and reuse the different modules of the LHC main quadrupole power converter module developed within this thesis. The first line includes the capture of the circuit and the input and output nodes of this circuit. From line 2 to 4 the parameters of this circuit are described. This parameters are set within this circuit to a default value of 0. When a test circuit will be generated, this parameters can be changed globally within the test circuit and will be automatically overwritten within the circuit of the sub sub sub module. This coupling structure between a global test and several circuits is used to run quickly several tests without big changes in every sub circuits. The numbers (i.e. (101 202)) within the brackets are the node numbers between which the specific circuit component is located.

Listing 9.1: power converter sub sub sub module

```
1  .subckt PC_Sub_Sub_Sub 1_pIn  1_pOut
2  + PARAMS:
3  + t_PS_off = {0}
4  + I_value  = {0}
5
6
7  v_monitor1 (1_pIn 100) 0
8
9  *The following subcircuit x_i_signal is the signal source of ↩
       RQ_PC_Signal.
10 *The signal will be turned off at the parameter t_ps_off.
11
12 x_i_signal (100 101) RQ_PC_Signal
13 + PARAMS:
14 + t_PS_off = {t_PS_off}
15 + I_value  = {I_value}
16
17 *This Switch is in parallel to the current source branch.
18 *The current will flow trough the switch, when x_i_signal will↩
       be switched off.
```

```
19 *This will happen at the same time, t_ps_off.
20
21 x_Switch3 (100 101 control) ↩
      RQ_PS_Sub_Sub_Sub_Switch_off_crowbar
22 + PARAMS:
23 + t_PS_off = {t_PS_off}
24
25 *$*******  The datasheet for the used diodes can be find here:
26 *$*******  S:\LHC\RQD_RQF\Circuit documentation\Datasheets\249↩
      nq135-150.PDF
27
28 *The following lines describe the branches with the diodes, ↩
      resistances and capacitances.
29
30 *The diode value starts with an "x_" as well, because the ↩
      every diode is stored in a global diode library.
31
32 x_D1 (101 102) 249NQ150
33
34 R_1 (101 202) 6.8
35 C_1 (202 102) 22e-9
36
37 R_2 (101 302) 6.8
38 C_2 (302 100) 15e-9
39
40 R_3 (100 401) 6.8
41 C_3 (401 102) 22e-9
42
43 x_D2 (100 102) 249NQ150
44
45 v_monitor2 (102 1_pOut) 0
46
47 .ends
48
49 *The subcircuit and the model of the used switch are described↩
       within this.
50 *This decreases the imbrication and the complexity.
51
52 .subckt RQ_PS_Sub_Sub_Sub_Switch_off_crowbar 1 2 control
53 + PARAMS:
54 + t_PS_off={0}
55 v_Switch_PS_test    (control 0) PULSE 0V 5V {t_PS_off} ↩
      0.000001s 10000s 10000s
56 S1    (1 2 control 0) xSmod
57 .model xSmod Vswitch  Voff=0.0V Von=5.0V  Roff=100e6 Ron=10e↩
      -06
58 .ends
```

Listing 9.2: power converter sub sub filter module

```
1
2  .subckt RQ_PC_FILTER_SUB_SUB    1_pIn_I 2_pIn_I 1_pOut_I_pos 2↩
       _pOut_I_neg
3
4
5  l_filter_1_pos_1        (1_pin_I 101) 670e-9
6
7  c_filter_1_1            (101 202) 470e-6
8  c_filter_1_2            (101 202) 470e-6
9  c_filter_1_3            (101 202) 470e-6
10 c_filter_1_4            (101 202) 470e-6
11
12
13 l_filter_1_pos_2        (101 102) 200e-9
14
15
16 c_filter_1_5            (102 203) 470e-6
17 c_filter_1_6            (102 203) 470e-6
18
19
20 l_filter_1_pos_3        (102 103) 200e-9
21
22
23 c_filter_1_7            (103 204) 470e-6
24 c_filter_1_8            (103 204) 470e-6
25 c_filter_1_9            (103 204) 470e-6
26
27 r_filter_1_1            (103 204) 100
28
29 c_filter_1_10           (103 204) 10e-3
30
31 r_filter_1_2            (103 202A) 50e-3
32 r_filter_1_3            (103 202A) 50e-3
33 r_filter_1_4            (103 202A) 50e-3
34 c_filter_1_11           (202A 204) 10e-3
35
36
37 *Capacitance to ground with the parallel resistor on the ↩
       positive branch of the filter
38 r_filter_earth_pos_1 (103 0) 1e6
39 c_filter_earth_pos_1 (103 0) 2.2e-6
40
41 l_filter_1_neg_1        (2_pIn_I 202) 670e-9
42 l_filter_1_neg_2        (202 203) 200e-9
```

```
43  l_filter_1_neg_3        (203 204) 200e-9
44
45  *Resistance of the fuse
46  r_filter_fuse_1 (204 205) 10e-9
47
48  *Capacitance to ground with the parallel resistor on the ↩
       negative branch of the filter
49  r_filter_earth_neg_1 (205 0) 1e6
50  c_filter_earth_neg_1 (205 0) 2.2e-6
51
52  v_monitor_1  (103 1_pOut_I_pos)    0
53
54  v_monitor_2  (205 2_pOut_I_neg)    0
55
56  .ends
```

Listing 9.3: power converter main output filter module

```
1   .subckt RQ_PC_FILTER_MAIN       1_pIn_I 2_pIn_I 1_pOut_I_pos 2↩
       _pOut_I_neg
2   *+ R_Cable = {960e-6}
3
4
5   v_monitor_1     (1_pIn_I 101) 0
6   v_monitor_2     (2_pIn_I 201) 0
7   *-------------------------------------
8
9
10  r_addition_pos_1_1_earth (101 0) 1e6
11  c_addition_pos_1_2_earth (101 0) 9e-6
12
13  r_addition_pos_1_3_earth (101 0) 1e6
14  c_addition_pos_1_4_earth (101 0) 9e-6
15
16
17  r_addition_neg_1_1_earth (201 0) 1e6
18  c_addition_neg_1_2_earth (201 0) 9e-6
19
20  r_addition_neg_1_3_earth (201 0) 1e6
21  c_addition_neg_1_4_earth (201 0) 9e-6
22
23
24  c_filter_1_1            (101 201) 18e-6
25
26
27  r_addition_pos_1_5_earth (101 0) 1e6
```

```
28  c_addition_pos_1_6_earth (101 0) 9e-6
29
30  r_addition_neg_1_5_earth (201 0) 1e6
31  c_addition_neg_1_6_earth (201 0) 9e-6
32
33
34  c_filter_1_2            (101 201) 18e-6
35
36
37  r_addition_pos_1_7_earth (101 0) 1e6
38  c_addition_pos_1_8_earth (101 0) 9e-6
39
40  r_addition_pos_1_9_earth  (101 0) 1e6
41  c_addition_pos_1_10_earth (101 0) 9e-6
42
43
44  r_addition_neg_1_7_earth (201 0) 1e6
45  c_addition_neg_1_8_earth (201 0) 9e-6
46
47  r_addition_neg_1_9_earth  (201 0) 1e6
48  c_addition_neg_1_10_earth (201 0) 9e-6
49
50
51
52  r_addition_pos_1_11_earth (101 0) 1e6
53  c_addition_pos_1_12_earth (101 0) 2.2e-6
54
55
56  x_D1 (101A 101) 440CNQ030_test
57  x_D2 (101A 101) 440CNQ030_test
58  x_D3 (101A 101) 440CNQ030_test
59  x_D4 (101A 101) 440CNQ030_test
60  x_D5 (101A 101) 440CNQ030_test
61  x_D6 (101A 101) 440CNQ030_test
62  x_D7 (101A 101) 440CNQ030_test
63  x_D8 (101A 101) 440CNQ030_test
64
65
66  r_monitoring_card_1 (201 101A) 100e-9
67
68
69  r_addition_pos_1_13_earth (101 0) 1e6
70  c_addition_pos_1_14_earth (101 0) 2.2e-6
71
72
73  x_D9 (101A 101) 440CNQ030_test
74  x_D10 (101A 101) 440CNQ030_test
```

```
x_D11 (101A 101) 440CNQ030_test
x_D12 (101A 101) 440CNQ030_test
x_D13 (101A 101) 440CNQ030_test
x_D14 (101A 101) 440CNQ030_test
x_D15 (101A 101) 440CNQ030_test
x_D16 (101A 101) 440CNQ030_test


r_monitoring_card_2 (201 101A) 100e-9


r_addition_pos_1_15_earth (101 0) 1e6
c_addition_pos_1_16_earth (101 0) 2.2e-6

x_D17 (101A 101) 440CNQ030_test
x_D18 (101A 101) 440CNQ030_test
x_D19 (101A 101) 440CNQ030_test
x_D20 (101A 101) 440CNQ030_test
x_D21 (101A 101) 440CNQ030_test
x_D22 (101A 101) 440CNQ030_test
x_D23 (101A 101) 440CNQ030_test
x_D24 (101A 101) 440CNQ030_test


r_monitoring_card_3 (201 101A) 100e-9

r_addition_pos_1_17_earth (101 0) 1e6
c_addition_pos_1_18_earth (101 0) 2.2e-6

x_D25 (101A 101) 440CNQ030_test
x_D26 (101A 101) 440CNQ030_test
x_D27 (101A 101) 440CNQ030_test
x_D28 (101A 101) 440CNQ030_test
x_D29 (101A 101) 440CNQ030_test
x_D30 (101A 101) 440CNQ030_test
x_D31 (101A 101) 440CNQ030_test
x_D32 (101A 101) 440CNQ030_test


r_monitoring_card_4 (201 101A) 100e-9


r_addition_pos_1_19_earth (101 0) 1e6
c_addition_pos_1_20_earth (101 0) 2.2e-6


x_D33 (101A 101) 440CNQ030_test
```

```
x_D34 (101A 101) 440CNQ030_test
x_D35 (101A 101) 440CNQ030_test
x_D36 (101A 101) 440CNQ030_test
x_D37 (101A 101) 440CNQ030_test
x_D38 (101A 101) 440CNQ030_test
x_D39 (101A 101) 440CNQ030_test
x_D40 (101A 101) 440CNQ030_test


r_monitoring_card_5 (201 101A) 100e-9


r_addition_pos_1_20_earth (101 0) 1e6
c_addition_pos_1_21_earth (101 0) 2.2e-6

x_D41 (101A 101) 440CNQ030_test
x_D42 (101A 101) 440CNQ030_test
x_D43 (101A 101) 440CNQ030_test
x_D44 (101A 101) 440CNQ030_test
x_D45 (101A 101) 440CNQ030_test
x_D46 (101A 101) 440CNQ030_test
x_D47 (101A 101) 440CNQ030_test
x_D48 (101A 101) 440CNQ030_test


r_monitoring_card_6 (201 101A) 100e-9


r_addition_pos_1_22_earth (101 0) 1e6
c_addition_pos_1_23_earth (101 0) 2.2e-6

x_D49 (101A 101) 440CNQ030_test
x_D50 (101A 101) 440CNQ030_test
x_D51 (101A 101) 440CNQ030_test
x_D52 (101A 101) 440CNQ030_test
x_D53 (101A 101) 440CNQ030_test
x_D54 (101A 101) 440CNQ030_test
x_D55 (101A 101) 440CNQ030_test
x_D56 (101A 101) 440CNQ030_test


r_monitoring_card_7 (201 101A) 100e-9

r_addition_pos_1_24_earth (101 0) 1e6
c_addition_pos_1_25_earth (101 0) 2.2e-6

x_D57 (101A 101) 440CNQ030_test
```

```
169  x_D58 (101A 101) 440CNQ030_test
170  x_D59 (101A 101) 440CNQ030_test
171  x_D60 (101A 101) 440CNQ030_test
172  x_D61 (101A 101) 440CNQ030_test
173  x_D62 (101A 101) 440CNQ030_test
174  x_D63 (101A 101) 440CNQ030_test
175  x_D64 (101A 101) 440CNQ030_test
176
177  r_monitoring_card_8 (201 101A) 100e-9
178
179  x_D65 (101A 101) 1_SKN6000_test
180  x_D66 (101A 101) 1_SKN6000_test
181  x_D67 (101A 101) 1_SKN6000_test
182
183  r_monitoring_card_9 (201 101A) 100e-9
184
185  c_filter_1_3            (101 201) 10e-6
186  c_filter_1_4            (101 201) 10e-6
187  c_filter_1_5            (101 201) 10e-6
188  c_filter_1_6            (101 201) 10e-6
189
190  c_filter_1_7            (101 201) 10e-6
191  c_filter_1_8            (101 201) 10e-6
192  c_filter_1_9            (101 201) 10e-6
193  c_filter_1_10           (101 201) 10e-6
194
195  c_filter_1_11           (101 201) 10e-6
196  c_filter_1_12           (101 201) 10e-6
197  c_filter_1_13           (101 201) 10e-6
198  c_filter_1_14           (101 201) 10e-6
199
200  c_filter_1_15           (101 201) 10e-6
201  c_filter_1_16           (101 201) 10e-6
202  c_filter_1_17           (101 201) 10e-6
203  c_filter_1_18           (101 201) 10e-6
204
205  c_filter_1_19           (101 201) 10e-6
206  c_filter_1_20           (101 201) 10e-6
207
208  *R_Cable_to_MAG001   (101 102) 480e-6
209
210  *R_Cable_to_Switch2  (201 202) 480e-6
211
212
213  v_monitor_3  (101 1_pOut_I_pos)    0
214
215  v_monitor_4  (201 2_pOut_I_neg)    0
```

```
216
217   .ends
```

Chapter 10

Annex for chapter 6

During the co-simulation progress of chapter 6, a new diode model for the protection diode was developed. The following listing contains the netlist file for this diode.

Listing 10.1: New model of the protection diode

```
1
2  .subckt RQ_Protection_Diode (p1_In      p1_Out)
3
4  .PARAM N   = {6}
5  .PARAM Rs  = 1e-6
6  .PARAM Is  = 1e-14
7  .PARAM U_VT = 30e-3
8  .PARAM fTL = {1/(0.00001*395*10^3)}
9  .PARAM N1   = {6}
10 .PARAM N2   = {1.2}
11 .PARAM I_0   = {50000}
12
13
14 v_input (p1_In 1) 0
15
16 v_output (2 p1_Out) 0
17
18 *- ABM component representing the diode behaviour
19
20 G_ABM_1 (1 2) VALUE {IF(V(1,2)>0&V(1_N)<6,LIMIT(Is*(EXP(V(1,2)↩
       /(V(1_N)*U_VT))-1),0,I_0),0)}
21
22
23
24 *- Diode current times the voltage across the diode -> to get ↩
       the power. P = U * I
25 E_ABM_diode_power (1_power  0) VALUE = {IF(V(1,2)>0,Is*(EXP(V↩
       (1,2)/(V(1_N)*U_VT))-1)*V(1,2),0)}
26
```

```
27  *- Integration of the power --> energy of the diode
28  E_ABM_diode_energy (1_energy  0) VALUE = {SDT(V(1_power))}
29
30  *- Calculation of the changed parameter N to N_scaled
31  E_ABM_N_Parameter_scale (1_N  0) VALUE = {LIMIT(N1-(N1-N2)*V(1↩
        _energy)*fTL, N2, N1)}
32
33  .ends
```